University of Tennessee, Knoxville

TRACE: Tennessee Research and Creative Exchange

Doctoral Dissertations

Graduate School

8-2007

Development of an integrated opto-electric biosensor to dynamically examine cytometric proliferation and cytotoxicity

Chang Kyoung Choi
University of Tennessee - Knoxville

Follow this and additional works at: https://trace.tennessee.edu/utk_graddiss

Part of the Mechanical Engineering Commons

Recommended Citation

Choi, Chang Kyoung, "Development of an integrated opto-electric biosensor to dynamically examine cytometric proliferation and cytotoxicity. " PhD diss., University of Tennessee, 2007.
https://trace.tennessee.edu/utk_graddiss/139

This Dissertation is brought to you for free and open access by the Graduate School at TRACE: Tennessee Research and Creative Exchange. It has been accepted for inclusion in Doctoral Dissertations by an authorized administrator of TRACE: Tennessee Research and Creative Exchange. For more information, please contact trace@utk.edu.

To the Graduate Council:

I am submitting herewith a dissertation written by Chang Kyoung Choi entitled "Development of an integrated opto-electric biosensor to dynamically examine cytometric proliferation and cytotoxicity." I have examined the final electronic copy of this dissertation for form and content and recommend that it be accepted in partial fulfillment of the requirements for the degree of Doctor of Philosophy, with a major in Mechanical Engineering.

Kenneth D. Kihm, Major Professor

We have read this dissertation and recommend its acceptance:

Anthony English, Majid Keyhani, Jayne Wu

Accepted for the Council:

Carolyn R. Hodges

Vice Provost and Dean of the Graduate School

(Original signatures are on file with official student records.)

To the Graduate Council:

I am submitting herewith a dissertation written by Chang Kyoung Choi entitled "Development of an integrated opto-electric biosensor to dynamically examine cytometric proliferation and cytotoxicity". I have examined the final electronic copy of this dissertation for form and content and recommended that it be accepted in partial fulfillment of the requirements for the degree of Doctor of Philosophy, with a major in Mechanical Engineering.

Kenneth D. Kihm
Major Professor

Anthony English
Co-advisor

We have read this dissertation
and recommend its acceptance:

Majid Keyhani

Jayne Wu

Accepted for the council:

Carolyn Hodges
Vice Provost and Dean of the
Graduate School

(Original signatures are on file with official student record)

Development of an integrated opto-electric biosensor to dynamically examine cytometric proliferation and cytotoxicity

A Dissertation Presented for the Doctor of Philosophy Degree

The University of Tennessee, Knoxville

Chang Kyoung Choi

August, 2007

DEDICATION

To my parents (In Ok Choi & Soon Nam Ha) and my family (wife: Kyoung Min Kim, daughter: Won Young Choi, & son: Jiseung Choi)

ACKNOWLEDGEMENTS

I would like to express my deepest respect to my primary advisor, Dr. Kenneth D. Kihm. He is not only a great scientist filled with great ideas and enthusiasm but also a great man filled with a wonderful and positive soul. He has inspired my research interest in the world of microfluidics and opto-electric cellular imaging. I would also like to express my heartfelt gratitude to my intellectual co-advisor, Dr. Anthony E. English, for his valuable guidance and constant support throughout this study. I would like to express my sincere thanks to my graduate committee members, Dr. Majid Keyhani and Dr. Jayne Wu, for their important observations and advice on the research work.

Most of my work would not have been possible without the help of Dr. Philip D. Rack and his students. I would like to express my further appreciation to Dr. Seung Joon Baek, Dr. Seung-Ho Lee, and other members of the Pathobiology Laboratory for their support. It has been my pleasure to study together with my colleagues, Joseph Tipton, Iltai Kim, and Seunghwan Kim as well as Chuck Margraves, who is one of my best friends.

On a personal note, I would like to express my appreciation to my wonderful parents and lovely parents in-law respectively, In-Ok Choi, Soonnam Ha, Gwangbaek Kim, and Oksoon Kim, for their warmth and support. I would also like to express my deepest appreciation to my marvelous wife, Kyoung Min Kim, for her encouragement and excellent support, as well as her being the most important role model of mother to our wonderful kids, Won Young Choi and Jiseung Choi. Final thanks go to my younger brothers and their family, to my grandmother, and my youngest maternal uncle, Moonsik Ha and his family for their wonderful support.

ABSTRACT

My doctoral research has focused on the development of microscale optical techniques for examining micro/bio fluidics. Preliminary work measured the velocity field in a microchannel, by optical slicing, using Confocal Laser Scanning Microscopy (CLSM). Next, Optical Serial Sectioning Microscopy (OSSM) was applied to examine thermometry by detecting the free Brownian motion of nano-particles suspended in mediums at different temperatures. An extension of this work used objective-based Total Internal Reflection Fluorescence Microscopy (TIRFM) to examine the hindered Brownian motion of nano-particles that were very close to a solid surface (within 1 μm).

An optically transparent and electrically conductive Indium Tin Oxide (ITO) biosensor and an integrated dynamic live cell imaging system were developed to dynamically examine changes in cell coverage area, cell morphology, cell-substrate adhesion, and cell-cell interaction. To our knowledge this is the first sensor capable of conducting simultaneous optical and electrical measurements. This system consists of an incubator, which keeps cells viable by providing the necessary environmental conditions (37 °C temperature and 5 % CO_2), and multiple microscopy techniques, including multi-spectrum Interference Reflection Microscopy (MS-IRM), TIRFM, Epi-fluorescence Microscopy, Phase Contrast Microscopy (PCM), and Differential Interference Contrast Microscopy (DICM). Along with investigations of cytometric proliferation including cellular barrier functions, *in vitro* cytotoxicity experiments were also conducted to examine the effect of a drug (cytochalasin D, a toxic agent) on cellular motility and cellular morphology. These cytotoxicity results give us a fundamental understanding of the cellular processes induced by the drug, which will be invaluable in the search for methods of preventing metastases. In this research, MS-IRM is used to examine the focal contacts and the gap morphology between cells and substrates, DICM is used to examine the coverage area of cells, and impedance measurements are used to correlate these two parameters.

Advances in the understanding of vascular bio-transport in endothelial cells will have an impact on many aspects of cell biology, tissue engineering, and pharmacology. Particularly important will be the ability to test the popular hypothesis that the cell barrier function is regulated by specific cytoskeleton elements controlling intercellular and extracellular coupling.

TABLE OF CONTENTS

Development of an integrated opto-electric biosensor to dynamically examine cytometric proliferation and cytotoxicity

---

LIST OF TABLES

LIST OF FIGURES

CHAPTER 1

OPTICAL SENSING

1.1 Confocal Laser Scanning Microscopy (CLSM)

1.1.1 Introduction

A confocal microscopy, patented by Dr. Marvin Minsky [1] at Harvard University in 1957, dramatically improves optical resolutions in microscopic imaging to an unprecedented level of 180-nm lateral resolution and 500-nm axial resolution (refer to the next section for more details). The most important feature of the confocal microscopy is its ability to deliver extremely thin, in-focus images by true means of depth-wise optical slicing, and allowing the gathering of 3-D reconstructed information by the line-of-sight imaging without the need of physical sectioning of specimens.

The basic ‘confocal’ concept is described by a point scanning of the laser excitation and a spatially filtered fluorescence signal emitting from the focal point onto the confocal point (Figure.1.1-a). The pinhole aperture, located at the confocal point, allows emitted fluorescent light, exclusively from the focal point, to pass through the detector (solid lines), and filters out fluorescent light emitted from outside the focal point (dashed lines). This “spatial filtering” is the key principle to enhance the optical resolutions by devising the depth-wise optical sectioning. The illuminating laser scans rapidly from point to point, in a synchronized way with the aperture, to produce a full-field image on the detector. The practical confocal microscopy [2] has been widely used in biology, material, and medical research to allow microstructures to be visible where they would be otherwise invisible because of the depth-wise obscurity.

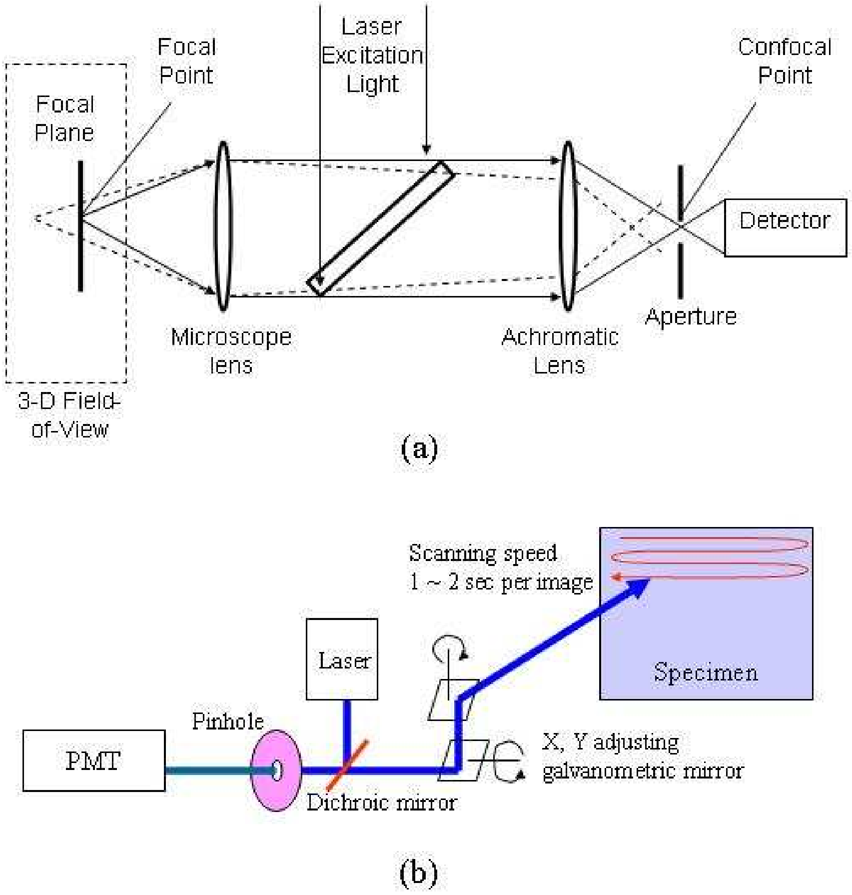

Figure 1.1: Principle of Confocal Microscopy using a pinhole as a spatial filter (a), and a schematic illustration of galvanometric scanning to conform to a full-field image (b).

Optical characterization of confocal microscopy has been fairly well studied by a number of optics researchers. The depth discrimination capability of this microscopy has been analytically characterized for a range of fluorescence wavelengths and the simulation results have been compared with the corresponding experimental results [3]. A quantitative theoretical analysis for standard confocal microscopy, in conjunction with 3-D fluorescence correlation spectroscopy, has been developed using a point-spread function in conjunction with a collection efficiency function [4]. Aberration compensations for confocal microscopy were discussed for spherical aberration occurring when one is focusing deep within the specimen [5], and for additional aberrations induced by mismatches in refractive index values across or inside the specimen[6]. An extensive study [7] shows that the signal-to-background ratio (S/B), with background defined as the detected light that originates outside a resolution volume, obtained with a confocal microscope can be more than 100 times greater than the S/B available with a conventional microscope, and the optimized confocal signal-to-noise ratio (S/N) can be a factor of 10 greater than the S/N of the conventional microscope.

The galvanometric steering of the focal point of the traditional confocal microscopy (Figure. 1.2-b) limits its scanning speed to approximately one (1) image-per-second (IPS), which is too slow for real-time observation of moving objects at any practical speeds. The innovative use of a rotating micro-lens array [8, 9], replacing the single pinhole, makes it possible for confocal microscopy to scan full-field images at substantially higher IPS rates. Further study has been done to use the high-speed confocal microscopy using a rotating scanner for advanced bio-medical applications of real-time 3-D imaging of single molecular fluorescence [10]. Both theoretical and experimental comparisons have been studied for the depth-wise resolution of the high-speed confocal microscopy with multi-focal and multi-photon microscopy [11].

The essential innovation of the Confocal Laser Scanning Microscopy (CLSM) is the use of dual high-speed spinning disks (Figure. 1.2): the upper disk is a rotating scanner that consists of 20,000 micro-lenses, and the lower one is called a Nipkow disk that consists of matching 20,000 pinholes of 50-μm in diameter. Both of the incident excitation light and emitting fluorescence light paths are defined by a similar optical path. The pumping light is focused by the micro-lens of the scanning disk through the pinholes on the Nipkow disk. A dichroic mirror, located between the two disks, reflects the returning confocal fluorescence image to the CCD for real-time, true color recording. As the disk rotation of 30-rps and a scanning speed of 360 IPS are possible, and the multiple pinholes sweep the view, a full field imaging at up to 120-IPS is possible by averaging three sweeps per single field for statistical enhancement.

The idea is that the CLSM can accommodate the use of microscopic-Particle Image Velocimetry [12-14] to achieve optically-sliced microfluidic velocity field mappings. To the authors' knowledge, the use of CLSM for micro-PIV has not been published in any open literature to date. A comparative characterization of the CLSM micro-PIV and a regular micro-PIV is presented by measuring the same flow configurations under otherwise identical optical conditions of image magnification, field illumination, and fluorescence filtering. Detailed flow measurements have been conducted for Poiseuille flows developed in micro-capillary pores of 100-μm and 500-μm internal diameters (ID, nominal) are presented between the CLSM micro-PIV and the regular epi-fluorescent micro-PIV comparison.

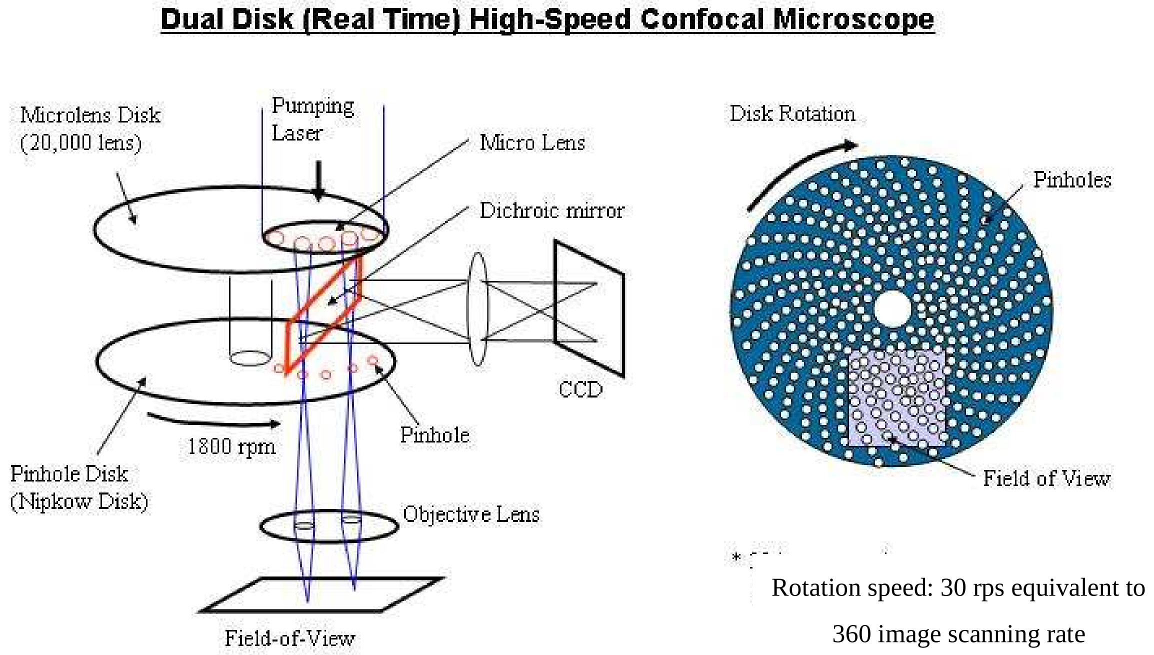

Rotation speed: 30 rps equivalent to
360 image scanning rate

Figure 1.2: A principle of the dual-Nipkow disk design for a high-speed Confocal Laser Scanning Microscopy (CLSM).

1.1.2 Lateral/Axial Image Resolution and Optical Image Slicing

1.1.2.1 Conventional microscope

When the Fraunhofer condition[1] is satisfied, microscopic particle imaging can be depicted by the Fraunhofer diffraction rings, called the Airy function [15]. Two neighboring objects are said to be marginally resolved when the center of one Airy disk falls on the first minimum of the other Airy pattern, i.e., the so-called Rayleigh criterion for monochromatic imaging. The Rayleigh criterion is generally defined as the lateral resolution for conventional microscopic imaging and used to estimate the minimum resolvable distance between two point sources of lights generated from a specimen (Table 1). If emitted wavelengths (λ_{em}) of point sources are all the same, their Airy disks have the same diameter, as long as for the same objective with a specified *NA*[2], and the Rayleigh criterion is equal to the radius of the Airy disk, i.e., $0.61\lambda_{em}/NA$ where NA is the numerical aperture of the microscopic objective lens.

Unlike the lateral Fraunhofer diffraction, the axial diffraction pattern of a point source does not constitute a disk-shape but an hourglass shape or flare of the Point Spread Function (*PSF*). A similar reasoning can be used to draw the axial Rayleigh criterion [2], which is defined by taking the distance from the maximum intensity

---

[1] This is also called a "far-field" diffraction condition, which is defined as $R > a^2/\lambda$ where R is the smaller of the two distances from the particle to the objective lens and the objective lens to the imaging detector, a is the particle radius, and λ is the wavelength in the medium. For typical conditions for micro-PIV, R ~ 1 mm, a ~ 200 nm, and λ ~ 500 nm, the inequality is well satisfied by more than 12,000 in ratio.

[2] Numerical Aperture (*NA*) is defined as $NA \equiv n_i \sin\theta_{\max}$ where n_i is the refractive index of the immersing medium (air, water, oil, etc.) adjacent to the objective lens, and $\theta_{\max}$ is the half-angle of the maximum cone of the light apertured by the lens.

location at the focal plane to the first location of the minimum intensity along the optical axis, or equivalently $2n\lambda_{em} / NA^2$ (Table 1). Note that the axial resolution increases with increasing refractive index of the medium, *n*, whereas the lateral resolution is independent of *n*. In usual sense, the Depth-of-Field (*DOF*) is referred to the defocusing range from the focal plane image of a single particle or object before its "unacceptable" blur is observed, and *DOF* is conventionally defined as one-half of the axial resolution, i.e., $DOF \equiv n\lambda_{em} / NA^2$. However, *DOF* does not constitute a true meaning of "depth-wise optical slicing" of images when multiple particles/objects are imaged in the line-of-sight direction.

1.1.2.2 Confocal microscope

The pinhole diameter is an important parameter for a confocal microscope and plays a decisive role in determining its image resolutions. When the modified pinhole diameter[3], *PD*, is greater than one (1) Airy Unit (*AU*[4]), i.e., $PD > 1.0\ AU$, a geometrical-optical analysis is used, while for $PD < 0.25\ AU$, a wave-optical analysis is applied [16]. Summarized results are presented also in Table 1 for the lateral/axial resolution formulas for both geometrical-optical and wave-optical confocal microscope systems. The lateral resolution uses a criterion based on Full Width at Half Maximum (*FWHM*) two neighboring *PSF* images at the confocal plane, somewhat analogous to the Rayleigh criterion of a conventional microscope, but additionally accounting for the pinhole effect of spatial filtering on the image construction that is restricted from the full Airy pattern of Fraunhofer diffraction. Likewise, the axial resolution of confocal microscope is based on

---

[3] Modified pinhole diameter, $PD \equiv$ Pinhole diameter (μm)/Magnification

[4] Airy unit, $AU \equiv 1.22\ \lambda_{ex}/NA$ with λ_{ex} being the fluorescent excitation wavelength

Table 1.1 Lateral/Axial Resolution and Optical Slice Thickness for both Conventional and Confocal Microscope Systems.

		Conventional Microscope	**Geometrical-Optical Confocal Microscope**	**Wave-Optical Confocal Microscope**
Lateral Resolution		$\frac{0.61\lambda_{em}}{NA}$	$\frac{0.51\lambda_{ex}}{NA}$	$\frac{0.37\overline{\lambda}}{NA}$
Axial Resolution	**NA$\geq$0.5**	$2\frac{n \cdot \lambda_{em}}{NA^2}$	$\frac{0.88\lambda_{ex}}{n-\sqrt{n^2-NA^2}}$	$\frac{0.64\overline{\lambda}}{n-\sqrt{n^2-NA^2}}$
	NA<0.5		$\frac{1.67n \cdot \lambda_{ex}}{NA^2}$	$\frac{1.28n \cdot \overline{\lambda}}{NA^2}$
Optical Slice Thickness		No Definition	$\sqrt{\left(\frac{0.88\lambda_{em}}{n-\sqrt{n^2-NA^2}}\right)^2+\left(\frac{\sqrt{2}n \cdot PD}{NA}\right)^2}$	$\frac{0.64\overline{\lambda}}{n-\sqrt{n^2-NA^2}}$

FWHM of *PSF* constructed along the optical axis.

Note that the axial resolution uses two different formulas depending on the ranges of *NA* of the objective. Also, while for the geometrical-optical confocal microscope both lateral and axial resolutions are functions of the excitation wavelength, λ_{ex}, for the wave-optical confocal microscope they are functions of the mean wavelength $\overline{\lambda}$[5], of λ_{em} and λ_{ex}. In contrast, the image resolutions for conventional microscope depend only on the emission wavelength λ_{em}. Note that the nominal magnifications are specified for the conventional microscopic imaging, but they had to be corrected for the case of the confocal microscopy since the optical paths are routed through the confocal unit before the detector resulting in slightly reduced actual magnifications. While the lateral resolution of the confocal microscope is slightly better than that of the conventional microscope, the confocal axial resolution shows more than 20 % reduction from the conventional microscope.

More exclusive and unique feature of confocal microscopy may be represented by its optical slicing capability. Since the focused region is defined approximately as a "lobe" elongated along the optical axis, rather as an ideal point, primarily because of spherical and/or chromatic aberrations, it constitutes a distributed probe imaging volume laterally as well as axially. For a conventional microscope, when the imaging plane moves away from the focal plane, the image focusing is degraded but the integrated amount of the emitted light energy remains more or less unchanged as long as the

---

[5] The mean wave length is defined as $\overline{\lambda} \equiv \sqrt{2}\,\dfrac{\lambda_{ex} \cdot \lambda_{em}}{\sqrt{\lambda_{ex}^2 + \lambda_{em}^2}}$.

defocusing distance is smaller than the axial dimension of the probe volume. As a result, off-focused images are blurred and larger in size with reduced intensity (reduced number of photons bombarded per unit area), but their total number of photons remains the same because of no spatial filtering restrictions. Since the entire flow field is illuminated in the line-of-sight direction in micro-PIV configuration, the integrated and blurred images contribute to degrading the measured velocity vector fields. The effective depth, so-called the depth-of-correlation, over which particles will contribute to the measured velocity has been well documented elsewhere for the case of conventional micro-PIV measurements [17, 18]

In contrast, for the case of spatial filtering by a pinhole of confocal microscopy, the maximum number of photons is recorded only when the focal plane is imaged with the pinhole allowing minimum level of filtering of the incoming light. The integrated light energy dramatically drops as the defocusing level is progressed with image planes *b*, *c* and *d*, since the amount of the spatial filtering progressively increases with the degree of defocusing. This allows truly “optically sliced” image recording for confocal microscopy. No such definition for optical slicing is available for conventional microscopy. Therefore, the confocal microscope, can exclusively observe fluorescence particles near the focus, with a peak of the integrated light energy, and the detected light energy falls off sharply as one moves out of focus.

Analytical expressions for the optical slice thickness that were developed theoretically with experimental corrections from multiple contributors [2-4, 7, 16, 19, 20] are tabulated for both geometrical-optical and wave-optical microscopic ranges in Table 1. Note that the slice thickness for the geometrical-optical range depends on the pinhole diameter whereas that for the wave-optical range a single formula is defined uniquely for all pinhole diameters as long as they satisfy the criterion of $PD < 0.25\ AU$. Table 2 shows the optical parameters for the present experimental consideration for typical cases and the calculated optical resolutions and optical slice thicknesses using the formula presented in Table 1. The confocal microscope system at *Microscale Fluidics and Heat Transport Laboratory* (http://minsfet.utk.edu) falls under the geometric-optical confocal microscope as $PD = 1.329$ for the 40X nominal (37.6X confocal) and = 5.319 for the 10X nominal (9.4X for confocal), both *PD* values are satisfying the geometric optic conditions of being larger than one corresponding *AU*. The objective lenses are semi-apochromat and air-immersion types. The optical slice thickness is estimated to be better than 3-μm for the 40X nominal objective and less than 27-μm for the 10X nominal objective. The former objective is used to record particle image fields at different imaging planes inside the 100-μm ID pore, and the latter objective, for the 500-μm ID pore. No effective means of optical slicing is available for conventional microscopy. With the conventional microscope, clear images can only be obtained when the line-of-sight dimension of the test field is less than the wave-optical *DOF* of the objective, defined as one-half of the axial resolution. When the line-of-sight dimension exceeds the specified *DOF*, integrated object information is recorded that is inevitably blurred by the out-of-focus forward as well as background images.

Table 1.2 Representative optical parameters for the present study and the optical resolutions and the slice thickness of the confocal microscope system.

λ_{ex}, excitation wavelength (μm)	0.488	
λ_{em}, emission wavelength (μm)	0.515	
$\bar{\lambda}$, mean wavelength (μm)	0.500879	
Refraction Index	1.0	
NA	0.75	0.3
Overall Magnification	40 (37.6)	10 (9.4)
Airy Unit (*AU*)	0.793	1.984
Pinhole Diameter (μm)	50	50
PD (μm)	1.329	5.319

	Conventional microscope		**Geometrical-optical confocal microscope**		**Wave-optical confocal microscope**	
	40X	10X	40X	10X	40X	10X
Lateral resolution	0.418	1.047	0.331	0.829	0.247	0.617
Axial resolution	1.831	11.444	1.268	9.323	0.946	6.959
Optical Slice Thickness	Not Defined		2.820	26.701	0.946	6.959

1.1.3 Experimental System

Figure 1.3 describes an experimental setup of micro-PIV system using high-speed CLSM. The experimental setup consists of a dual-Nipkow disk confocal module (CSU-10, Yokogawa), an upright microscope (BX-61, Olympus), a 50-mW CW Ar-ion laser (Laser Physics), a frame grabber board (QED Imaging), a CCD camera (UP-1830, UNIQ, 1024 x 1024 pixels at 30 FPS), a micro syringe pump (55-2111, Harvard apparatus), a micro test section, and PIV analysis software (Davis, LaVision). The lower inlet port of the confocal head unit is attached to the ocular port of the microscope and the upper outlet port is connected to the CCD camera. A series of digital images are transferred from the CCD camera to a computer by passing through a digital cable and a frame grabber board. A fiber optic cable (OZ optics) connects the confocal module with Ar-ion laser, whose illuminating light passes through the fiber optic, a confocal module and an objective lens, then reaches on a test section. A test section is connected with a micro syringe by using Teflon tube and a micro syringe pump constantly pushes the micro syringe so as to generate a designated flow rate.

1.1.4. Comparison of Particle Images between Conventional Microscopy and Confocal Microscopy

The PIV raw images are shown for three selected planes of $y/R = 0$ at the center-plane, $y/R = 0.4$, and $y/R = 0.8$ near the top end of the microtube inner surface, in Figure. 1.4. and 1.5. The 516-μm ID microtube is imaged at 9.4X confocal or 10X conventional microscope, and the 99-μm ID microtube, at 37.6X or 40X, respectively. The confocal microscopic images demonstrate optically sliced images with clear image definition of individual particles located within the slice thickness. On the contrary, the conventional

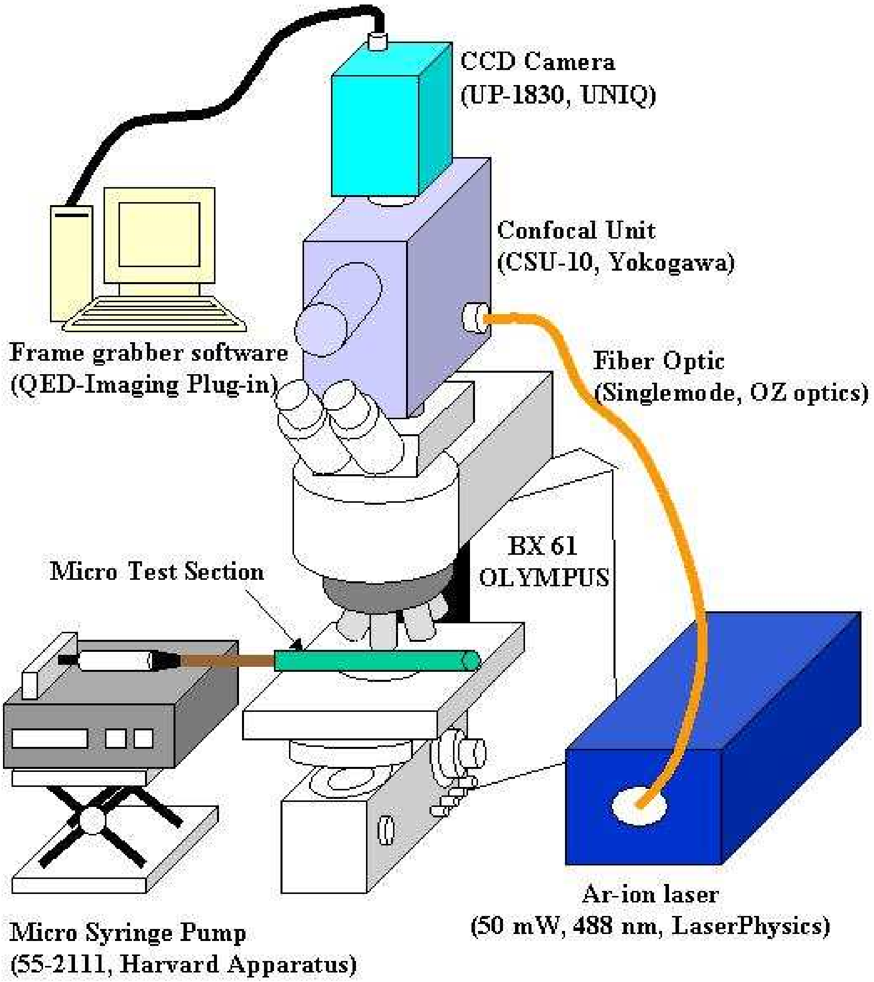

Figure 1.3: Experimental setup of micro-PIV system using high-speed CLSM.

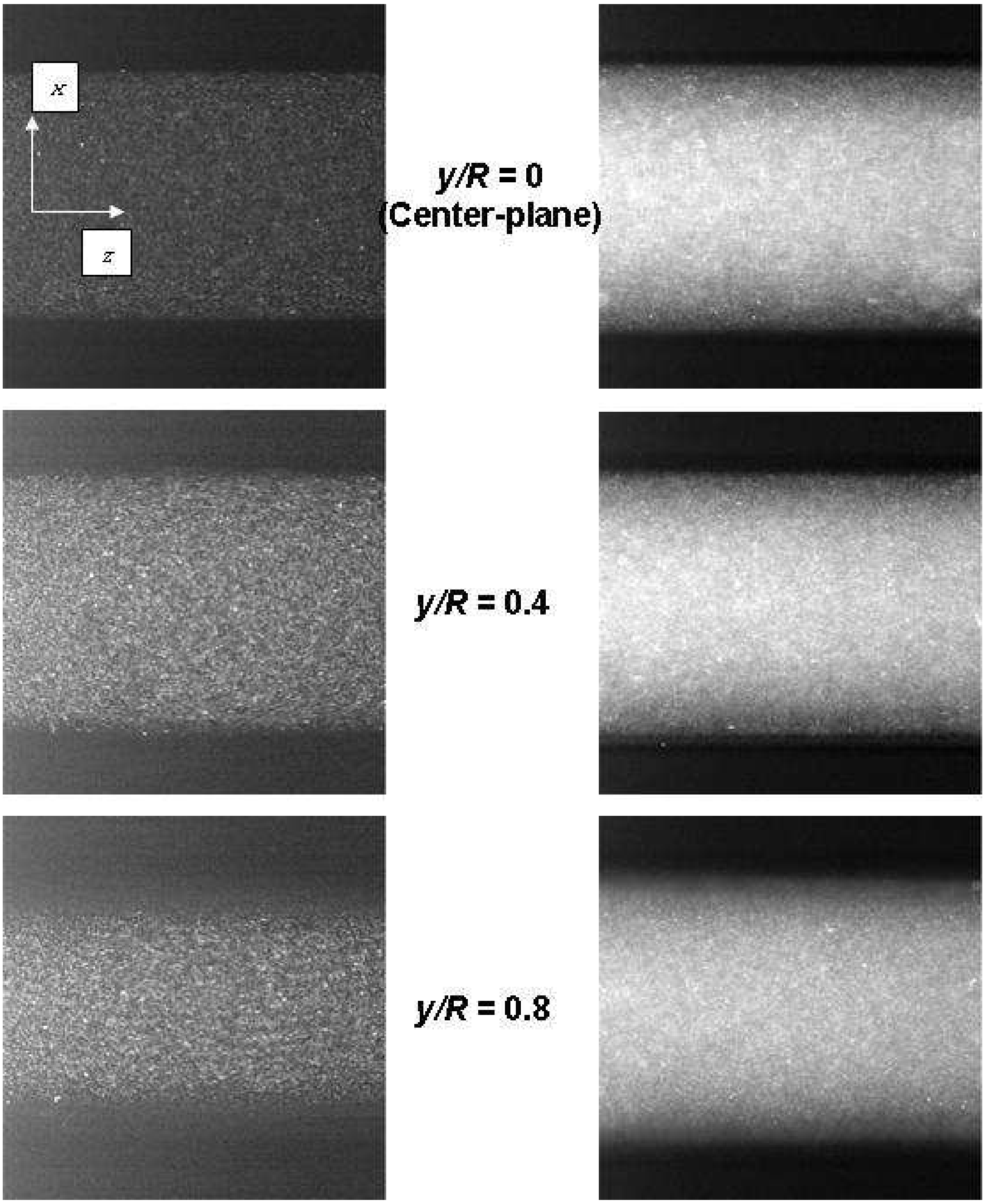

Figure 1.4: Particle images taken at three different *y*-planes of a 516-µm channel by the CLSM (left column) and by the wide-field epi-fluorescence (right column) microscopy.

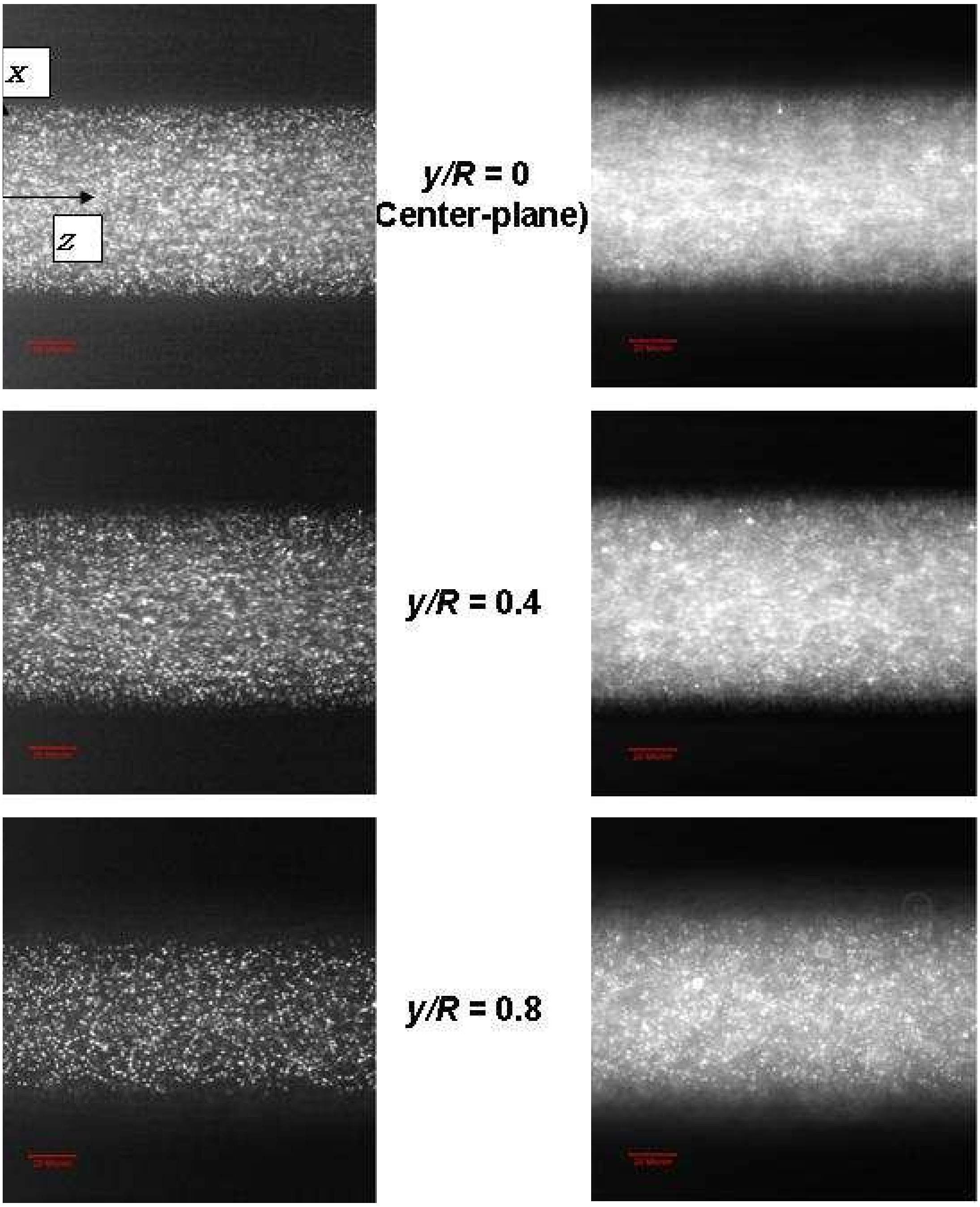

Figure 1.5: Particle images taken at three different *y*-planes of a 99-µm channel by the CLSM (left column) and by the wide-field epi-fluorescence (right column) Microscopy.

microscopic images are largely obscured by the blurred off-focused images, as the line-of-sight dimension of the microtube far exceeds the estimated *DOF* of 0.92--μm for 40X, or of 5.72--μm for 10X. The background noise from the off-focused particle images can be reduced to an acceptable extent by limiting the PIV measurement depth to a base-cut level where the field-wide-averaged image intensity reaches a one-tenth of the maximum in-focus image intensity [18]. In addition, the stray light rays that are internally reflected from the microtube inner surface and externally refracted/reflected rays through the curved microtube wall enter the detector without being spatially filtered and they further deteriorate the particle images. Though there are a number of techniques known to improve PIV images, including the use of an oil-immersion objective with high *NA* or the use of a pulsed laser for illumination, no further attempt has been accommodated at present since the primary interest is to compare the image and velocity field data quality between the CLSM micro-PIV and the conventional micro-PIV under specified and identical imaging conditions.

The apparent image diameter of 200-nm particles, when back-projected to the physical domain, is estimated to be 2.10-μm for 10X imaging of the 516-μm microtube, and to be 0.86-μm for 40X imaging of the 99-μm microtube, assuming that negligible particle image streaks occur from the particle displacement during a finite shutter opening time. The relative particle image size normalized by the tube diameter, i.e., 0.87% for the 99-μm microtube is more than two times bigger than 0.42% for the 516-μm microtube. For the case of the smaller microtube, the relatively larger image size makes it essential to accommodate the reduced particle number density in that the seeding concentration is increased by only five times.

Another point to note is that the normalized flow velocity based on the microtube diameter for the smaller microtube (0.545 s^{-1} ≡ 54-µm·s^{-1}/99-µm) is more than three times higher than that for the larger microtube (0.154 s^{-1} ≡ 79.7-µm·s^{-1}/516-µm), and this explains the more image streaks shown for the 99-µm microtube than for the 516-µm microtube. The 54-µm/s is bound by the lower limit of the volume flow rate of 0.75-µl/hr given by the micro syringe pump used. The particle image streaks during the 33.3-ms exposure time at 30-FPS are 1.8-µm for the 99-µm microtube (more than two times larger than the particle image size of 0.86-µm or 33% of the 5.5-µm interrogation volume size) and 2.7-µm for the 516-µm microtube (approximately the same as the particle image size of 2.10-µm or 12.3% for the 22-µm interrogation volume size). Therefore, the resulting PIV flow vector field data for the smaller microtube will likely be subjected to more bias because of its lower particle image density and the higher normalized velocity.

In order to compensate for such bias, a more rigorous analysis for the PIV software improvement has been extensively studied using a highly accurate high-resolution PIV technique, particularly to improve the sub-pixel measurement accuracy [14]. At present, in spite that these aspects could be improved to an extent by carefully altering the related parameters to the PIV analysis, no further attempt has been contemplated since the comparative observation for the level of such bias is important to characterize the differences between the conventional- and the CLSM micro-PIV systems. Another way to alleviate the image streaking bias will be to use a sufficiently short-pulsed illumination to freeze imaging frame, which is commonly exercised by many researchers in using conventional micro-PIV [13].

1.1.5 Poiseuille velocity profiles developed in microtubes

Figures 1.6 and 1.7 show measured velocity profiles at different *y*-planes of the 99-µm and 516-µm microtubes, respectively, and the solid symbols represent the CLSM micro-PIV data, the regular symbols for the conventional micro-PIV data, and the parabolic curves represent the ideal Poiseuille flow profiles that are depth-corrected accounting for the aforementioned refractive index mismatching.

All presented results represent the flow field of raw vectors with no attempt for artificial validation scheme implemented so that the imaging capabilities are exclusively compared between the CLSM micro-PIV system and the conventional micro-PIV system. The error bars represent 95% standard deviations of the averaged data of thirty (30) axial locations at constant x per each image and for all twenty-nine (29) PIV image pairs processed, i.e., average of 870 velocity profiles all together. Note that the Poiseuille flow profile is calculated directly from the specified volume flow rate conditions without attempting any normalization for the velocity profiles, i.e., 54-µm/s center maximum velocity from 0.75-µl/hr for the 99-µm microtube or 79.7-µm/s center maximum velocity from 30-µl/hr for the 516-µm microtube. The laminar flow entrance or developing length is given as L/D = 0.65 (Lew and Fung, 1970) and the corresponding length is calculated to L = 64.4-µm for the smaller microtube and L = 335-µm, and thus, the tested microtube flows have negligibly small entrance region to establish fully developed Poiseuille flow within less than one-diameter distance from the entrance.

For the 99-µm microtube, the CLSM data at the centerplane (Figure 1.6-a) shows a fairly good agreement with the calculated Poiseuille profile as anticipated by the truly resolved depth-wise PIV imaging by the well-defined optical slice thickness of 2.82-µm

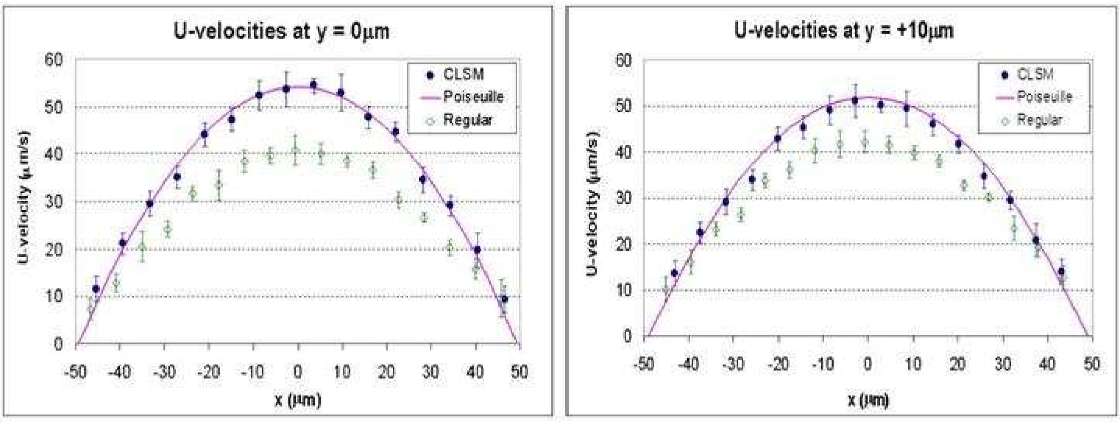

(a) y/R = 0 **(b) y/R = 0.2**

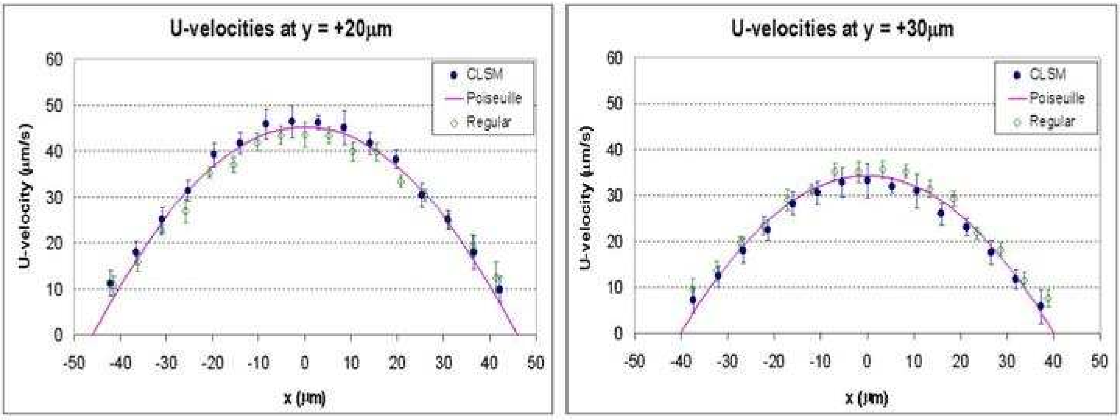

(c) y/R = 0.4 **(d) y/R = 0.6**

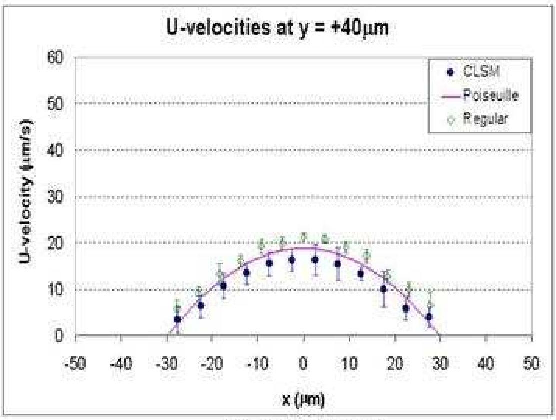

(e) y/R = 0.8

Figure 1.6: Comparison of the velocity profiles measured by the CLSM micro-PIV and by the conventional micro-PIV at different *y*-planes of the 99-μm ID microtube.

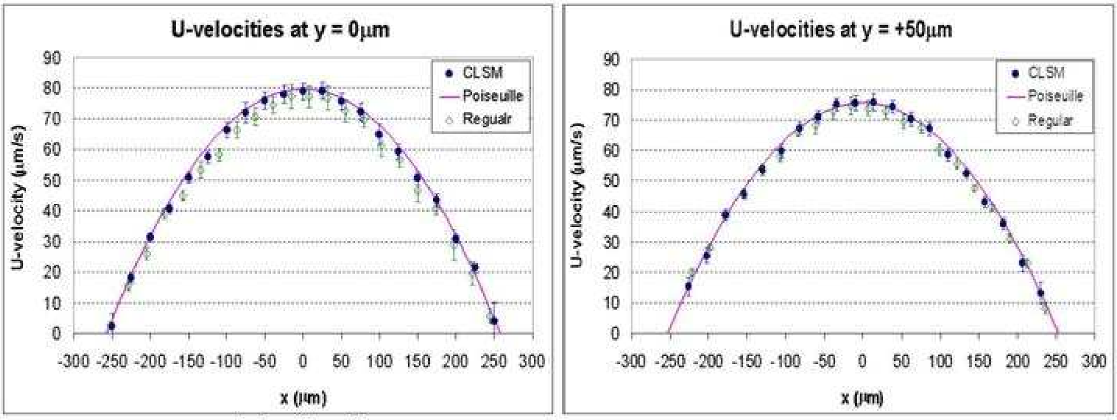

(a) y/R = 0 ***(b) y/R = 0.2***

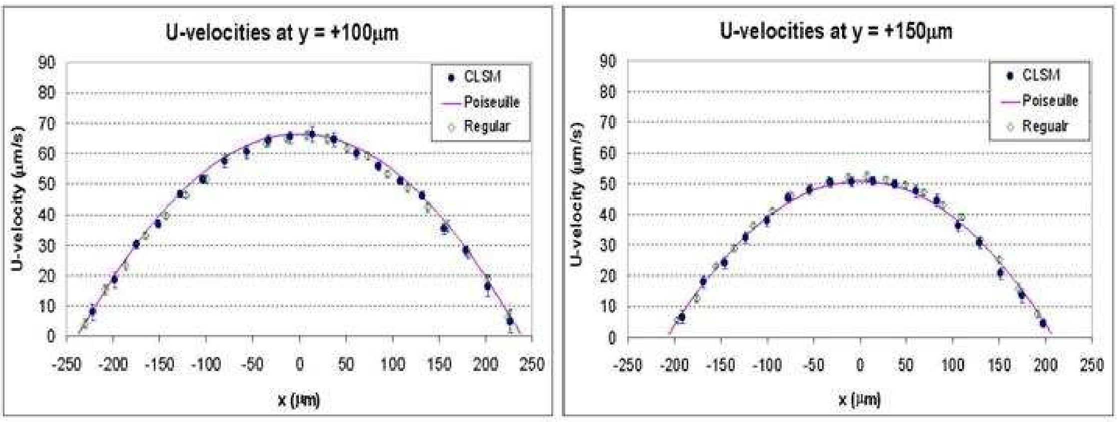

(c) y/R = 0.4 ***(d) y/R = 0.6***

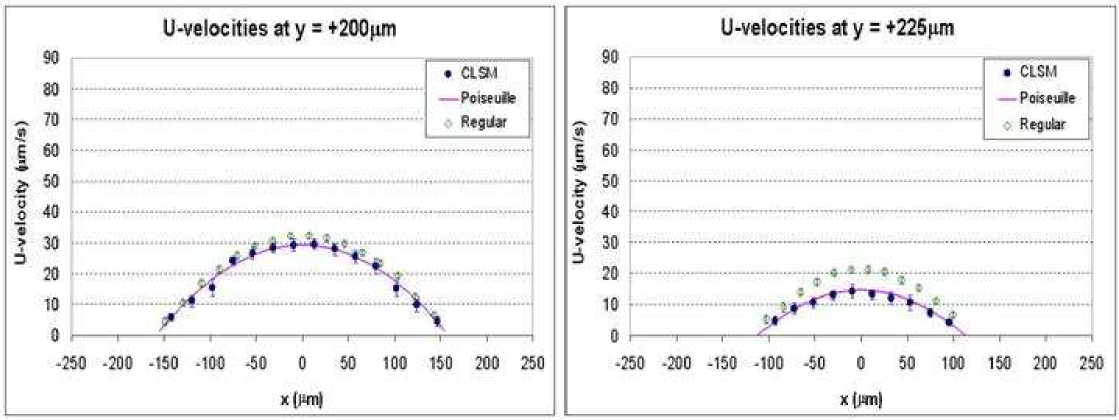

(e) y/R = 0.8 ***(f) y/R = 0.9***

Figure 1.7: Comparison of the velocity profiles measured by the CLSM micro-PIV and by the conventional micro-PIV at different *y*-planes of the 516-μm ID microtube.

(Table 2), whereas the conventional micro-PIV data shows substantial underestimation of –13.3 μm/s from the calculations. We believe that the primary reason for such large discrepancies are attributed to the lack of the optical slicing capability of the conventional microscopy, and the particular reason for the underestimation is due to the negative bias caused by the out-of-focus forward- as well as background blurred images that are moving slower than the fastest center plane flow movement. The centerline velocity biases (x = 0) at other planes of y/R = 0.2, 0.4, 0.6 and 0.8, are measured to –9.7 μm/s, -1.7 μm/s, +1.4 μm/s and +2.3 μm/s, respectively. The magnitude of the negative bias gradually diminishes as being away from the center plane to y/R = 0.2 (Figure 1.6-b), and becomes minimal at y/R = 0.4 (Figure 1.6-c) as supposedly a balance is reached between the positive bias imposed by the faster background flow near the center plane region (y/R < 0.4), and the negative bias due to the slower foreground flow near the microtube edge region (y/R > 0.4).

Further away from the center plane, at y/R = 0.6 and 0.8 (Figure 1.6-d and e), a transition from the negative bias to the positive bias is observed and this is believed to be the fact that as the top inner microtube wall is approached the positive bias by the faster moving background flow in the region of y/R < 0.8 becomes dominant and the negative bias is diminished by the significantly reduced microtube edge region of y/R > 0.8. In contrast, the CLSM-PIV data remain fairly well agreeing with the calculated profiles at all the tested y-planes. The last CLSM profile shown in Figure 1.6-e, measured at only 10-μm away from the microtube edge, starts showing some perceivable degree of deviations and this is possibly due to the more drastic velocity magnitude changes near the wall, even within such a thin optical slice thickness of 2.82-μm, as the velocity gradient becomes steeper as the microtube wall is approached. Additional reason for the enlarged deviations may be attributed to the more substantial lens effect and internal reflection occurred because of the relatively thick lens for the relatively narrow flow region.

For the case of the 516-μm ID microtube, the magnitudes of the negative bias for the conventional PIV results near the center plane (Figure 1.7-a and b) are dramatically reduced in comparison with the previous 99-μm microtube case. As shown in Figure 1.4 and 1.5 as well as discussed previously, the PIV image quality, for both CLSM and conventional cases, is noticeably improved for the larger microtube with the lower magnification (10X Nominal), and the advantageous feature of the CLSM micro-PIV is less pronounced for the objective with low numerical aperture (*NA* = 0.3) used for its imaging. At *y/R* = 0.4 and 0.6 (Figure 1.7-c and d), both the CLSM-data and the conventional PIV data agree well with the theory showing negligible bias. At larger $y/R \geq 0.8$ (Figure 1.7-e and f), however, the positive biasing starts appearing and the bias progressively grows with increasing *y/R*, while the CLSM results stay in fairly close agreement with the theoretical Poiseuille profiles. As the microtube wall is approached, the PIV image quality degradation is amplified because of the dramatically increased lens effect distorting images and the severe image obscuration by the internal reflection. Consequently, the bias of the conventional micro-PIV is amplified whereas the CLSM micro-PIV results more or less consistently show good agreement. This indicates that the optical slicing works more effectively to improve the data accuracy when the PIV image quality is not optimized. Note that the CLSM imaging in general shows more distinctive improvement with higher magnifications and with higher *NA* objectives, and should be even more pronounced with oil-immersion based objectives with *NA* larger than unity.

1.2 Optical Serial Sectioning Microscopy (OSSM)

1.2.1 Background

When low Reynolds number flow velocities are detected by tracing submicron-sized seeding particles, such as in micro-PIV (Particle Image Velocimetry) /PTV (Particle Tracking Velocimetry) applications, the magnitude of the Brownian thermally diffusive motion can be comparable to the convective flow displacement itself. It has been shown that the well-defined thermal correlation of the Brownian motion can be used for nonintrusive temperature measurement schemes. In 1946, Lawson and Long presented a feasibility study that examined how Brownian motion can be used to devise low temperature thermometry. Based on the fact that the kinetic potential energy of molecules, or extremely fine particles, shows an inverse-linear dependence on temperature, namely $\frac{1}{2}kT$, a correlation between Brownian motion and temperature was established.

Olsen and Adrian [21] introduced theoretically the effects of the Brownian motion on the micro-PIV correlation signal peak. They found that Brownian motion diminishes the correlation signal strength and negatively affects the image depth of correlation. By utilizing the cross-correlation peak broadening, which is increased by the Brownian thermal motion, Hohreiter et al. [22] proposed a formidable temperature measurement technique. Sato et al. [23] presented an experimental attempt to take into account the Brownian motion of submicron tracer particles so that their pulsating motion can be detected with unbiased temporal resolution.

In 1905 Einstein presented in his doctoral dissertation an insightful theory calculating Brownian motion of small particles suspended in a fluid. Perrin, in 1908, attempted to verify the theory by painstakingly measuring the time dependence of one and two-dimensional mean square displacements of microscale grains of a known size in a fluid[6] [24]. More recently, the use of video microscopy has allowed two-dimensional tracking of Brownian motion of suspended particles with substantially shorter time intervals than in Perrin's experiment. Calculation of the mean square displacements of the data has shown good correlation with Einstein's theoretical values [25, 26]. It is well known that Einstein's theory predicts the Brownian motion with acceptable accuracy for one- and two-dimensions.

To the authors' knowledge, no attempt to date has been made to track Brownian motion of submicron particles in a fully three-dimensional and simultaneous way. For the case of the near wall region (less that 1µm from the wall), a Ratiometric Total Internal Reflection Fluorescence Microscopy (R-TIRFM) has allowed simultaneous three-dimensional tracking of nanoparticles for their near-wall "hindered" Brownian motion [27]. This paper presents the use of Optical Serial Sectioning Microscopy (OSSM) for detecting three-dimensional "unhindered" or free Brownian motion outside the near-wall region. The OSSM method uses the optical diffraction patterns of focused and defocused images of nanoparticles and compares them to the theoretically predicted patterns so that the location of the particle can be identified with respect to the focal plane of the imaging optics.

---

[6] Both Einstein and Perrin's efforts helped confirming the existence of atoms as real particles, not as hypothetical objects, and both were awarded the Nobel Prize in physics in 1921 and 1926, respectively.

The OSSM technique was originally developed to obtain a 3-D depthwise resolved image in a thick biological specimen [28]. The technique utilizes a standard epi-fluorescence microscopy with a high numerical aperture objective to record and analyze the 3-D diffraction image patterns of small particles [19]. The wave nature of light images a point source to form a diffraction pattern that is longitudinally modulating with respect to the focal plane and laterally modulating with respect to the optical axis. The resulting 3-D image pattern is expressed in a fully analytical form of a symmetric vector function in the absence of optical aberration [29, 30]. However, optical aberrations caused by any non-ideal specimen structures bring about complicated asymmetric image patterns [31]. An experimental verification of the analysis has been conducted by using an advanced video microscopy system [32]. McNally *et al.* [33] applied the Gibson and Lanni's equation to a dry objective system, and measured 3-D intensity profiles of fluorescent microspheres by using a computational optical sectioning microscopy. A similar idea for tracking 3-D particles using off-focus imaging was presented by Speidel *et al.* [34] where an experimental correlation between the diffraction pattern and the defocusing distance was used.

For macro-scale applications using seeding particles on the order of several microns, results showed vivid and bright images accompanying no detectable diffraction patterns and negligible Brownian motion. In such cases, an attempt has been presented by Pereira and Gharib [35] to detect the third velocity component in the line-of-sight direction by using a mask with two or more off-axis apertures. This allows a single image formation for particles located on the focal plane and multiple images for particles located at off-focal planes, which is referred to as Defocusing Digital Particle Image

Velocimetry (DDPIV). The working principle of the technique, however, assumes that the system is free of optical aberrations and diffractions for applications that are not necessarily in microscales, while the OSSM technique is useful for micro/nano-scale applications with optical aberration present.

Therefore, the first goal of this paper is to demonstrate three-dimensional tracking of Brownian motion of submicron tracer particles by analyzing the optical diffraction images taken by OSSM. Measured values of one-, two-, and three-dimensional Mean Square Displacements (MSD) have been compared with the predicted values based on Einstein's theory for the range of temperature from 5 to 70°C. The second goal is to implement a concept for an *in-situ* and full-field mapping thermometry with microscale resolution[7] based on the temperature correlation with the measured Brownian diffusivity of nanoparticles. The experimental data validates the correlations not only for more comprehensive 3-D Brownian motion but also for simpler 1-D line-of-sight Brownian motion.

1. 2.2 Temperature dependence of Brownian motion

Brownian motion refers to the random motion of a small particle suspended in a fluid. This was first observed microscopically by the botanist Robert Brown in 1827 [36]. In 1905 Einstein indicated that this motion is caused by random bombardment of fluid molecules on the suspended particle and that the mean square displacement (MSD) of the particle is the primary observable quantity. The three-dimensional MSD of the random walk traveled by suspended particles is expressed as:

---

[7] The minimum spatial resolution for temperature measurement should be limited by the minimum inter-particle distance with negligible interference, or equivalently ten times of particle diameter.

$$\langle r^2 \rangle = \frac{\sum_{i=1}^{n} r_i^2}{n} = \frac{\sum_{i=1}^{n} (\Delta x_i^2 + \Delta y_i^2 + \Delta z_i^2)}{n} = 6D\Delta t \tag{1.1}$$

where *D* indicates the Brownian thermal diffusivity (or equivalently a diffusion coefficient) of the particle suspended in the fluid and *t* is an observation time interval of each incremental displacement. The observation time interval may be equated to the image frame interval of a CCD camera as long as the frame rate is sufficiently high to discern the minutely changing displacements of the random walk.

Following the well-known Stokes-Einstein equation, the diffusivity is given by

$$D = \frac{\kappa T}{6\pi\mu r_p} \tag{1.2}$$

where is the Boltzmann's constant (1.3805 x 10^{-23} J/K), *T* is the absolute temperature of the fluid, (*T*) is the dynamic viscosity of the fluid, and r_p is the particle’s radius. The viscosity of liquid is primarily a decreasing function of temperature and is expressed as (Fox et al. 2004):

$$\mu = A \cdot 10^{\frac{B}{T-C}} \tag{1.3}$$

where *T* is the absolute temperature of the fluid, and *A*, *B*, and *C* are constant variables that depend on the fluid. For the case of water, *A*, *B* and *C* are known to be 2.414 $\times 10^{-5}$, 247.8, and 140, respectively. Combining Eqs. (2) and (3) gives the diffusivity as a function of the suspension liquid temperature only, as long as the particle size is known, i.e.,

$$D = \frac{\kappa T}{6\pi \left[A \cdot 10^{\frac{B}{T-C}} \right] r_p} \tag{1.4}$$

Figure 1.8 shows the temperature dependence of the diffusion coefficient and of the viscosity of water when they are normalized by D_o and μ_o given at a reference temperature of T = 273K. The intermediate dashed curve shows the gradually increasing temperature dependence of the diffusivity when the temperature dependence of viscosity is neglected while the solid curve shows the dramatic increase of diffusivity when the temperature dependence of viscosity is accounted for. Therefore, the Brownian diffusivity, and the corresponding MSD of a particle with a known size, can be uniquely determined by the suspension temperature. Conversely, by measuring the Brownian diffusivity of the suspended particle, the surrounding liquid temperature can be readily determined.

1.2.3 Point Spread Function (PSF) and Optical Serial Sectioning Microscopy (OSSM)

When a point source or small particle is imaged through an aperture or high-magnification objective lens, the phase modulation based on the wave nature of light forms a spatially distributing diffraction pattern. The three-dimensional diffraction pattern is called a Point Spread Function (PSF) and is generated from stacks of serial optical sections [19]. Another important factor to consider is optical aberrations[8] , which occur when the imaging is conducted under “off-design” conditions. In practice,

---

[8] Optical aberrations can be defined as the departure from the idealized conditions of Gaussian optics. Common optical aberrations can be classified as following: spherical, chromatic, curvature of field, comatic, and astigmatic. Among these aberration, for macroscale applications, the spherical aberration is the most serious in the monochromatic illumination and can be explained by the fact that as light rays emerge from several radial points of a lens they are not converged into one focal plane but focused on different planes along the optical axis which results in blurry images. However, for microscale applications, several factors contributing to additional aberration must be accounted for as described in the text above.

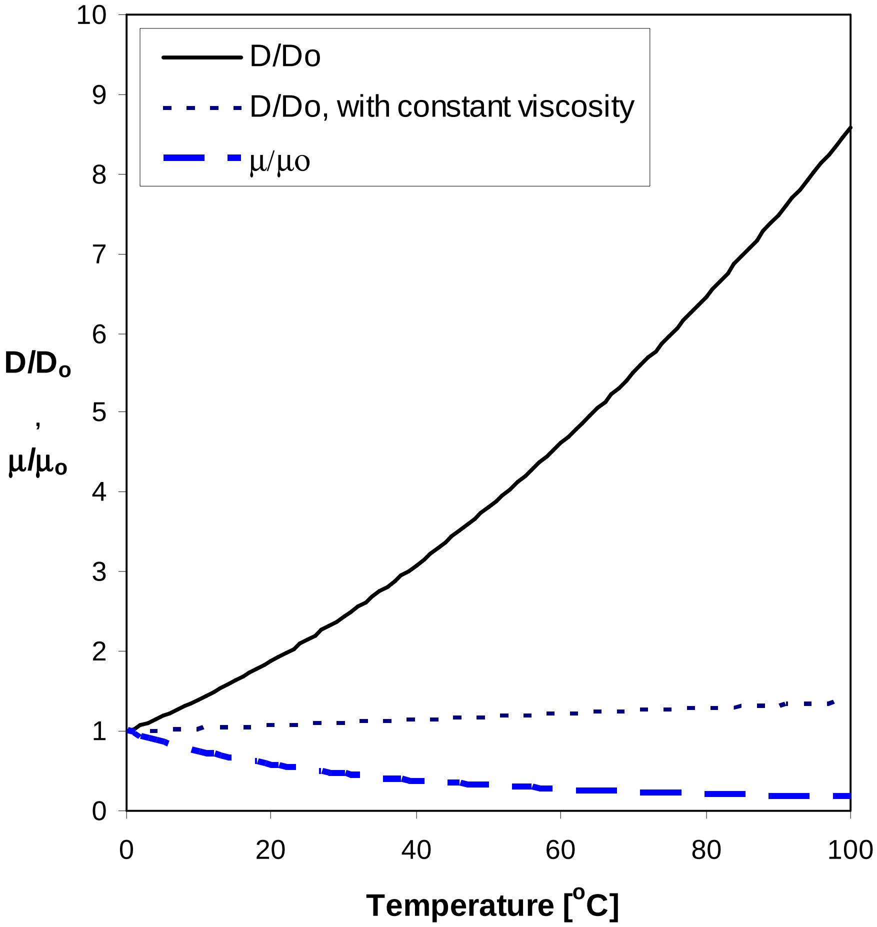

Figure 1.8: Dimensionless diffusion coefficient and fluid viscosity of water as functions of temperature. The reference diffusivity and viscosity values for normalization are taken at T = 273K.

significant aberration is commonly caused by two variables: one, the different refraction indices of the cover glasses and immersion media, and two, the variability in the thickness of the immersion media and cover glass from the specified design values. A monochromatic spherical wave emitting from a point source transverses the entrance pupil of an objective lens and emerges from the exit pupil of the objective lens, and converges towards the back focal point (Figure. 1.9-a). The analytical form of PSF based on the *Huygens-Fresnel Interference Principle* consists of the Bessel function and a sinusoidal complex exponential term, both of which essentially constitute the modulation of PSF in the lateral and in the line-of-sight directions, respectively.

Figure 1.9-a illustrates an aberration-free imaging system. The design conditions stipulate that the light ray from the observation point passes directly through the cover slip of a designed thickness (170 μm in most cases) and an immersion medium having a designed refractive index, and then travels to the detector located on the ideal image plane. The designed conditions of the aberration-free system specify a cover glass of designated refractive index (n_{g*}) and thickness (t_{g*}), and an immersion medium of designated refractive index (n_{i*}) and thickness (t_{i*}). The specimen thickness (t_{s*}) should be zero to ensure the aberration-free imaging. When these conditions are not met, the refracted rays have optical pathways that deviate from the original aberration-free conditions and do not converge to the ideal focal point. In consequence, the refraction due to the index mismatching affects the optical aberration of an objective lens and produces asymmetric diffraction patterns as schematically illustrated in Figure. 1.9-b. Since the aqueous medium of a specimen, in general, has a different refractive index from those of a cover glass and of an immersion medium, most practical cases are subject to

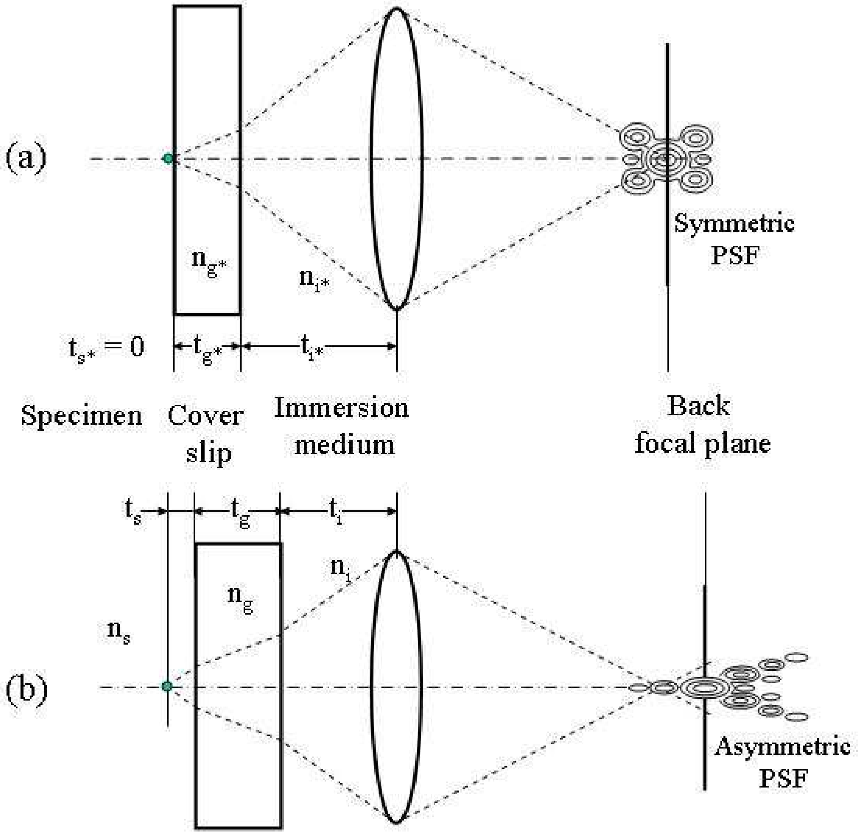

Figure 1.9: Formation of Point Spread Function (PSF): (a) aberration-free imaging to form a symmetric PSF; and (b) aberrated imaging to form an asymmetric PSF.

asymmetric PSF images.

Gibson and Lanni [31] presented a comprehensive form of PSF on a basis of Kirchhoff's diffraction integral formula. The three-dimensional intensity distribution of PSF is expressed in terms of the detector location (x_d, y_d), the numerical aperture of the objective lens (NA), the magnification of the microscopy system (M), and the defocus distance (Δz) as:

$$I(x_d, y_d, \Delta z) = \left| C\int_0^1 J_0\left[k\frac{NA}{\sqrt{M^2 - NA^2}}\rho\sqrt{{x_d}^2 + {y_d}^2}\right] exp\left[jW(\Delta z, \rho)\right]\rho\, d\rho \right|^2 \tag{1.5}$$

where k is the wave number ($2\pi/\lambda$) with λ being the emission wavelength of a point source[9], is the normalized radius in the exit pupil, and $W(\Delta z, \rho)$ is a phase aberration function, which is the product of the Wave Number (k) and optical path length difference[10] (OPD). The three-dimensional PSF of Eq. (1.5) is reduced to the planar Airy function [15] on the focal plane at $\Delta z = 0$[11] and the resulting intensity pattern modulates

---

[9] The Point Spread Function, Eq. (1.5), is constructed based on the ray emission from an infinitesimally small point source and the diffraction pattern is irrelevant to the nanoparticle sizes. The authors believe that 500-nm particles can be considered sufficiently small to be assumed as a point source. In theory, therefore, polydisperse particles do not affect measurements unless their sizes are excessively large. On the other hand, smaller nanoparticles will reduce the diffraction pattern intensity because of their smaller diffraction cross section.

[10] For the complete expression for OPD, see Eq. (4) of Gibsen and Lanni (1991).

[11] Accounting for the axi-symmetric PSF characteristics on the image plane, we set $y_d = 0$ and $\Delta z = 0$, Eq. (1.5) reduces to

$$I(x_d, 0, 0) = \left| C\int_0^1 J_0\left[k\frac{NA}{\sqrt{M^2 - NA^2}} x_d\, \rho \right]\rho\, d\rho \right|^2 \tag{1.6}$$

Using one of the general properties of Bessel functions, called as a recurrence relation, Eq. (1.6) further reduces to in the radial and axi-symmetric directions. The PSF of Eq. (1.5) also modulates in the line-of-sight axial direction as it can be demonstrated for the case of $x_\mathrm{d} = 0$ and $y_\mathrm{d} = 0$[12].

$$I(x_d,0,0) = \left| \frac{C\sqrt{M^2 - NA^2}}{k\,NA\,x_d} \int_0^1 \frac{d}{d\rho}\left[\rho\, J_1\!\left(k \frac{NA}{\sqrt{M^2 - NA^2}}\, x_d\, \rho \right) \right] d\rho \right|^2$$

$$= \left| \frac{C\sqrt{M^2 - NA^2}}{k\,NA\,x_d}\, J_1\!\left(k \frac{NA}{\sqrt{M^2 - NA^2}}\, x_d \right) \right|^2 \qquad (1.7)$$

This is the Airy formula for Fraunhofer diffraction at a circular aperture, as expected. The 1st order Bessel function J_1(a) equals to zero for a = 0, 3.83, 7.02, 10.17, 13.32, and so forth. By converting the dimensionless values using $k\cdot NA/(M^2 - NA^2)^{0.5} = 0.23\text{-}\mu\mathrm{m}^{-1}$ for the given experimental conditions, the corresponding radial x_d's of zero intensities on the focal plane are obtained as 16.7-μm, 30.5-μm, 44.2-μm, and 57.9-μm, respectively. By the way, these values correspond to the magnified dimensions on the back focal (image) plane, and thus, the corresponding physical dimensions on the object plane are 0.42-μm, 0.76-μm, 1.1-μm, and 1.45-μm, respectively.

[12] For $x_d = 0$ and $y_d = 0$, Eq. (2.1) reduces to

$$I(0,0,\Delta z) = \left| C \int_0^1 exp\left[jW(\Delta z,\rho) \right] \rho\, d\rho \right|^2 \qquad (1.8)$$

The phase aberration function is obtained based on the reference of Gibson and Lanni (1991), and expressed as

$$W(\Delta z,\rho) = k\, n_{imm}\, \Delta z \sqrt{1 - \left(\frac{NA\rho}{n_{imm}} \right)^2} \qquad (1.9)$$

where n_{imm} is a refractive index of immersion medium. We set $W(\Delta z,\rho) = \beta$, and substitute $\rho\, d\rho$ into $\beta\, d\beta$. The complex exponential function shall be expressed by trigonometric functions, and Eq. (1.8) is written as

$$I(0,0,\Delta z) = \left| -\frac{C}{(k\,NA\Delta z)^2} \int_a^b \left[\cos(\beta) + i\sin(\beta) \right] \beta\, d\beta \right|^2 \qquad (1.10)$$

Figures 1.10-a and –b show the contour lines in meridional sections of the calculated 3-D intensity distributions from Eq. (1.5) for the design (symmetric) and off-design (asymmetric) conditions, respectively. The point source is located in the left of the plane and the calculations are made for selected experimental conditions, M = 40, NA = 0.75, λ = 515 nm (Green band from an ar-ion laser), and f = 4.5 mm. Both intensity distributions are axi-symmetric along the optical axis since neither astigmatism nor optical coma is considered. A number of concentric fringe rings are presented in the radial section of the intensity distribution, which is more pronounced for the symmetric PSF case. Note that the out-most fringe diameter persistently increases with increasing defocusing distance, as marked by dashed curves, but the negative defocusing for the asymmetric case does not recognizably increase the out-most fringe diameter. The principle of Optical Serial Sectioning Microscopy (OSSM) is based on the determination of the radial intensity profile normal to the meridional plane as a function of Δz. In other words, the relative line-of-sight (z) location of a particle measured from the focal plane can be determined by observing the radial diffraction pattern, in particular the increase in

---

where the integration limits are defined as $a = k\, n_{imm} \Delta z$ and $b = k\, n_{imm}\, \Delta z \sqrt{1 - \left(\frac{NA}{n_{imm}} \right)^2}$. Eq. (1.10) is integrated by parts to give

$$I(0,0,\Delta z) = \left| -\frac{C}{(k\, NA \Delta z)^2} \left[(1 - ib)\exp(ib) - (1 - ia)\exp(ia) \right] \right|^2 \qquad (1.11)$$

Solving Eq. (1.11) for z for the subsidiary minimum intensities gives as 1.5-µm, 3.0-µm, 4.55-µm, 6.1-µm, 7.6-µm, and so on.

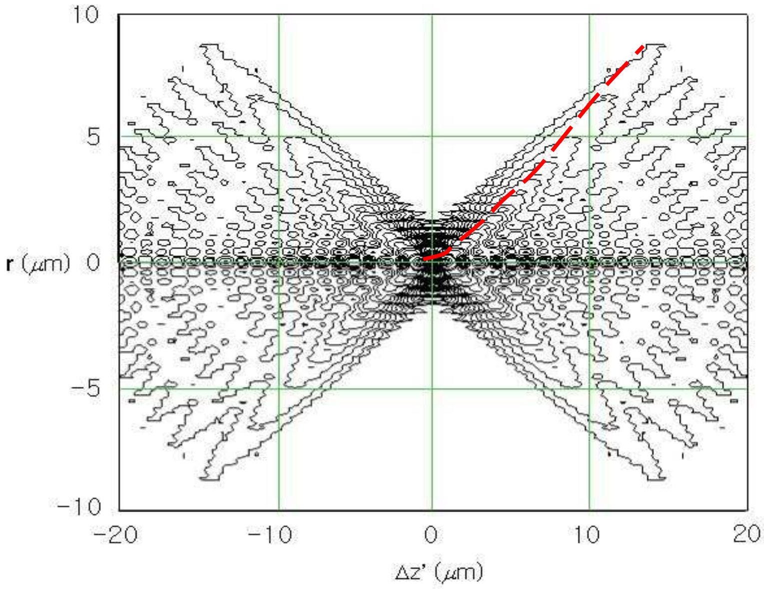

(a) Symmetric PSF

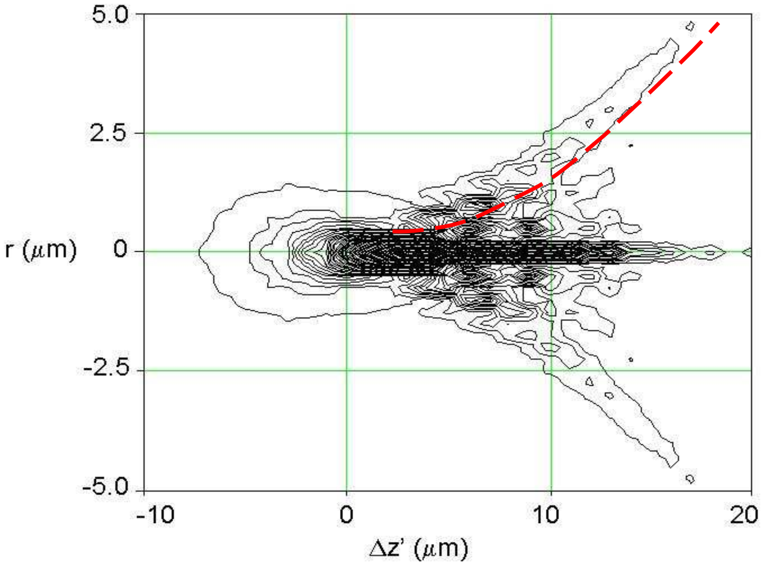

(b) Asymmetric PSF

Figure 1.10: Meridional sections of the 3-D intensity distributions obtained with the theoretical calculation based on Gibson and Lanni [31]. For (a) symmetric pattern, the thicknesses and refractive indices of specimen layers are identical with designed conditions like: $t_s = 0$, $n_s = 1.33$, $t_g = 0.17$ mm, $n_g = 1.522$, $n_i = 1.0$ and t_i = variable (because it is related with z). For (b) asymmetric pattern, a few thicknesses of specimen layers are non-designed conditions like: t_s = variable (because it is related with Δz), $t_g = 0.233$ mm and $t_i = 0.481$ mm.

the out-most fringe radius with an increase in defocusing distance. The out-most fringes are identified with less uncertainty in general for the asymmetric case, because of their brighter and narrower definition.

1.2.4 Experimental Setup

The most crucial part of the experiment is to ensure the calibration accuracy of the OSSM-measured radial intensity profiles in comparison with the calculated intensity profiles based on Eq. (1.5). The OSSM calibration system (Figure. 1.11) consists of an epi-fluorescent microscope (upright Olympus BX 61 Model) with a dry objective lens (40X, 0.75 N.A.), a 1024 x 1024 pixel CCD camera (UNIQ Vision Inc., UP-1830) with a frame grabber at 30 fps (QED-Imaging Inc.), and a 170-μm high calibration chamber. Yellow-green (505/515) fluorescent polystyrene micro-spheres, with a nominal diameter of 500 ± 16 nm and a density of 1.05-g/ml (Molecular Probes Inc.), are used as tracers. The calibration chamber is filled with a water-based solution at a volume concentration of 4×10^{-6} of the seeding particles[13] and the calibration experiment is conducted at the laboratory temperature of 22 °C. Extra care is taken to minimize particle coagulations by dispersing the sample extensively using a sonicator before and after conducting each experiment.

---

[13] The primary merit of the proposed technique is to measure the base fluid viscosity by detecting the temperature (and viscosity) dependence of the Brownian motion of seeded nanoparticles at a minimum concentration that provides statistically acceptable number of particle images. The average inter-particular distance is calculated to 31-μm that is larger than 60-times of the particle diameter. Thus, the particle-to-particle interaction effect as well as the particle interaction with fluid is considered negligibly small [37] W. B. Russel, D. A. Saville, and W. R. Schowalter, "Colloidal dispersions " *Cambridge University Press,* pp. 21-63, 1989.. On the other hand, the technique can also be applied to measure the resulting viscosity of a thick slurry sample where the particle-fluid interaction is not trivial as long as a calibration equation for temperature-viscosity correlation is available.

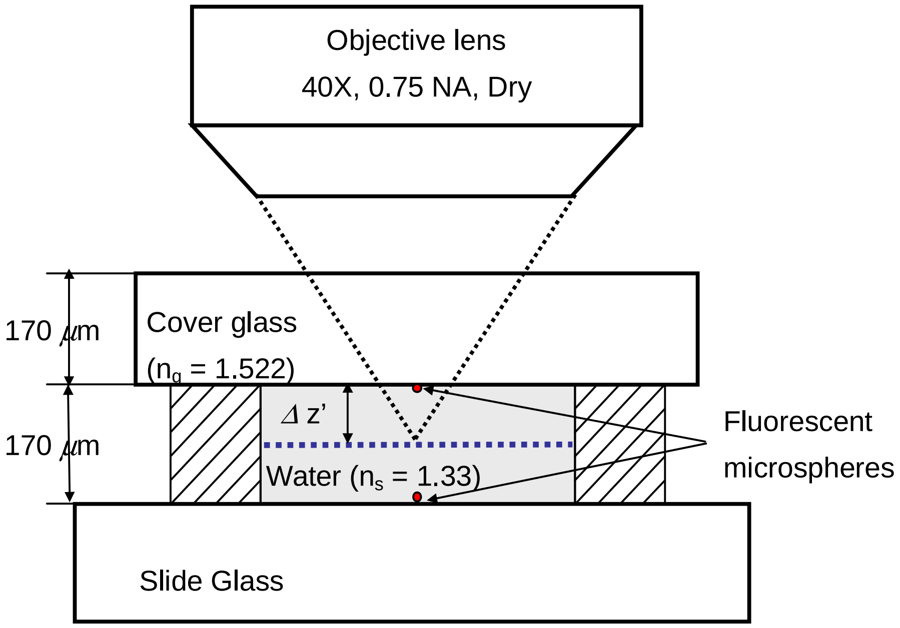

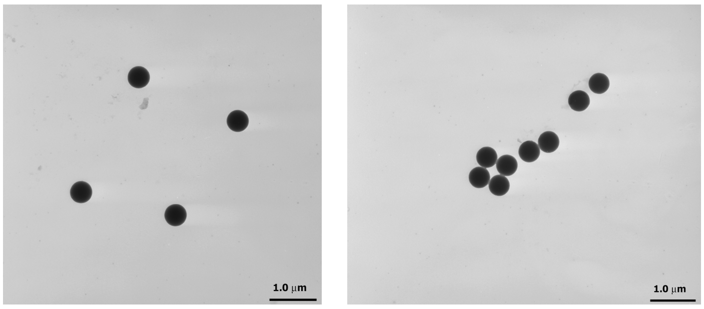

{TEM Images}

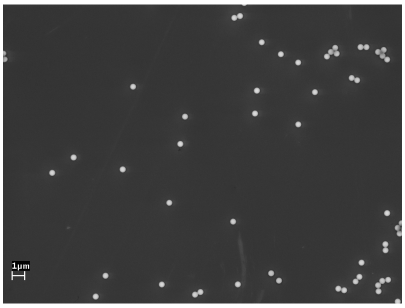

{SEM Image of 500-nm particles}

Figure 1.11: Schematic of a test specimen for measuring both symmetric and asymmetric PSFs in the OSSM using 500±16 nm nominal diameter nanoparticles.

When a test particle is located at the top glass plate, the chamber is to provide a nearly aberration-free condition. This in turn will form a symmetric PSF in the absence of the specimen thickness (t_{s*}), which is the primary source of aberration for most cases. On the other hand, when a test particle is located at the bottom plate, the thickness (170-μm) of the specimen creates a substantial aberration effect to make asymmetric diffraction patterns necessary for the particle. Note that Δz’ in Figure. 1.11 is the location of the actual imaging plane that is compensated for by the refractive index mismatching occurring throughout the imaging rays whereas Δz in Eq. (1.5) is the mechanical movement of the objective controlled by a stage with 1-μm resolution. Thus, the defocusing distance (Δz’) is varied with 1.33-μm resolution. For the case of the top particle, the calibration is conducted to establish a correlation of the symmetric PSFs with a negative defocusing distance for particles located at a shorter distance than the focal distance as the objective is lowered from the initial focusing point of the top surface. For the case of the bottom particle, a calibration for the asymmetric PSF is conducted for a positive defocusing distance for particles located beyond the focal plane as the objective is lifted from the bottom focal plane.

The second test chamber is designed to measure the thermal effect on the particle’s Brownian motion. The chamber is geometrically similar to the calibration chamber. One change however is that a steady temperature condition is provided for the test fluid by embedding the test chamber in a copper block with a coolant passage built in. This enables the coolant to be circulated to and from a constant thermal bath. A thermo-couple probe is flush-installed at the inside bottom surface to monitor the liquid temperature. Another important modification is that the test chamber uses an off-designed cover glass of 223-μm thickness in order to construct asymmetric PSFs in a more pronounced way. As discussed in section 3 more pronounced PSFs provide less uncertainty and higher definition. The focal plane of the objective lens is fixed to the top glass-water interface and any suspended particles can generate asymmetric PSF images for all experiments. This is possible because of the off-designed cover glass and the suspension medium (water) of mismatching refractive index. It is more realistic to assume that a nonzero specimen distance (t_s) is the condition in most practical imaging cases as particles are suspended and imaged in a liquid medium.

1.2.5 Temperature correlation of Brownian motion

Figure. 1.12. shows temperature correlations of the Brownian MSD measurement data for 500-nm particles in a suspension for the temperature ranging from 5 to 70°C. The three primary curves, shown by thicker lines, represent theoretical predictions for the 3-D MSD's of $6D\Delta t$, 2-D (*x*-*y*, *x*-*z*, or *y*-*z*) MSD's of $4D\Delta t$, and 1-D (*z*) MSD of $2D\Delta t$, respectively. The primary uncertainties[14] for the calculated MSD values are believed to be due to the diameter uncertainties (500 ± 16 nm). A pair of dashed curves for each primary curve shows the uncertainty range. Each symbol represents an ensemble-averaged MSD for seven arbitrarily selected particles that are tracked for one second at each temperature condition, i.e., a total of 210 data realizations for each data point. The error bars indicate a 95% confidence range of the measured data or MSD, assuming a Gaussian distribution. The ensemble-averaged MSD agree fairly well with the well-known Einstein's predictions.

---

[14] See Section 5.5 for more detailed uncertainty estimations including other potentially contributing parameters, such as the liquid temperature and viscosity as shown in Eq. (1.2).

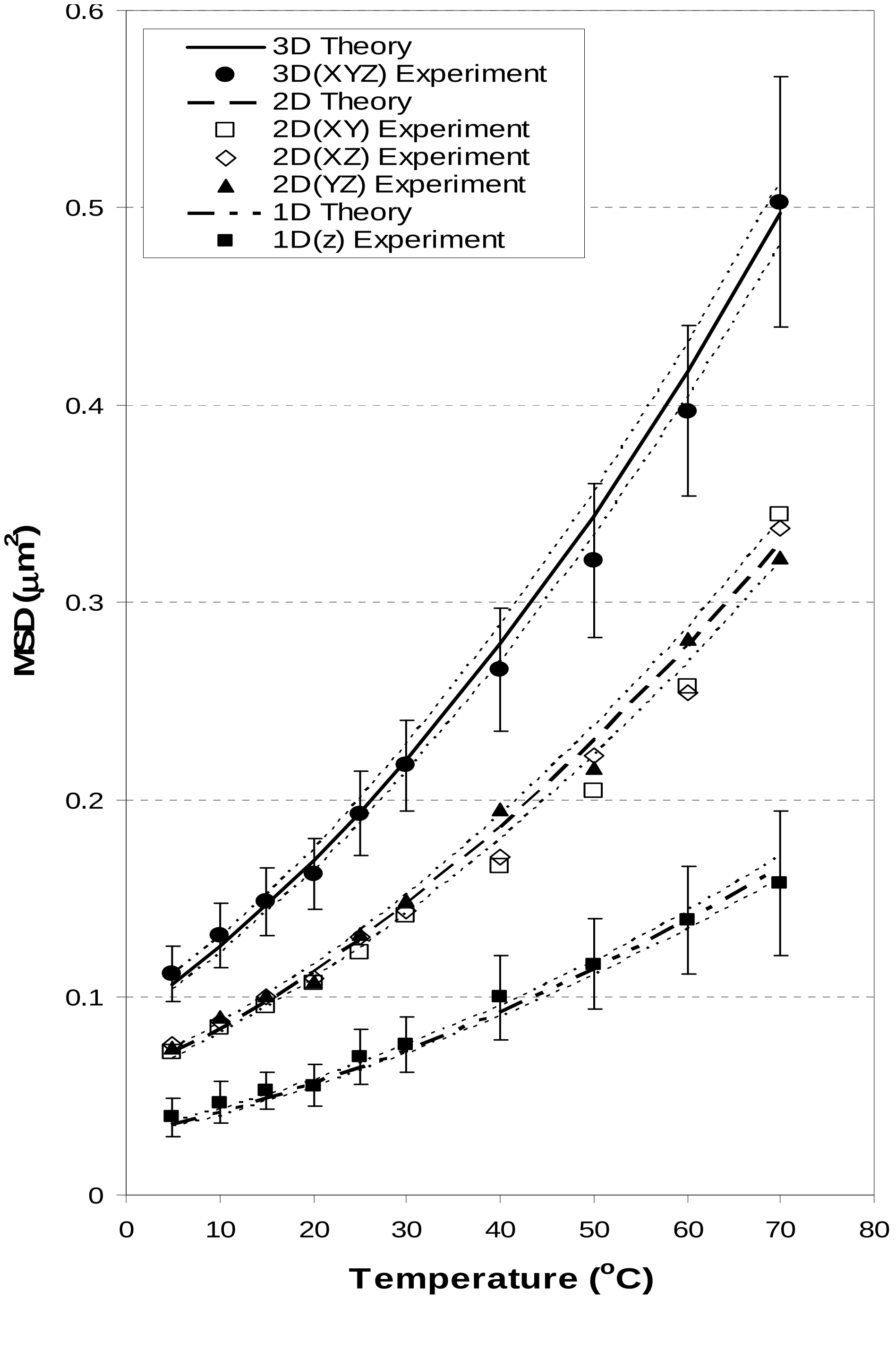

Figure 1.12: Theoretical and experimental mean square displacements (MSD) for all 203 steps of 7 particles are shown in terms of temperature and dimension. The dashed lines near theoretical curves of each dimension mean a range of MSD which is caused by the uncertainty (3.2%) of particle’s diameter. The error bars indicate a 95% confidence interval of measured MSD.

Table 1.3 shows both the magnitudes of the difference between the predictions and measured values of MSDs (|Theory-Data|) in nanometer units and the percentile differentials, which is defined as (100% x |Theory-Data|/Data). The magnitudes of the difference for the 1-D, 2-D and 3-D cases show a gradual increase from |Theory-Data| = 3.6nm, 7.3 nm to 8.2 nm primarily because of the increasing magnitudes of MSD with increasing dimensions. Note that the normalized percentile differentials decrease from 5.55%, 4.26%, to 3.11% with increasing measurement dimensions and MSD magnitudes. Henceforth, it can be said that the 3-D MSD detection as well as the 1-D (z) MSD detection persistently correlate well with the theory in predicting the liquid temperature. Therefore, one suggestion is that the single component detection of the line-of-sight Brownian motion using the OSSM technique may prove to be an effective new tool in nonintrusively mapping the temperature fields for nanoparticle suspension fluids. This would negate the need to use the more cumbersome effort of tracking the two-dimensional Brownian motion, which will be needed to constitute the 3-D MSD data. *A priori* is the temperature dependency of the fluid viscosity; such as given in Eq. (1.3), in order to provide the temperature dependence predictions of the Brownian diffusivity.

1.3 Total Internal Reflection Fluorescence Microscopy (TIRFM)

1.3.1 Background

One crucial phenomenon of particular importance at micro/nano-scale levels is Brownian diffusive motion of extremely small particles. This diffusion is random by nature in that a fine particle diffuses as a result of random collisions by the aggressive thermal motions of surrounding fluid molecules.

Table 1.3 Calculated Brownian Mean Square Displacements (MSD) of 500-nm diameter fluorescent spheres suspended in water and corresponding ensemble-averaged measurement results for 1-D, 2-D and 3-D MSD detections. (MSD theory and data are in μm^2.)

Suspension Temperature		**1-D MSD**	**2-D MSD**			**3-D MSD**
		Z axis	XY Plane	XZ Plane	YZ Plane	XYZ volume
5°C	Theory	0.036	0.072			0.107
	Data	0.039	0.072	0.077	0.074	0.112
	Difference (%)*	8.33	0	6.94	2.78	4.67
10°C	Theory	0.042	0.084			0.126
	Data	0.047	0.085	0.088	0.09	0.131
	Difference (%)	11.90	1.19	4.76	7.14	3.97
15°C	Theory	0.049	0.098			0.147
	Data	0.053	0.096	0.1	0.101	0.148
	Difference (%)	8.16	2.04	2.04	3.06	0.68
20°C	Theory	0.057	0.113			0.17
	Data	0.056	0.107	0.11	0.108	0.163
	Difference (%)	1.75	5.31	2.65	4.42	4.12
25°C	Theory	0.065	0.129			0.194
	Data	0.07	0.123	0.13	0.133	0.193
	Difference (%)	7.69	4.65	0.78	3.10	0.52
30°C	Theory	0.073	0.147			0.22
	Data	0.076	0.142	0.144	0.149	0.218
	Difference (%)	4.11	3.40	2.04	1.36	0.91
40°C	Theory	0.093	0.186			0.279
	Data	0.1	0.166	0.171	0.195	0.266
	Difference (%)	7.53	10.75	8.06	4.84	4.66
50°C	Theory	0.115	0.23			0.344
	Data	0.117	0.205	0.222	0.216	0.322
	Difference (%)	1.74	10.87	3.48	6.09	6.40
60°C	Theory	0.135	0.278			0.417
	Data	0.139	0.258	0.255	0.282	0.397
	Difference (%)	2.96	7.19	8.27	1.44	4.80
70°C	Theory	0.16	0.33			0.497
	Data	0.158	0.345	0.338	0.323	0.503
	Difference (%)	1.25	4.54	2.42	2.12	1.21
Average Difference (nm)		**3.6**	**7.3**			**8.2**
Percentile Average Differential		**5.55%**	**4.26%**			**3.11%**

*Difference (%) = 100 x │Theory-Data│/Theory

History of published observation of Brownian motion goes back to Gray [38], who, using a Plano convex lens, first identified the irregular motion of a small glass globule suspended in a fluid. In 1828, the botanist Robert Brown at first presumed a "living" origin of the motion, but eventually showed that an irregular motion of "inorganic" grains was also present [39]. The first quantitative examination of Brownian motion was completed by Gouy, who demonstrated that the motion was not caused by any external vibration or surface tension but by the thermal motion of the solvent molecules [40]. He also showed that Brownian motion of colloids decreased with increasing particle size and solution viscosity.

Albert Einstein used the molecular-kinetic theory proposed by Boltzmann to obtain an expression for the diffusion coefficients of suspended particles in liquid in his well-known doctoral dissertation, "Annus Mirabilis," published in 1905 [41]. Einstein was then able to evaluate the mean square displacement in terms of Avogadro's number, temperature, particle size, and fluid viscosity. Following this theoretical prediction, Jean Perrin, in 1908, also re-published in 1990, was able to confirm Einstein's theory experimentally by measuring the tangential MSD of colloids of a known size in a fluid for different sampling time intervals [24].

While the Stokes-Einstein diffusion theory assumes free or unhindered Brownian motion, because of the hydrodynamic hindrance occurring from the no-slip boundary condition, the theory breaks down as particles approach a solid surface. The idea that the particle motion remains randomly isotropic is no longer valid, as the dynamics of particle motion become non-isotropic and the average particle displacement deviates from the Stokes-Einstein theory [42]. The presence of a solid surface, therefore, necessitates a correction of the Stokes-Einstein diffusion coefficient. Considering the slow viscous motion of a sphere in a quiescent viscous fluid in the near-wall region, Goldman et al. analyzed rotational and translational motion close to the wall using an asymptotic solution of the Stokes equation, and they derived a correction term for the hindered particle movement parallel to the plane wall [43]. Brenner, under the hypothesis that there is no relative motion at the fluid-solid interface, i.e. no-slip condition, provided an analytical expression in the form of an infinite series to account for another correction term for motion normal to the solid surface [44].

Bevan and Prieve [45] experimentally examined hindered Brownian motion of a 6.24 μm diameter sphere by measuring scattered light from the particle surface using prism-based total internal reflection microscopy (TIRM). Similarly, Pagac et al [46] applied an external radiation force, using a laser at varying power levels, to 7.5-μm and 15-μm diameter spheres in order to measure the average hindered mobility at multiple heights. For the effective examination of hindered Brownian motion of small particles, total internal reflection fluorescence microscopy (TIRFM) has proven to be very useful. Kihm et al. conducted three-dimensional particle tracking for 200-nm fluorescent spheres under the near-wall hindered Brownian motion using the ratiometric analysis of TIRFM, also known as R-TIRFM [27].

Furthermore, Banerjee and Kihm[47] attempted to measure hindered Brownian motion data of the particles and were able to show the compatibility of their data with the aforementioned theories[42, 43]. Note that only averaged values of Brownian mean square displacements (MSD’s) are presented over all elevations sampled. For more appropriate and meaningful validation of the theories, experiments will be necessary to obtain spatially resolved, or layered parallel to the wall, distributions of hindered Brownian motion as functions of height from the solid surface.

The scope of the present study is to experimentally examine the hindered Brownian motion of nanoparticles parallel and normal to the solid surface by measuring their mean square displacements (MSD’s) and comparing the results against the theories for validation. Using the R-TIRFM technique, multi-layered MSD’s are obtained at 25-nm increments from the solid surface for the case of three different polystyrene fluorescent nanospheres (SG = 1.055) 100, 250, and 500 nm in radii.

1.3.2 Theory

A light beam propagating through an internal medium with a higher refractive index (n_i) is refracted, according to Snell's Law, when it encounters a boundary to an external medium with a lower refractive index (n_t). At ray incident angles larger than the critical angle $\theta_c = \sin^{-1}(n_t / n_i)$, light is completely reflected at the interface as the total internal reflection condition prevails at least from a macroscopic point of view. From a microscopic point of view, a portion of the incident light penetrates through the interface into the external medium and propagates parallel to the surface in the plane of incidence, creating an electromagnetic field in the external medium adjacent to the interface. This field, termed an *evanescent wave field*, is capable of exciting fluorescent particles residing in the effective region very near the interface, within less than 1-µm from the interface. The evanescent wave intensity I decays exponentially with the normal distance z measured from the solid wall located at z = 0 [15].

$$I(z) = I_0 \exp\left(-\frac{z}{z_p} \right) \tag{1.12}$$

where I_o is the incident light intensity at the interface, and the penetration depth (z_p), at which I/I_o = e^{-1}, is determined by the incident wavelength in a vacuum (λ_o) and the refractive indices of the internal and external mediums (n_i, n_t), as

$$z_p = \frac{\lambda_0}{4\pi\sqrt{n_i^2 \sin^2\theta - n_t^2}}\ . \tag{1.13}$$

1.3.3 Experimental Setup

Figure 1.13 presents the experimental schematic using an objective lens-based TIRFM system that allows a substantially enhanced signal-to-noise level in the resulting images and is more accessible and flexible when compared to a prism based system [48]. The system consists of an oil immersion 60X TIRF objective lens with NA = 1.45, an Olympus Model IX-50 inverted microscope with a TIRF illumination light guide, a 10 mW Ar-ion CW laser tuned to a wavelength of 488 nm, and a Hamamatsu 14-bit electron multiplier (EM) CCD digital camera having both functions of a cooled and intensified-CCD. The total magnification used in the current TIRFM experiment is 90x, resulting from using a 60x TIRF objective lens, a 0.3x lens in the U-PMTVC, and a 5x PE lens in the IX-SPT. The illumination kit provides precise control of the incident angle to a high degree of accuracy, approximately ± 0.16°, resulting in considerable improvement in the sensitivity of the penetration depth, thus greatly reducing systematic errors.

Fluorescent particles located in the near-wall region are excited by the evanescent wave illumination field. The spatially distributed emission intensity signal[49] of the fluorescent particles, F, is given by:

$$F(x, y; z_p) = \varepsilon I_o(x, y; z_p) \int_0^{\infty} [Q(z)P_D] C(x, y, z) e^{-\frac{z}{z_p}} dz \tag{1.14}$$

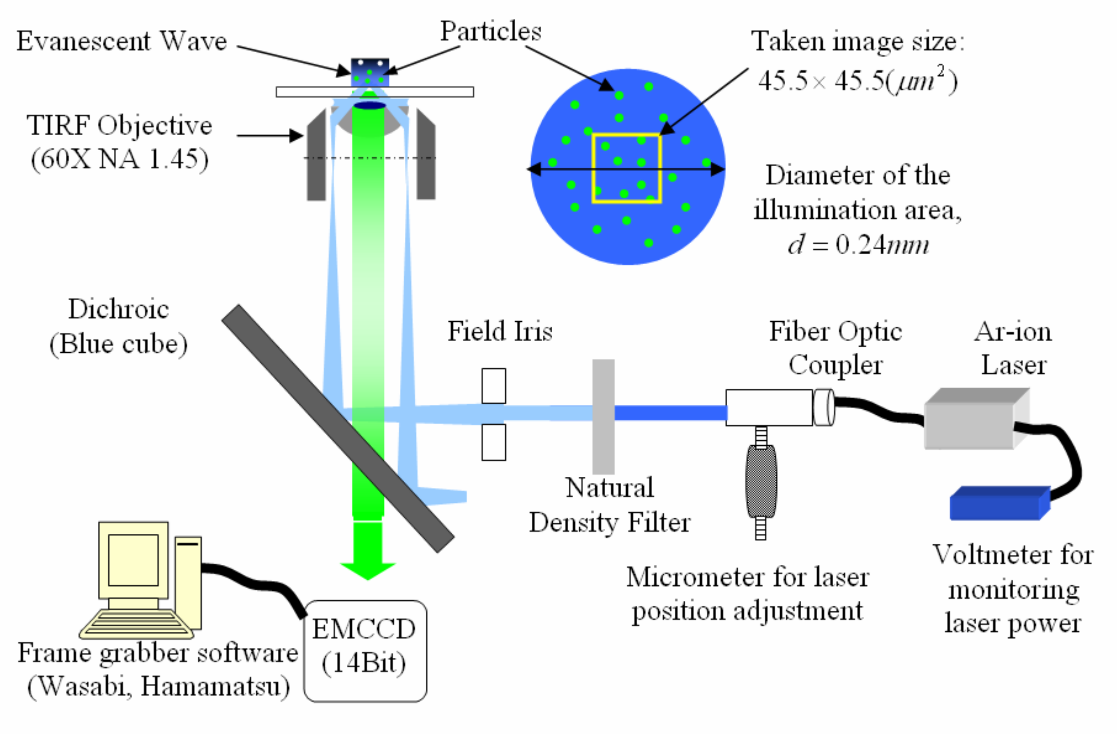

Figure 1.13: Schematic of TIRFM system with a fiber-optic illumination kit.

where ε is the quantum efficiency of the imaging system, $Q(z)$ is the collection efficiency of the objective lens defined as the collected power of the CCD divided by the total emitted power of the particle [50, 51], and P_D is the detection probability that can be assumed to be 1 in most cases.

The two-dimensional fluorescence intensity distributions are predicted as a function of *x* and *y* in the projected area of a single fluorescent particle and the z-integration is essential to account for the resulting fluorescence emission from the three-dimensional (spherical) fluorophore distribution *C*(*x*,*y*,*z*) within a single fluorescent particle. This is necessary to more accurately describe the resulting fluorescence intensity since the resulting intensity is determined from integrated contributions of all the fluorophores contained in the fluorescent particle. The *x-y* integration is conducted later on and is shown in detail in this paper [49]. After performing substantial mathematical manipulations, the normalized intensity [49] detected by the CCD at a given distance from the surface, *h*, is given as:

$$I_n(h,R,c) = 4\pi c z_p^3 \left[\left(\frac{R}{z_p} \right) \cosh\left(\frac{R}{z_p} \right) - \sinh\left(\frac{R}{z_p} \right) \right] e^{-\frac{h}{z_p}} . \qquad (1.15)$$

Though it is possible to determine the absolute elevation *h* of a particle using Eq. (1.15) alone, in practice, it becomes very difficult due to the fluorescence concentration function *c*, which is difficult to measure and rarely known. In order to eliminate this unknown parameter, a ratio of two different intensities can be taken from two different particle images so that the relative distance can then be calculated as:

$$RaInt = \left(\frac{I_N^1 \left(h_1, R, c \right)}{I_N^2 \left(h_2, R, c \right)} \right) = \exp^{\left(-\frac{\Delta h}{z_p} \right)} . \qquad (1.16)$$

Now, by taking a ratio with respect to a particle image with maximum intensity, which is assumed to be attached to the solid wall at h = 0, the temporally and spatially varying elevations of each particle can be readily determined. The ratiometric calculation, Eq. (1.16), uses the maximum pixel intensity near the center of each particle image, and the resulting particle location corresponds to the bottom of each spherical particle. The reference maximum intensity is based on the averaging of at least 100 particles, and the total data points used for 100, 250, and 500 nm radius particles are 87360, 50568, and 63336, respectively. This average was obtained by placing each particle size in 100mM of NaCl solution, which essentially eliminated the double layer causing many of the particles to stick to the surface of the cover slip. The incident angle ($\theta_i = 62.5^\circ$) for determining the reference intensity is the same as that used for the Brownian motion tests.

A similar method for determining particle elevation using intensity measurements detected by a CCD is presented by Wu and Bevan[52]. However, in this paper elevations are calculated, for larger 2-µm diameter non-fluorescent particles, by measuring the scattering intensity of the evanescent wave rather than a fluorescent signal. Schumacher and van de Ven measured the scattering intensity of multiple nano-particles (46.2 nm in diameters), using a photon correlation spectrometer, to examine DLVO curves [53].

1.3.4 Near-Wall Hindered Brownian Diffusivity

Figure 1.14 shows near-wall tangential MSD data measured for nanoparticles of three different radii (100, 250, and 500 nm), separately suspended in a 10 mM saline solution. Each data point represents an average of 80 or more data realizations for the corresponding fluid layer of 25-nm thickness. Good agreement of the measured MSD's with Goldman et al.'s theory validates the predicted near-wall hindrance coefficients for the case of tangential Brownian motion of nanoparticles.

The intrinsic nature of Brownian motion is examined based on the linearity of MSD with respect to the sampling time interval at a constant diffusivity condition. Figure 8 illustrates correlations between measured MSD values and the time intervals for an arbitrarily selected layer between 200 and 225 nm elevations. The straight dashed lines represent the near-wall hindrance theory by Goldman et al.[43] The Brownian diffusivity for a given particle size, or equivalently, the correlation slope in Figure 1.15 is constant, as the fluid properties remain unchanged within the 25-nm thick layer. Though not repeatedly shown, linearity up to a five-time longer sampling period is observed at other elevations for the three tested particle sizes. This validates the measurement accuracy of the TIRFM tracking of the Brown motion of nanoparticles.

Avogadro's number and the Boltzmann constant are calculated from the measured MSD's for further validation of the measurement accuracy [54]. The Boltzmann constant k can be calculated from

$$MSD \equiv \left\langle \left(X(t) - X(0) \right)^2 \right\rangle = 2 D_H \Delta t = \frac{2kT}{3\pi \mu d_p \lambda_{//}} \Delta t \quad , \qquad (1.13)$$

and Avogadro's number is calculated from the relation of $k = R/N_A$, where the universal

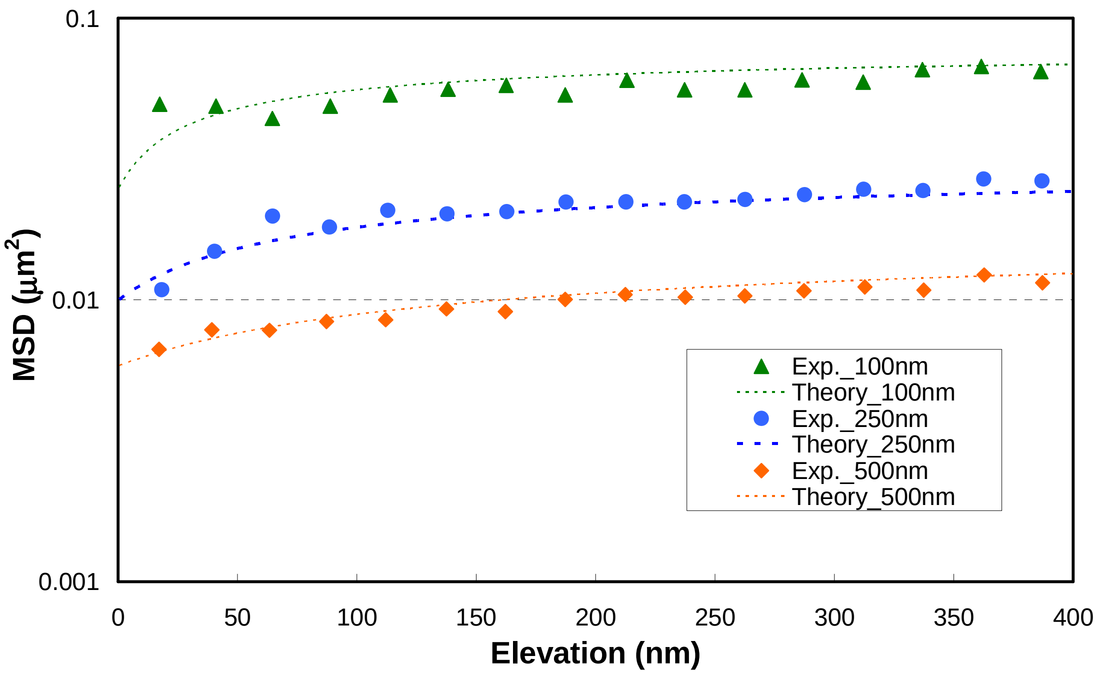

Figure 1.14: Comparison of measured and theoretical two-dimensional tangential mean square displacements (MSD's) at 10 mM salinity. Δt was set at 17.92 ms for 100-nm and 250-nm radius particles and at 20.96 ms for 500-nm radius particles.

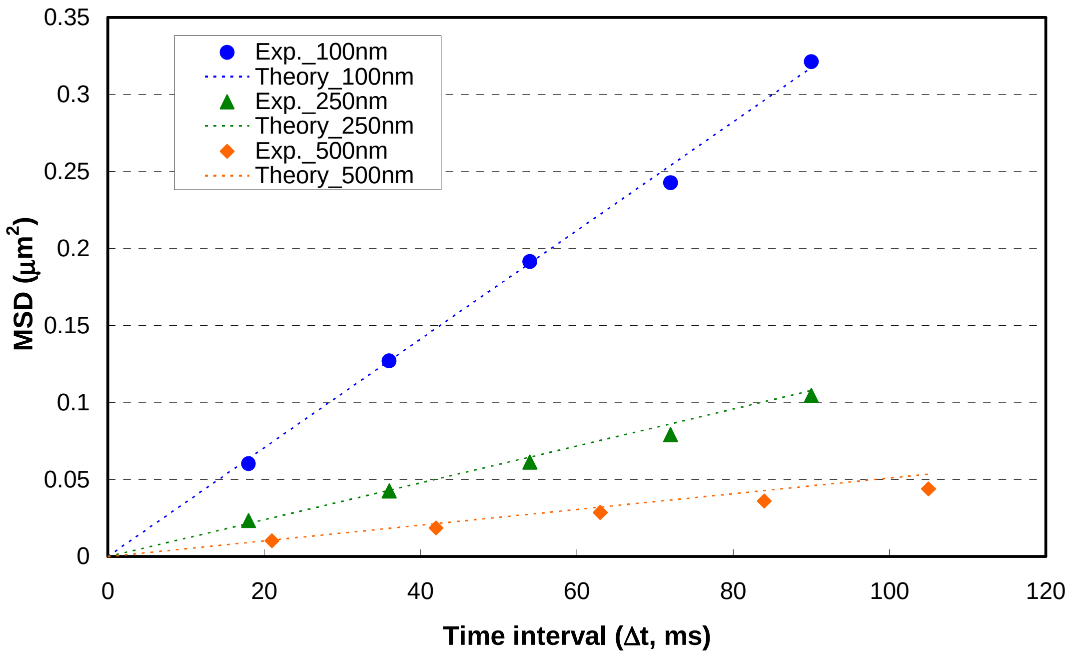

Figure 1.15: Mean square displacement in terms of time interval (Δt) for the 200 ~ 225 nm band, which includes the penetration depth of 202-nm, where the theoretical equation of tangential MSD is expressed as $2D\Delta t$.

gas constant $R = 8.3144\ \mathrm{J/K \cdot mole}$. X(t) and X(0) represent particles locations at two different times. As summarized in Table 1.4, the experimentally extrapolated values closely estimate Avogadro’s number and the Boltzmann constant.

1.4 Epi-Fluorescence Microscopy

Fluorescence microscopy was developed in the early part of the 20th century. The basic function of the fluorescence microscope is to deliver excitation energy to the fluorescing species in the specimen and to separate the much weaker emitted fluorescence light from the brighter excitation light. In doing so, only the emitted light reaches the detector and a high contrast image is generated. The fundamental main components of a fluorescence microscope are (1) excitation light sources, (2) wavelength selection devices, (3) objectives, (4) detectors, and (5) stages and specimen chambers.

Figure 1.16 shows two different microscopic techniques, DICM which will be shortly explained and epi-fluorescence microscopy, to examine apoptotic morphology change in HCT116 (colorectal cancer) cells treated with 30 μM of silindac sulfide. Silindac sulfide is a nonsteroidal anti-inflammatory drug or NSAID. Live cells are stained using LavaCell for 6 hours in an incubator (37°C and 5% CO_2) and treated with complete medium containing 30 μM of silindac sulfide. Morphology changes become more apparent with time as some cells tended to shrink even after 1 hour of treatment. Furthermore 6 hours after treatment, all the cells shrunk and become sphere shapes as well as has another characteristic morphological change associated with apoptosis such as membrane blebbing [55-69]. It is known that when adherent cells enter apoptosis, their attachment to the extracellular matrix becomes weakened and they retract, probably as a result of a loss of focal adhesions and membrane blebbing is normally transient and is

Table 1.4 Extrapolated Avogadro's numbers and Boltzmann constants.

Particle radius (nm)	Avogadro's number (atoms/mole)	Boltzmann constant (J/K)
100	$(5.834 \pm 0.24) \times 10^{23}$	$(1.427 \pm 0.05) \times 10^{-23}$
250	$(6.61 \pm 0.25) \times 10^{23}$	$(1.259 \pm 0.04) \times 10^{-23}$
500	$(7.34 \pm 0.31) \times 10^{23}$	$(1.134 \pm 0.04) \times 10^{-23}$
Reference	6.0231×10^{23}	1.3807×10^{-23}

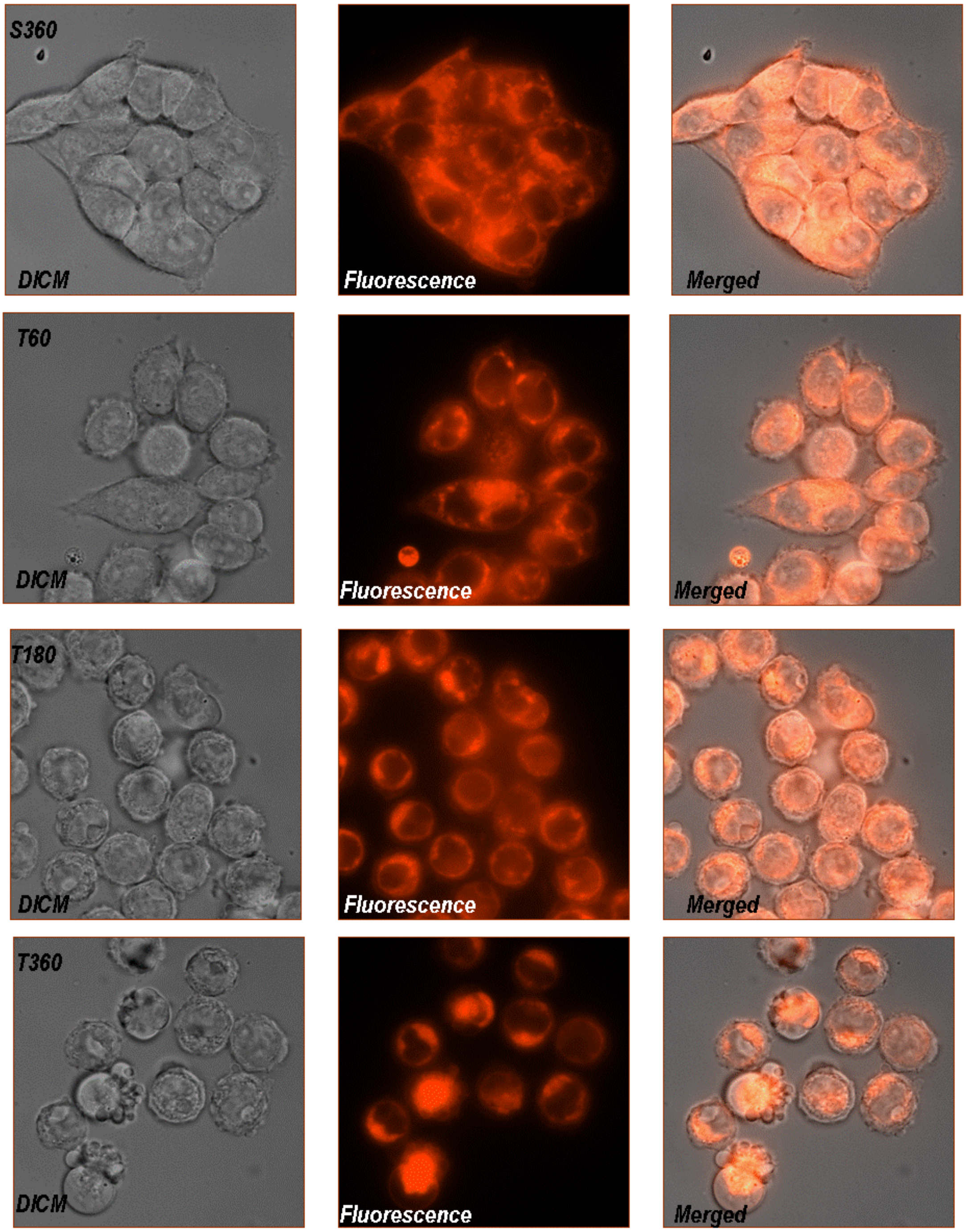

Figure 1.16: Time-lapse epi-fluorescence images of HCT116 colorectal cancer cells under Sulindac Sulfide.

followed by the appearance of other features of apoptosis and often by cell fragmentation.

1.5 Phase Contrast Microscopy (PCM)

In bright field microscopy (BFM), specimens are imaged by recording the intensity (amplitude) of the light passing thorough the specimen at the back focal plane of the objective. However transparent specimens, also referred to as phase specimens[15] (transparent specimens), such as living cells, thin tissue slices, and organelles, are effectively undetectable in BFM as there is little change in the intensity of the incident light as it passes through the specimen. Thus phase contrast microscopy (PCM), differential interference contrast microscopy (DICM), and other contrast-enhancing techniques, which measure phase shifts rather than intensity are needed.

The general idea in phase contrast microscopy is to transform phase shifts between undeviated light and diffracted light, which passes through a specimen, into intensity changes that can be seen and recorded by CCD's. Assume "s" is a surround (undeviated, undiffracted, zeroth-order) wave, "d" is a diffracted (deviated) wave, and "p" is a resultant particle wave as defined in equation 1.

$$\vec{p} = \vec{s} + \vec{d} \qquad (1.18)$$

The schematic for BFM in Figure 1.17 (a) shows that a diffracted (d) wave having a very low amplitude and small (or nonexistent) phase shift results in a particle (p) wave

---

[15] Unstained specimens that do not absorb light are called phase specimens, or transparent specimens, because they slightly alter the phase of the light diffracted by the specimen, usually by retarding such light approximately $\lambda/4$ as compared to the undeviated direct light passing through or around specimens. The human eye is only sensitive to difference in amplitude (brightness) or wavelength (color) not to differences in phase. However there are no microscopic specimens to create appreciable change in intensity or color of the light falling through them. The changes in phase only can be caused through specimens.

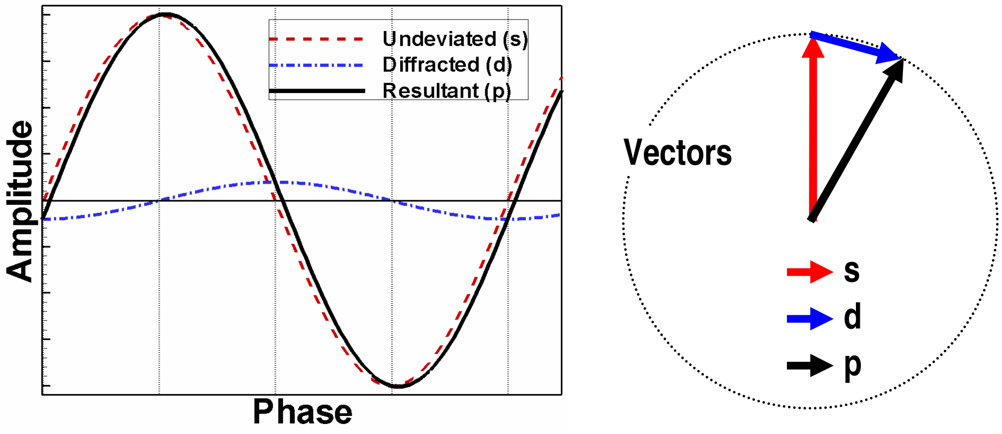

(a) Bright Field Microscopy (BFM)

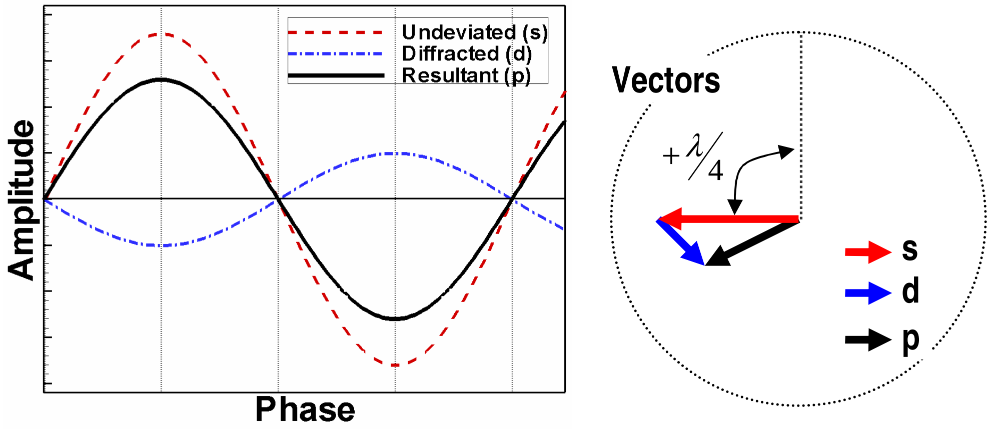

(b) Phase Contrast Microscopy (PCM)

Figure 1.17: Phase relationships between the surround (s), diffracted (d), and particle (d) waves.

with an amplitude that is nearly equal to that of the surround (s) wave. Therefore because the undeviated (s) and resultant (p) waves have similar amplitude, there is no generation of contrast and there can be no clear representation of the specimen.

The phase changes in PCM are shown in the figure 1.17 (b) and figure 1.18, where the spherical wavefront of diffracted light emerging from specimens is retarded by $\lambda/4$ relative to the phase of the planar surround (undiffracted, s) wave. The surround (s) wave is then advanced in phase by another $\lambda/4$ when it traverses the phase plate[16] in the objective. The net phase shift in PCM is therefore $\lambda/2$ such that the advance undeviated (s) wave is able to participate in maximum destructive interference with the diffracted (d) waves at the intermediate image plane, resulting in the resultant (p) wave. The amplitude of the resultant (p) and advanced undeviated (s) waves are considerably different in the intermediate image plane so that the specimens are shown to be contrast-enhancing images in the CCD or through the eyepieces. The images, shown in the figure 1.18, present two adjoining endothelial cells with the use of phase contrast microscopy.

1.6 Differential Interference Contrast Microscopy (DICM)

The differential interference contrast microscopy (DICM) also transforms the phase shift of light, induced by the combination of refractive index and thickness of specimens, into detectable amplitude differences but it does not have halo artifact shown in PCM. Incident light initially passes through a plane polarizer and then is split into two perpendicular yet in phase components (ordinary wave and extraordinary wave) using a

---

[16] The light passing through the phase ring in the phase plate is advanced by $\lambda/4$ compared to the light that does not pass the phase ring.

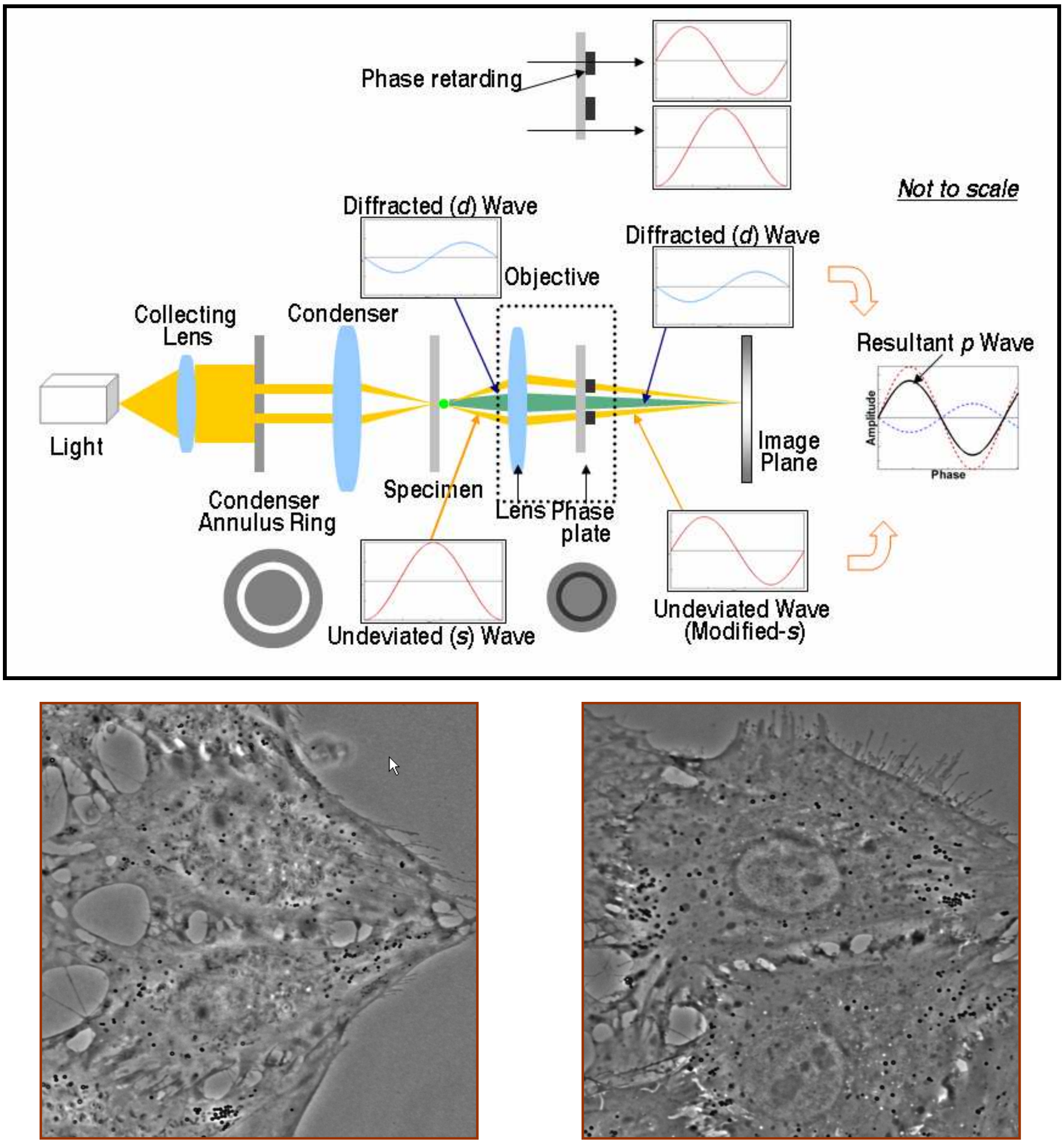

Figure 1.18: Schematic of phase contrast microscopy (PCM) illustrating amplitude versus phase after passing through specimens (d- and s-waves), after passing the phase plate in the objective (d- and advanced (modified) s-waves), and at the image plane where there is considerable amplitude difference between p-waves and advanced s-waves. All the graphs have amplitude (y-aixs) versus phase (x-axis). The images are obtained by using this technique.

condenser Nomarski prism. The two perpendicular rays are then focused by the condenser so that they will pass through two adjacent points in the sample. The spatial difference between two rays is minimal[17]. In any part of the specimen in which adjacent regions differ in refractive index, the two rays are delayed or refracted differently. The phase shifted and sheared rays are combined through differential interference by the objective Nomarski prism[18] and an analyzer yields a high-contrast rendition of the gradient (Figure 1.19). The DICM images[19] shown the figure 1.19 corresponds to the mathematical first derivative, rather than magnitude, of the gradient profile obtained from the specimen optical path difference. A wide variety of specimens can be visualized with differential interference contrast microscopy (DICM), including very thin filaments, thick specimens, and sharp interfaces.

It is cheaper to set up phase contrast microscopy (PCM) mainly needing a phase annulus ring and a objective lens than differential interference contrast microscopy (DICM) consisting of a polarizer, a condense prism, a Nomarski prism, and a analyzer. One more thing to consider for a DICM image is that perfect images are captured through all the materials along the light path should not be birefringent or plastic. However there are advantages of DICM images over PCM images as follows: (1) no halos, (2) realistic 3-dimensional shape, and (3) optical sectioning under the high magnification.

---

[17] It is acceptably known to be less than the maximum resolution of the objective.

[18] The Nomarski objective prism overlays the two bright field images and aligns their polarizations so that they can interfere. Instead of interfering with a ray of light that passed through the same point in the specimen, it will interfere with a ray of light that went through an adjacent point and have a slightly different phase.

[19] Because the difference in phase is due to the difference in optical path length, the recombination of two rays causes “optical differentiation” of the optical path difference, generating contrast-enhancing images.

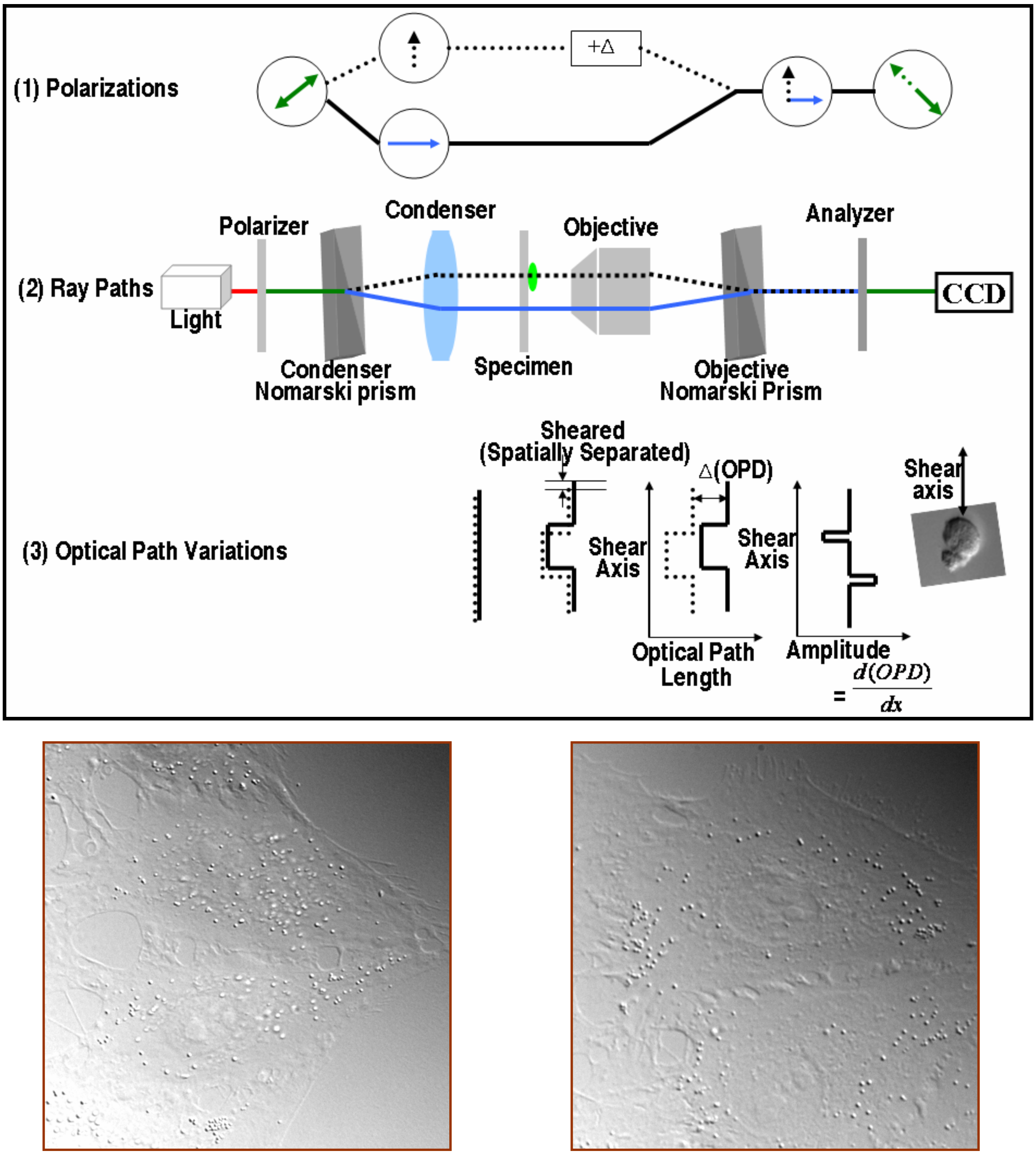

Figure 1.19: Schematic of principle of differential interference contrast microscopy (DICM) using dual-beam interferometers created by polarization optics. Polarizations, optical path variations, and ray paths are explained at the corresponding stages. Note that amplitude only varies when there exists differential interference. The images are taken by DICM and show adjoining two endothelial cells.

1.7 Interference Reflection Contrast Microscopy (IRCM)

Rainbow color fringe patterns are easily seen everywhere a thin film is present. This includes an oil film on water, an air or water film between coverslips, and soup bubbles in the air. The figure 1.20 shows two examples as follows: First, lines were drawn on the coverglass by using a black color-pen and second, thin water film between glasses. They produce color fringe patterns shown in the figure that can be captured using our advanced multi-spectrum interference reflection microscopy.

Basically there are three methods of color imaging using CCD arrays as follows: (1) In the Mosaic technology used in a DP70 digital color camera, it uses Bayer filter mosaic. Each block consisting of four pixels contains 2 green filters, 1 blue filter, and 1 red filter. The raw output of Bayer-filter camera is referred to as a Bayer pattern image. Since each pixel is filtered to record only one of the three colors, two-third of the color data is missing from each. A demosaicing algorithm is used to interpolate a set of completed red, blue, and green values for each point to make a RGB images. There exist many different algorithms. A Bayer pattern image is processed with a correlation-adjusted version of linear interpolation algorithm and is then reconstructed by interpolation. The reconstructed image looks good in low contrast area. However the edges of letters have visible colored artifacts and a rough appearance. This filtering scheme allows us to capture color images, but since four pixels must be combined to form one color dot, the resolution of the image is less than a monochromatic image. (2) In order to use a CCD with multi-color filters, tunable RGB filters can be accommodated with monochrome CCD camera to obtain a high-resolution color images. There are several ways to have a

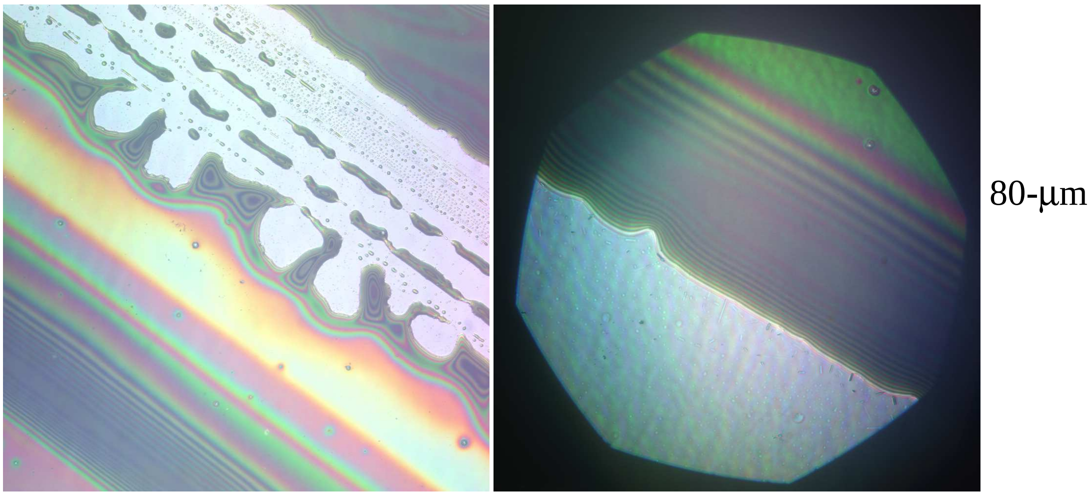

Figure 1.20: Two examples; (1) lines were drawn on the coverglass by using a black color-pen and (2) thin water film between glasses. They produce color fringe patterns shown in the figure that can be captured using our advanced multi-spectrum interference reflection microscopy.

set of filters such as the liquid crystal technology or mechanical shutter system to switch rapidly between the red, green, and blue color states. Each color state is carefully designed to transmit, as closely as possible, and wavelength ranges that match the individual color sensitivity curves of the human eye. The red, green, and blue color states can be selected by computer control in any order, and the exposure time for each color can be varied to provide an accurate white balance. Three grayscale images are acquired in quick succession as the filter automatically changes color states. The images are combined to obtain true 24-, 36-, or 48-bit color images. No interpolation routines are needed for getting accurate color, pixel-by-pixel, and the image possesses maximum sharpness. (3) In the color 3-CCD Camera, three CCD color camera were developed to eliminate many of the problems associated with a single array color camera. An optical prism assembly is used to separate an image into three color components. Each spectral image is captured with a CCD. Using this technique, virtually all of the light for a color channel arrives at the CCD array. Each color channel CCD utilizes all of its pixels so the channels are captured and can obtain the full array resolution rather than the reduced resolution of the single chip color camera. The 3-CCD camera has three times the number of pixels as a single array camera so the image resolution is improved. Neat filters mounted in front of each array accurately control the spectral band so the camera can provide very accurate color representation.

In our system, the second one using one monochromatic CCD with filter wheel system having blue, green, and red channels is accepted to be our system in order to take multi-spectrum interference reflection microscopic (MS-IRM) images. Simultaneously using monochromatic- and color IRM measurements, the detailed characterization of cell-matrix gap topology and focal adhesion points will be possible in unprecedented details and spatial resolutions. The natural fringes occur from the interference of reflections from two surfaces, one from the cellular bottom membrane and the other from the glass substrate. The resulting fringe patterns represent the quantitative gap topology possibly in nanoscale resolutions. The monochromatic IRM images allow measurement resolution of $\lambda/4$ ~ 100 nm, for the case of a green filter, but provide no information on the slope characteristics. In comparison (figure 1.21), the MS- IRM provides substantially finer measurement resolutions because of its multiplicity in fringe spectra. In addition, the order of color fringes determines the slope of the separation distance topology, i.e., the spectrum orders in R-B-G-R for a positive slop and R-G-B-R for a negative slope.

Thus, historically interference reflection microscopy producing monochromatic fringe patterns have been used to examine cell-to-substrate contacts [70-90]. This gap information from IRM images tells cell-substrate adhesion (figure 1.22), such as focal contacts shown darker streaks which is the closest distance, close contacts shown to be dark area which are a little bit more distant than focal contacts, and large cell-to-substrate distance shown bright, which are other area than focal contacts and close contacts. IRM images are obtained by interference of reflected lights from the interface at the glass-medium and medium-bottom membrane. Reflection from the top membrane produces a signal that is too weak to capture.

The developed advanced multi-spectrum interference reflection microscopy (MS-IRM) having better resolutions and uphill/downhill information of the bottom morphology of cells is mainly used to examine cell-to-substrate contacts and to estimate gap morphology between a cell and substrate.

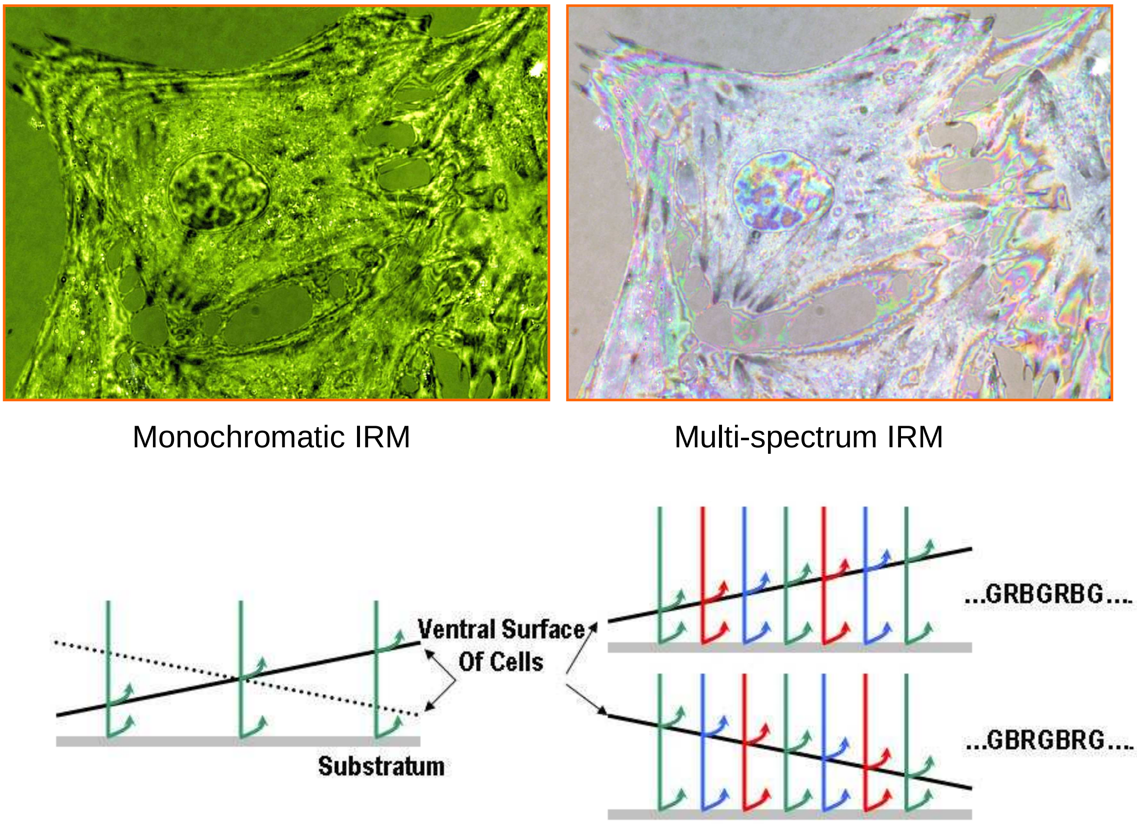

(a) Mono-IRM (Green)

(b) Color-IRM

Figure 1.21: Mono-/color- interference reflection microscopic images (86 μm x 60 μm) and the corresponding schematics telling uphill/downhill of bottom morphology.

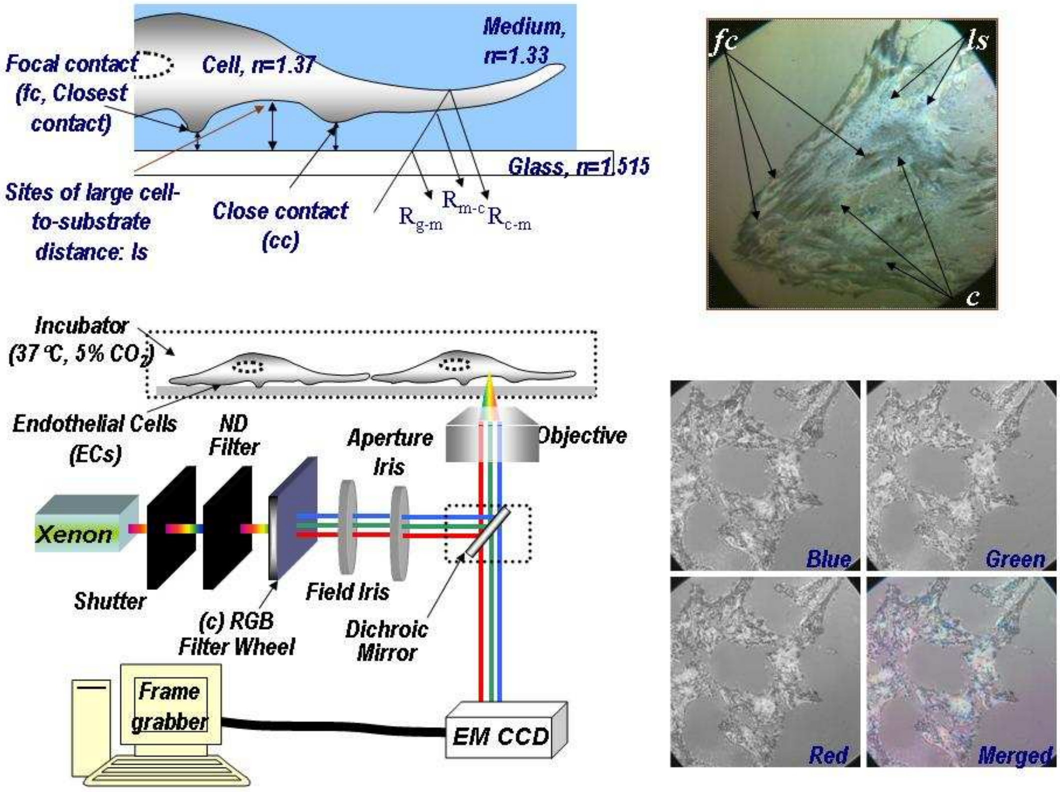

Figure 1.22: Experimental setup for multi-spectrum interference reflection microscopy (MS-IRM) on the bottom left corner, schematic of cell-substrate adhesion and its corresponding MS-IRM images, and IRM images from each channel and merged channels.

CHAPTER 2

ELECTRICAL SENSING

2.1 Introduction

The study of cells had not been made possible until the invention of the light microscope. There are, however, a lot of limitations in using them to examine cellular physiology including morphology changes, cellular division, and cellular micromotion due to the fact that mammalian cells are tiny, translucent, and colorless. Techniques for understanding the finer structure of cells weren't developed until the latter part of the19th century, when staining methods that can provide sufficient contrast became available. The study of cellular functions and responses has been done for decades to better understand the workings of the cell body as well as its structure. As technology has advanced, the capabilities and sensitivity of cellular studies has greatly improved. A more recent technology has been developed to study electrical properties of cells by stimulating them with an electrical signal and analyzing its response. This unique technique of measuring the cellular electrical response has created a new way of dynamically examining cells.

Much of the intricate and complex behavior of organisms can be attributed to the electrical activity of the cell. Various processes like sensory perception, cardiac function, muscle control, thought, etc. are all partially controlled and regulated by the electrical activity and response of different cells in the body. Structurally, cells are composed of a lipid bilayer membrane enclosing an intracellular ionic solution. This membrane contains numerous proteins, receptors, ionic channels, and ionic pumps which are responsible for maintaining the ionic concentrations within the cell and the intracellular potential relative to the extracellular potential [91].

The major advances in electrophysiology, which had been first established in nerve tissue by L. Galvani, began in 1934, when Alan Hodgkin began his research into the physiology of nervous tissue. Despite the many advances in the study of cellular electro-physiology, there were still many questions unresolved such as (1) what controlled ion flow through the membrane, (2) were the pore-like openings in the membrane, and (3) did transporter molecules exist.

Throughout the last decade, elaborate experimental methods to isolate and culture mammalian cells in vitro have been developed and constantly improved so that cell cultures for almost any tissue of living creatures may be obtained. This has been largely motivated by the desire to study particular cell types apart from the complexity of an entire organism in well defined laboratory conditions. However, for maximum scientific information it is not sufficient to have the cell cultures available, it is also important to develop sensitive laboratory techniques to either monitor the behavior of living cells non-invasively by using sensors or to manipulate them using actuators.

With the advent of micro fabrication technologies, which have allowed us to develop microelectrode arrays, dynamic measurements of electrical properties of the cells have become a common method for inference of various cellular processes [91]. Of all the methods involving the analysis of electrical signals from these biological specimens, the electrical impedance measurement technique is the most widely used to monitor cellular activities.

The Electric Cell-substrate Impedance Sensing (ECIS) system is a novel biosensor designed for real time monitoring of cell behavior including attachment, motility and cytotoxicity in a continuous fashion. It was developed by Drs. Ivar Giaever and Charles R. Keese [92-94] in 1984 and commercialized in the early 90`s. The novelty in the ECIS setup was stimulating the cell by a weak electric signal and analyzing its response which was completely different from the traditional method of recording and analyzing the inherent electrical property of the cell. This method thus provided a new dimension in cell research which allowed the continuous tracking of cellular adhesion, growth and micromotion and even the cellular response to toxic substances and pharmacological agents [94-97].

Besides gold electrodes, which are commercially available, there are several types of electrodes to electrically measure cellular physiological properties as long as the materials of electrodes are conductive and bio-compatible. The biosensor subjects cells growing on gold microelectrodes to small ac electric current. Since the cells behave essentially like insulating particles, a very weak and non-invasive current (< 1 µA), is used to perform the measurement. As long as cells started attaching and spreading, this current must flow around the cell which refers the increases in the calculated electrical resistance. An interesting feature from the impedance results is the fluctuation in the calculated impedance, which is always associated with living cells and persists regardless sub-confluence and/or confluence cell inoculations. This behavior is attributed to micro-motion, the tightness changes in cellular adhesions such as cell-cell adhesion and cell-ECM (extracellular matrix) adhesion, the number of packed cells on the working electrode, and the morphology change in viable cells. The resistance read out is complicatedly dependent on electrode coverage, cellular adhesion tightness, the cellular shape, cytoplasm conditions, the number of cells, and the case of confluent or sub-confluent cell layers. Since the electrodes are very close to the cell bodies, this electrical measurement is very sensitive and capable of resolving changes in cell shape much smaller than the resolution of an optical microscope.

2.2 Experimental Setup

The Instrumentation of the biosensor is based on ECIS technology, which measures the voltage drop across the working electrode to the counter electrode. The cardinal part of the instrumentation is the specially engineered slide which has a series of wells suitable for cell culture and an array of gold electrodes that forms the base of the slide which bridges the electronics of the biosensor setup to the individual wells. It should be noted that electrodes can be made of any bio-compatible and conductive materials, such as gold used for many commercial electrodes and Indium Tin Oxide (ITO) which is proposed and developed in this experiment.

The cells are deposited on the electrodes which may be pretreated with an adherence promoting protein called fibronectin. However this general surface treatment on the electrode surface is not carried out since the factor of surface material is another important observation to examine the cell growth rate. These cells form a monolayer over the electrodes as they settle down. A small non invasive current of about 1 μA is passed through the gold electrodes, which results in a voltage across the electrodes oscillating at the same frequency as the applied current.

The working principle of the electrical biosensor setup is that the change in the morphological characteristics of the cell can be detected as a change in the measured impedance. The measured voltage drop reflects the adhesion of the cells to the electrode surface. The barrier function associated with the endothelial monolayer restricts the current flow and a marked increase in the resistance is observed during the time during which the cells reach confluence over the electrode. The impedance difference between naked scans, where there is no cellular attachment, and attached scans, where there are cellular attachments and spreading involved, can be seen by normalizing the data. After the cells reach confluence over the electrode, the steep change in the measured data is reduced to small fluctuations that can be measured over time. These fluctuations can be attributed to the micro-motion of the cells over the electrode surface. This arrangement thus serves as a basis from which we can subject the cells to various external stimuli and signals and monitor its response.

2.1.1 Lock-in Amplifier

The lock-in amplifier is a device which is used to detect and measure very small AC signals down to the level of a nanovolt. It has the unique ability to accurately measure small signals which may be buried in noise signal thousands of times larger than the original signal of interest. The amplifier uses a technique known as phase-sensitive detection which singles out the signal at a specific reference frequency and phase while filtering out noise, which exist at different frequencies. Even when the output of the instrument reads full scale the input sensitivity of the lock-in amplifier is achieved by adjusting the gain of the signal path. The input circuits are devised in such a way that they can handle signals many times larger than the calibrated value and thus makes a reliable measurement possible. This performance feature is called "dynamic reserve" and is a measure of the ability of a lock-in amplifier to recover signals that are buried in noise**.**

In this paper, the Lock-in amplifier was used to provide a non-invasive current of

1 μA through the electrodes by applying an ac voltage of 1V through a series resistance of 1MΩ so as to excite the cells in the electrode wells. The Lock-in amplifier is also used for the phase-sensitive detection of the resulting voltage across the electrodes using the principle previously discussed. The data was acquired for a wide range of frequencies ranging from 10 Hz to 10^5 Hz. The lock-in voltage source impedance, Z_s, was measured to be approximately 50Ω and the input impedance, Z_v, of the phase sensitive etector had resistive, R_v, and capacitive, C_v, components of 10 MΩ and 25 pF, respectively. To evaluate R_b and C_m model parameters, which characterize the endothelial cell barrier function, it was necessary to convert the voltage measurements into corresponding impedance values. The measured voltage conversion to the corresponding impedance are done considering all the resistance and capacitance of sources and all the cable in order to reduce systematic errors.

2.1.2 DAQ

The Data Acquisition System (DAQ) for this investigation is devised using the National Instruments Signal Conditioning eXtensions for Instrumentation (SCXI) DAQ package. The system consists of a chassis which acts as the base of the acquisition setup, the module which acts as the signal conditioning circuit, the terminal block which act as connectors for I/O signals to the system and a plug-in DAQ device. The plug-in DAQ device can be replaced with a module which has an inbuilt DAQ card. The chassis, which is highly rugged and made of aluminum, contains an analog bus, a digital bus, and a chassis controller regulating bus operations. The analog bus transfers all the analog signals at the input modules to the DAQ device while the digital bus is controlled by the DAQ device for chassis operation. The modules are the heart of the DAQ system as they perform the important function of signal conditioning. The module acts as a multiplexer, amplifier, and filter, and can also isolate voltage and current signals. There are different types of modules available and the choice depends on the application. The terminal block consists of attachments to the front of the module and act as a convenient interface for connecting I/O signals to the system. There are two types of terminal blocks, the direct-mount block and the terminal block extensions. The former, as the name suggests are directly connected to the module using connector screws while the latter is connected to the module using shielded cables. The DAQ system for this investigation has used the SCXI-1140 module housed in a SCXI 1000 chassis. The terminal block used is a SCXI-1331 which connects the input from the lock-in amplifier to the module, which switches the signal between the five electrode arrays to excite the cells. The response is then detected by the lock-in amplifier and passed on to the terminal block which routes it through the module to the DAQ board on the computer. The data acquisition software collects the data from the DAQ board and stores it for further analysis.

2.1.3 Electrical Circuit

A data acquisition and analysis system was implemented using LabVIEW. Figure 2.1 shows a schematic illustration of the impedance measuring circuit configuration. A reference voltage source provided an ac $1v_{p-p}$ reference signal via a series 1 MΩ resistor, R_{cc}, to the electrode array. A National Instruments SCXI-1331 switch made successive connections between the different working electrodes and the counter electrode of each array. The source voltage generator resistance, R_s, was 50 Ω.

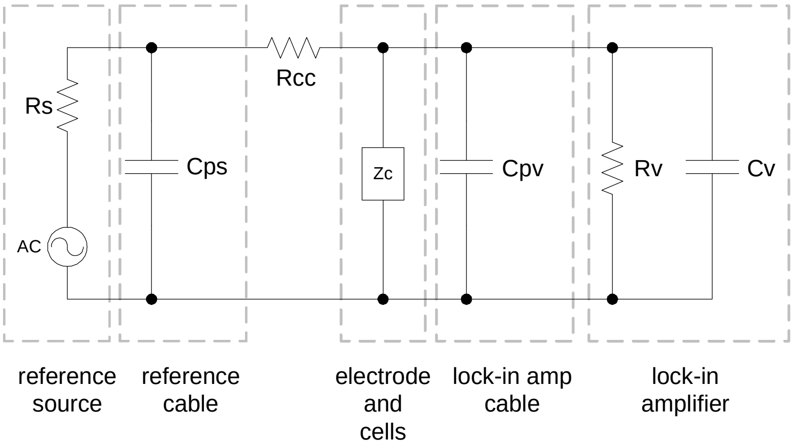

Figure 2.1: Electrical impedance measuring circuit. The electrode array was connected to a lock-in amplifier voltage source through a 1MΩ series resistor to provide an approximately constant 1μA current source. The measured voltage was used to estimate the impedance.

Since the series resistance was significantly larger the electrode impedance over the range of frequencies used in this study, an approximately 1 μA constant current was provided to the electrode. An SR830 lock-in amplifier measured the electrode voltage. The input impedance of the lock-in amplifier was equivalent to a parallel resistor, R_v, and capacitor C_v combination of 10 MΩ and 10 pF, respectively. The source and lock-in amplifier cable have parasitic capacitance, C_{ps} and C_{pv}, respectively. Direct measurements of the cable parasitic capacitances were made using an LCR meter and incorporated into the circuit model to estimate the impedance based on the lock-in voltage measurement.

2.3 Impedance Measurement

Impedance is the frequency-dependent opposition of a conductor to the flow of an alternating electric current. A measure of impedance (Z) is composed of the sum of two vectors, resistance (R) and reactance (Xc), measured at a particular frequency and is described mathematically by the equation $Z^2 = R^2 + Xc^2$.

Resistance is the opposition of a conductor to the alternating current, and as the electric current travels through the body, resistance is basically the same as in non-biological conductors. Reactance is produced by the additional opposition to the current from the capacitant (storage) effects of cell membranes, tissue interfaces, and structural features. Early studies of bioelectrical impedance focused on the meaning of impedance measures in relation to the water and electrolyte content of the body, and to physiological variables such as thyroid function, basal metabolic rate, estrogenic activity, and blood flow in human and animal tissues. These explorations developed into some of the present-day areas of impedance cardiography, pulmonary impedance, brain impedance, and impedance imaging. The use of bioelectrical impedance to estimate body composition developed from more recent exploratory works in the areas of single-frequency and multiple-frequency impedance. An alternating current is used for bioelectrical impedance analysis because it penetrates the body at low levels of voltage and amperage. In a complex electrical structure such as the human body, the part of the fluid volume measured by bioelectrical impedance is also a function of the current frequency. At low frequencies of less than about 5 kHz, the bioelectrical current travels primarily through extracellular fluids, but as the frequency increases, the current starts to penetrate body tissues, creating reactance. At high frequencies (above 100 kHz), the current is assumed to penetrate all conductive body tissues or all of the total body water in the conductor and supposedly overcomes the capacitant properties of the body, reducing reactance to zero. One of the earliest devices was manufactured by Hanna and Johnson (1968) who produced an array of 20 or 30 electrodes on a plastic sheet using photo etching techniques. Their device however was intended for surface potential recording due to the size of the electrodes. Although designed for recording from cardiac cells, one of the original microelectrode devices manufactured was by Thomas *et al.*[98]. The basic fabrication principles of this method are still used in more modern designs. This microelectrode array was etched into thin metal films deposited on glass cover slips. Thin-film nickel layers were vacuum deposited onto a glass coverslip and were insulated with a thin layer of insulating polymer. The coverslip was then exposed to light through a photographic negative image of the desired electrode pattern. The polymer was removed and the metal remaining uncovered was removed with acid. The nickel was then gold-plated, re-insulated, and the electrodes exposed by repeated light exposure with a second negative image of the desired pattern. Electrode impedance was improved by coating the electrode tips with platinum black. Their system contained 30 microelectrodes arranged in two rows 50 mm apart; the distance between electrodes in rows was 100 mm. Using this system Thomas and colleagues (1972) were able to record potentials from cultured chick cardiac cells. Successful implementation of the microelectrode system by Thomas et al. inspired many investigators to extend its use to monitor the electrical activity of many organisms like bacteria, algae [99], neurons [100] and also various organs in the body. With the rapid development of fabrication techniques and advent of visualization methods, monitoring the health of cells and tissues and following their dynamics has provided a plethora of information, thus solving many mysteries which have puzzled investigators over the years. Yet, it is predicted that there is a long way to go before we can completely understand the complexity of cellular function and activity.

2.3.1 Resistance

Figure 2.2 show the normalized resistance as a function of time and dose of Tolfenamic Acid (TA) from 0 to 30 μM to examine apoptotic morphology changes in HCT116 cancer cells. The cell concentration used here was 2x 10^5/ml. Representative time-dependent normalized resistances and reactances are selected to be scanned at 5.62 kHz where there is the maximum value among 17 frequencies at each time step. For the sake of clarity, symbols are marked at every 20th data point. The higher concentrations of tolfenamic acid produce a reduction in the normalized impedance components that reflect increasing numbers of apoptotic cells. Apoptotic cellular morphology changes are associated with cell shrinkage, cell rounding, and disintegration of cell-cell and cell-substrate contacts. These change creates a decrease in the normalized impedances.

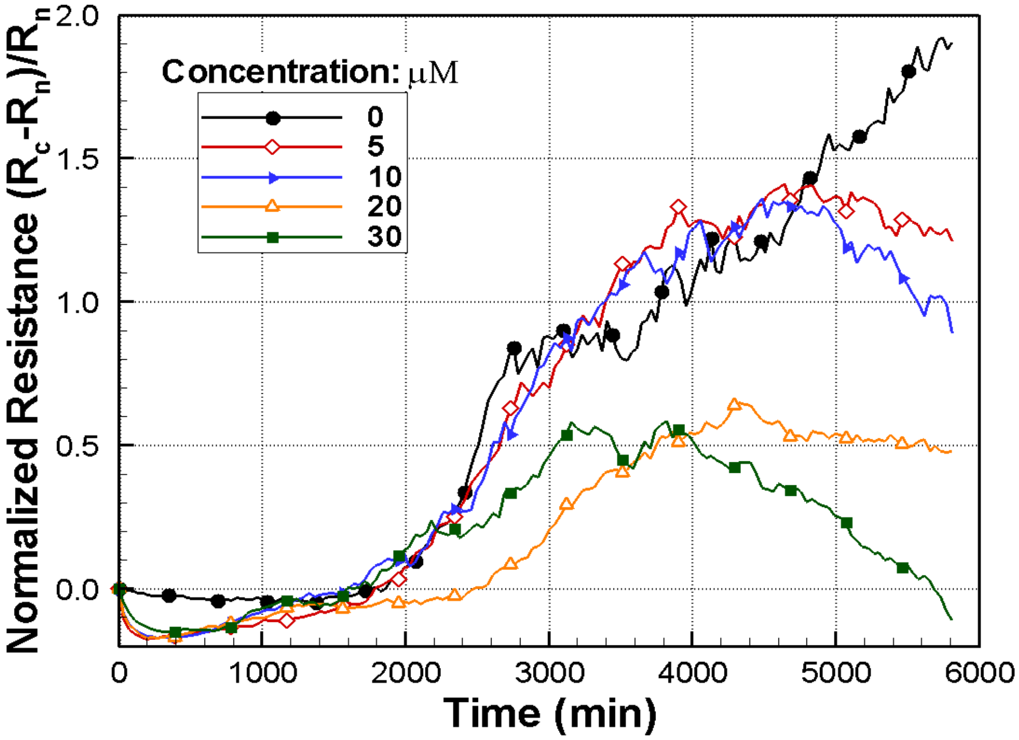

Figure 2.2: Normalized resistance, $(R_c - R_n)/R_n$. The terms R and X represent the resistance and reactance, respectively and the subscripts c and n indicate cell covered and naked scans, respectively.

2.3.2 Reactance

Measurements were performed simultaneously using the same batch of HCT116 cells. The cell concentration used here was 2 x10^5/ml. Representative time-dependent normalized reactances shown in the figure 2.3 are selected to be scanned at 5.62 kHz where there is the maximum value among 17 frequencies at each time step. For the sake of clarity, symbols are marked at every 20th data point.

The well-known existing methods to examine apoptosis are fluorescence microscopy, flow cytometry, and other biochemical assay using agarose gel electrophoresis or enzyme-linked immunosorbent assay (ELISA). While they are all stationary and need fluorescent or radioactive probes, the micro-impedance measurement is a new bio-analytical technique capable of non-invasively and dynamically monitoring apoptosis-induced changes in the 3-dimensional cellular shapes in real time without any probes. Both resistance and reactance at 0 μM keep increasing because of the increase of cell-cell and cell-substrate adhesion, while all other normalized resistances and reactances decreased after they reached their maximum during the 97 hour measurement.

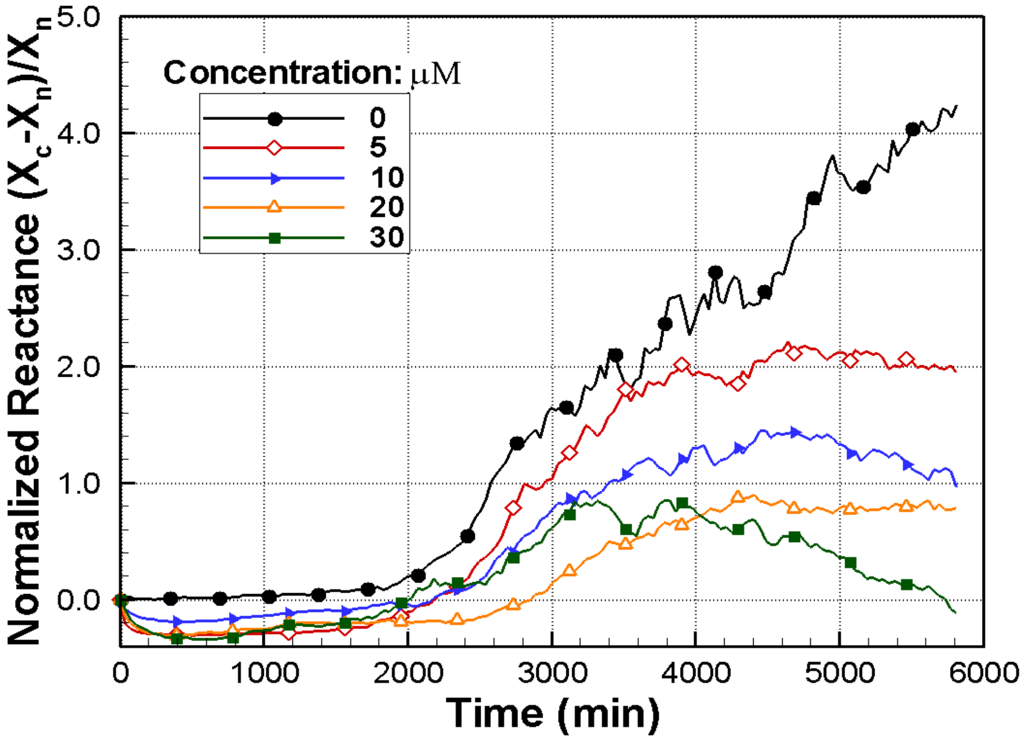

Figure 2.3: Normalized resistance, $(X_c - X_n)/X_n$. The terms X represent the resistance and reactance, respectively and the subscripts c and n indicate cell covered and naked scans, respectively.

CHAPTER 3

INTEGRATED DYNAMIC LIVE-CELL OPTO-ELECTRIC SYSTEM

3.1 Experimental Setup

The dynamic cellular imaging system (figure 3.1) makes it possible to comprehensively examine the spreading, attachment, and confluence characteristics of live cells under environmental challenges in a way that has not been previously prevalent. The system integrates a number of existing as well as newly implemented imaging techniques: bright field microscopy (BFM), epi-fluorescent microscopy (EFM), phase contrast microscopy (PCM), differential interference contrast microscopy (DICM), interference reflection microscopy (IRM), and total internal reflection fluorescent microscopy (TIRFM). The integrated imaging system can provide visible and quantitative knowledge of both interfacial response of cells under multiple stimuli and cellular interaction with bio-vesicles.

3.2 ITO Biosensor

Cellular micro-impedance measurements have found extensive application in quantifying cellular adhesion and barrier function. A relatively recent method, referred to as Electrical Cell-Substrate Impedance Sensing (ECIS) pioneered by Giaver and Keese [92-94], has become increasingly used to study and quantify cellular physiology [29, 97, 101-111]. This biosensor is based on a gold two-electrode configuration that consists of a small working electrode and a larger counter electrode. Although this electrode configuration has the potential to probe cellular barrier function in terms of cell-cell adhesion, cell-matrix adhesion and cellular membrane properties, the optical properties of

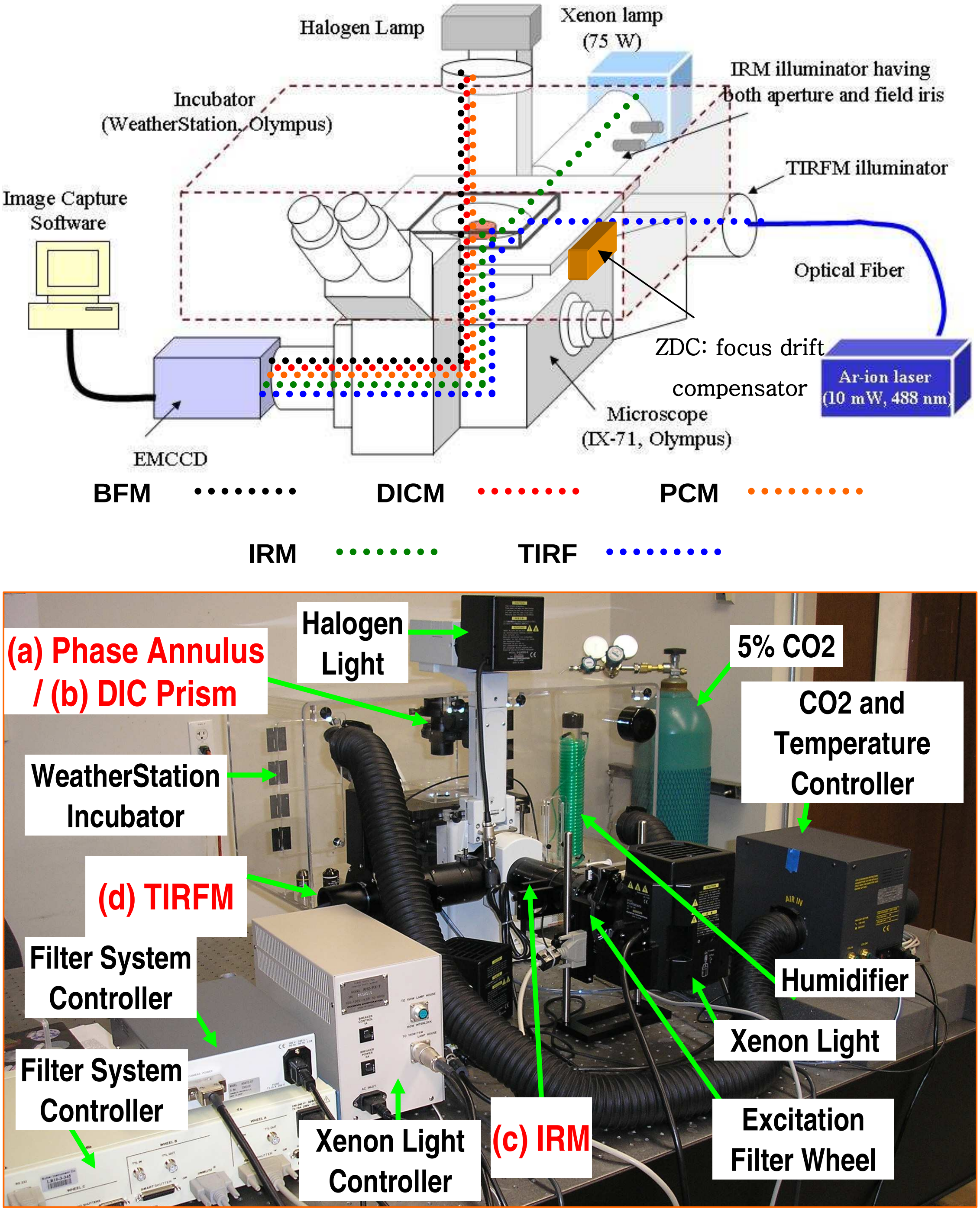

Figure 3.1: Integrated and dynamic live-cell opto-electric system.

gold limit its ability to perform simultaneous electrical impedance and microscopy measurements.

The combined electrical conductivity and optical transparency of indium tin oxide (ITO) makes it an attractive alternative to gold as a microimpedance biosensor [112-120]. Indium-tin-oxide is stable in electrolyte solutions and the transparent properties of this electrode allow the simultaneous optical investigations using phase contrast, interference reflection and fluorescence microscopy. Despite its potential importance in probing cellular barrier function both electrically and microscopically, few studies have examined the fabrication and performance of ITO electrodes for this particular application.

This study describes the fabrication and performance of an ITO biosensor array that is compatible with porcine pulmonary artery endothelial cell growth. The naked and cell covered ITO frequency response is examined using 250 and 500 m diameter electrodes and directly compared to a 250 m diameter industry standard gold electrode with similar array dimensions. This study is motivated by the fact that the ability to combine electrical microimpedance measurements with microscopy methods presents a number of opportunities to study cellular physiology.

3.2.1 Fabrication Process

Figure 3.2 shows a photograph of an assembled array of five transparent ITO electrodes with top and side view schematics. Arrays of five working ITO electrodes were fabricated with either 250 or 500 μm diameter electrodes, respectively. The electric current flowed between a working electrode and the larger counter electrode.

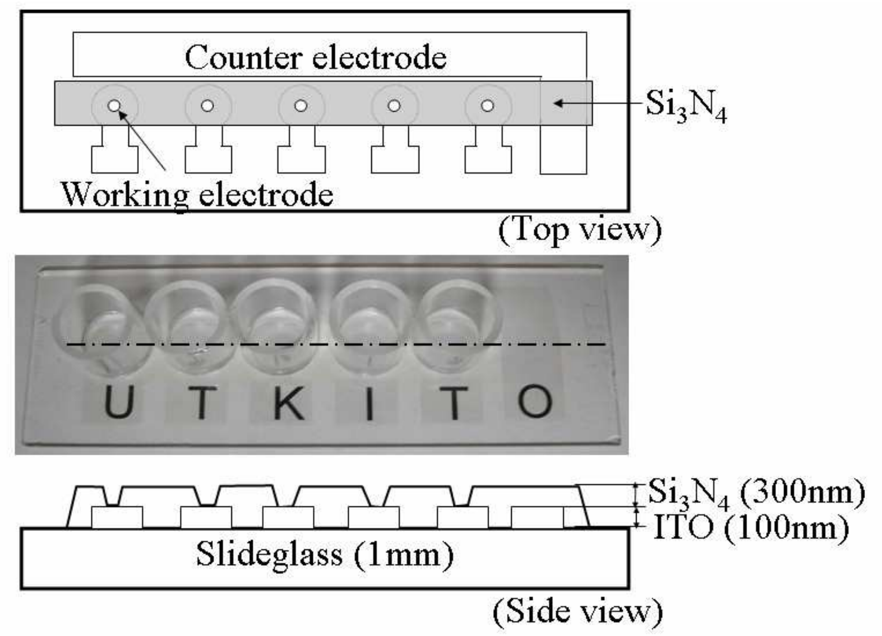

Figure3.2: Indium tin oxide–silicon nitride electrode array. By etching either a 250 or 500 μm diameter hole in the insulating silicon nitride layer an array of five electrodes was formed. Each electrode made an electrical contact with a common 2 cm^2 counter electrode via a 400 μL well. Letters, “UTKITO”, are easily seen through the ITO layer coated on the glass slide demonstrating the high transparency of the material.

Figure 3.3 summarizes the ITO electrode fabrication process. The ITO biosensor array consisted of six 100 nm ITO film electrodes deposited on a 76 mm x 26 mm glass slide using an AJA ATC2000 RF magnetron sputtering system. Five of the electrodes were used as working electrodes while the sixths was a common counter electrode. The sputtering target consisted of 90wt. % In_2O_3 and 10wt. % SnO_2. The base pressure prior to the sputtering deposition was below 5.3 μPa. During sputter deposition, a flow rate of 25 sccm of Ar-H_2 was introduced into the chamber to produce a 3 mTorr pressure. The ITO sputtering power was 200 W and the film was deposited for 15 minutes at a temperature of 400 ^{o}C. Subsequent to the ITO thin film sputtering, photoresist (955CM-2.1) was spin-coated for 50 seconds at 3000 rpm resulting in a nominal 1.5 μm thickness. After spin coating, the photoresist was soft baked at 90 °C for 45 seconds, exposed to a 365 nm wavelength for 1.5seconds using a Karl Suss MA6 contact lithography system, post exposure baked at 120 °C for 45 seconds, and developed in CD-26 developer for 70 seconds. Finally, the ITO was wet etched with Cyantek LCE-11 etchant at 40 °C. Stripper solution then removed the photoresist at 70 °C.

On the top of the patterned ITO electrode, RF magnetron sputtering in argon-hydrogen (5 % H_2) and nitrogen gases deposited an insulating 300nm silicon nitride film. The sputter deposition condition of the Silicon Nitride film was 100 W RF power, 5 mTorr pressure, 25 sccm Ar-H_2, and a 25 sccm N_2 gas flow at a temperature of 300 ^{o}C. A similar photolithography process as described for the ITO film pattern produced the silicon nitride layer. The silicon nitride insulating wells on the array were patterned by reactive ion etching (RIE) with SF6/O2 chemistry.

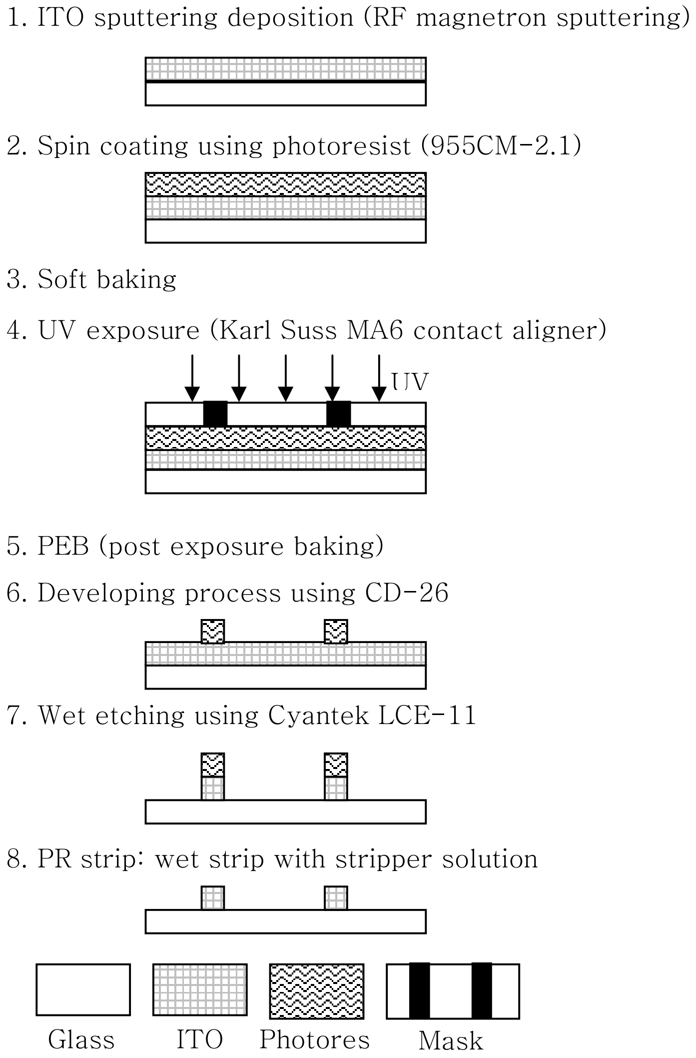

Figure 3.3: Fabrication of ITO thin film microelectrode on slide glass. A 90 % In$_2$O$_3$/10 %SnO$_2$ 100 nm layer was sputter coated onto slide glass. Using standard photolithography methods, an array of five ITO electrodes and a single counter electrode was developed.

The cellular impedance can be detected because the working electrode constrictive impedance dominates the impedance of the whole system. The insulating silicon nitride (Si_3N_4) layer was resistant to ethanol sterilization. Electrodes were therefore sterilized with a 70 % ethanol 30 % de-ionized (DI) water solution and then rinsed with sterilized DI water. All the wells were inspected using microscopy imaging prior to use.

3.2.2 Qualitative optical characteristics

Endothelial cells isolated from porcine pulmonary arteries were cultivated on bare glass, 100 nm thick ITO coated on the coverglass, and 47.5 nm thickness of gold thin film coated on 2.5 nm titanium coated on the coverglass in an incubator at 37 ^{o}C and 5 % CO_2. The cell culture media consisted of M199 (GibcoBRL) and 10 % fetal bovine serum (Hyclone) supplemented with BME vitamins (Sigma), L-glutamine (GibcoBRL), penicillin and streptomycin (GibcoBRL), and BME amino acids (Sigma). The culture was maintained for approximately one week, at which point the cells reached confluence.

Once they reach confluence, endothelial cells grown on three different substrates are taken by using bright-field microscopy (BFM), phase contrast microscopy (PCM), and differential interference contrast microscopy (DICM).

The PCM images (figure 3.4) of PPAECs on a bare glass are comparable to the corresponding images on a 100nm ITO-coated glass, while no discernable cellular image is available for Au/Ti-coated glass under the same illumination intensity.

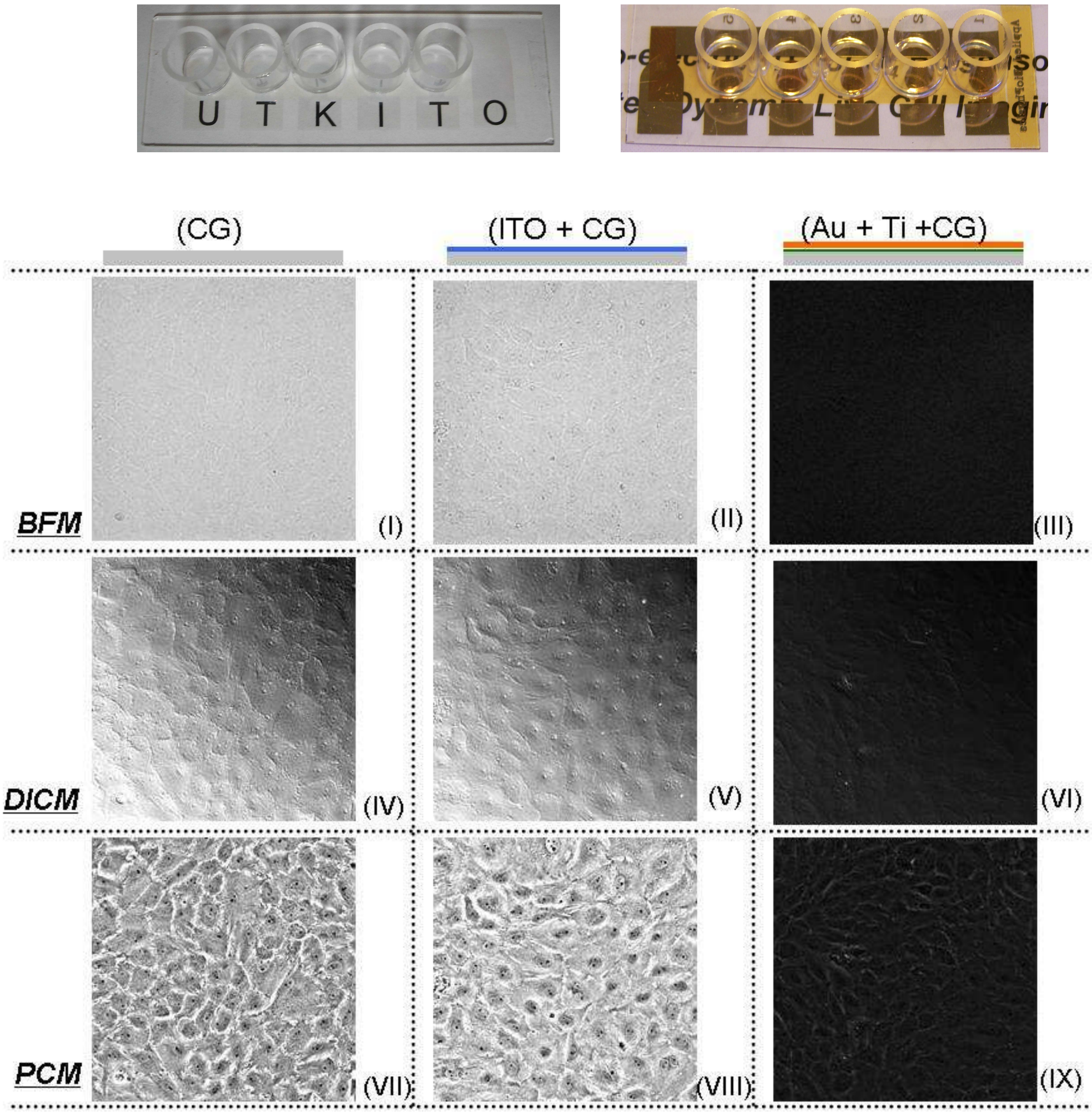

Figure 3.4: Qualitative optical characteristics of ITO thin film using a set of brightfield, phase contrast, and differential interference contrast microscopic images of PPAECs cultivated on a coverglass of 170 μm thickness, a glass surface coated with a 100 nm thick ITO layer, and a glass surface coated with 2.5 nm titanium and 47.5 nm gold layer. Phase contrast cell images of the 100 nm thick ITO film on slide-glass are comparable to those of pure coverglass and far superior to those on the 47.5 nm thick gold film on slide-glass.

3.2.3 Quantitative optical characteristics

Figure 3.5 shows normal transmittance, *calculated* for bare slideglass (*I*) and Au (47.5 nm)/Ti (2.5 nm)-coated slideglass *(II)* and *measured* for bare slideglass (*III*), 100-nm ITO-coated slideglass (*IV*), 500-nm ITO-coated slideglass (*V*), and Au/Ti-coated slideglass (*VI*). The transmittances are measured using a Cary 5000 UV-Vis-NIR spectrophotometer (Version 1.9, Varian) that consists of a double Littrow monochromator, two beam path holders (one for reference and one for sample), PbS/InGaAs detectors, and covers from UV (200 nm) to NIR (800 nm) at intervals of 1 nm and a scanning rate of 10 nm/sec. Measurements are repeated five times at each wavelength, and the extended bars indicate the resulting standard deviations.

In order to validate the experimental data, the transmittance of the multilayer thin film structure is calculated using the characteristic transmission matrix and taking the wave interference effect into consideration. The characteristic transmission matrix of the *m*-th layer is expressed on the basis of *s*-polarized light as follows:

$$M_m(z) = \begin{bmatrix} M_{11} & M_{12} \\ M_{21} & M_{22} \end{bmatrix}_m = \begin{bmatrix} \cos(\frac{2\pi}{\lambda}\tilde{p}_m d_m), & -\frac{i}{\tilde{p}_m}\sin(\frac{2\pi}{\lambda}\tilde{p}_m d_m) \\ -i\tilde{p}_m\sin(\frac{2\pi}{\lambda}\tilde{p}_m d_m), & \cos(\frac{2\pi}{\lambda}\tilde{p}_m d_m) \end{bmatrix}, \tag{3.1}$$

where $\tilde{p}_m = \tilde{n}_m \cos\tilde{\theta}_m$. The complex angle of incidence $\tilde{\theta}_m$ is given from the generalized Snell's law, $\sin\theta_i = \tilde{n}_m \sin\tilde{\theta}_m$, where *i* means incident, and d_m denotes the thickness of the *m*-th layer. The complex refractive index of the *m*-th layer is defined as $\tilde{n}_m = n_m - i\kappa_m$, where both refractive index (*n*) and extinction coefficient(κ) depend on

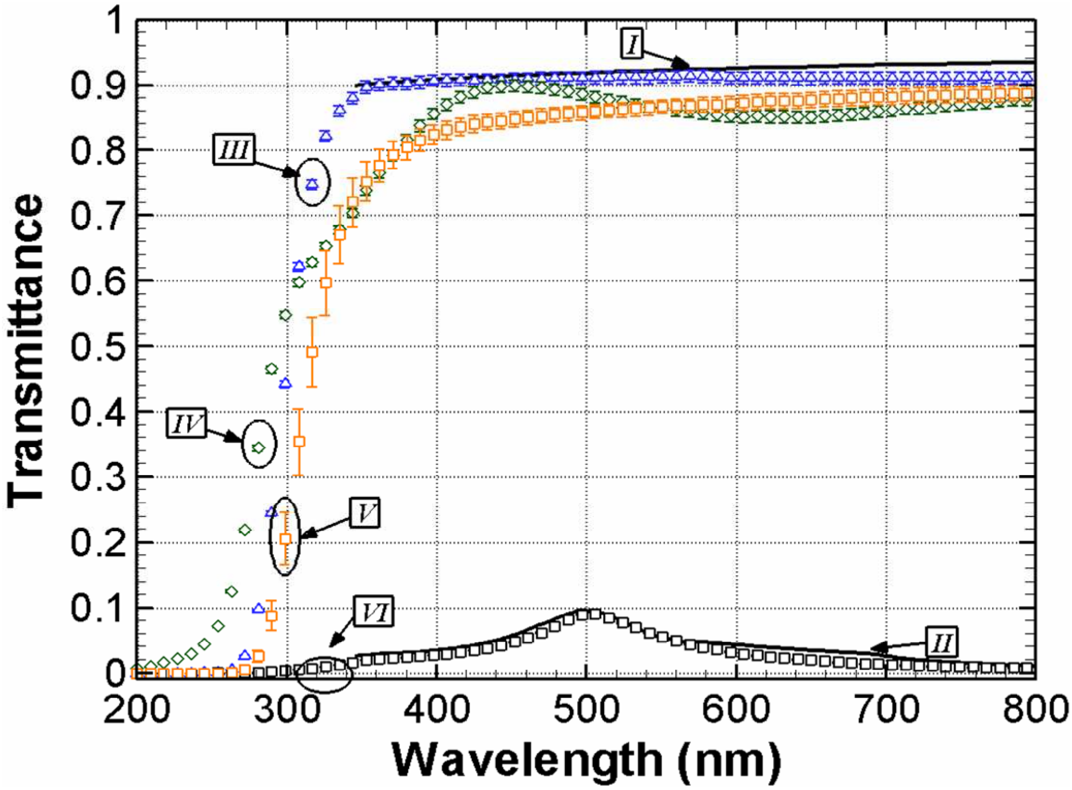

Figure 3.5: Normal transmittance, calculated for bare slideglass (*I*) and Au (47.5 nm)/Ti (2.5 nm)-coated slideglass *(II)*, and measured for bare slideglass (*III*), 100-nm ITO-coated slideglass (*IV*), 500-nm ITO-coated slideglass (*V*), and Au/Ti-coated slideglass (*VI*).

the wavelength (λ).

Assuming all layers are nonmagnetic, the overall transmission matrix *M* is defined by multiplication of the elementary matrix of Eq. (1) for the total *N* layers, i.e., *m* = 1, 2, 3, … , *N* as follows:

$$M = \prod_{m=1}^{N} M_m(z) = \begin{bmatrix} M_{11} & M_{12} \\ M_{21} & M_{22} \end{bmatrix}. \qquad (3.2)$$

Assigning *m = 0* for the incident air medium and *m = N+1* for the transmitting air medium, the overall transmittance (*T*) for multi-layers is given as:

$$T = \frac{\tilde{p}_{N+1}}{\tilde{p}_0} |t|^2, \qquad t = \frac{2\tilde{p}_0}{\left(M_{11} + M_{12}\tilde{p}_{N+1}\right)\tilde{p}_0 + \left(M_{21} + M_{22}\tilde{p}_{N+1}\right)}. \qquad (3.3)$$

The calculated transmittance, Eq. (3.3), is in agreement with the measurements for the cases of bare slideglass (*I*) and gold-coated slideglass (*II*), for the visible range in Fig. 1. The transmittance of the ITO-coated coverglass is not calculated because the complex refractive index of the present ITO thin film is unavailable. At λ = 510 nm (green light), the measured transmittance of 88% for 100-nm thick ITO sputtered layer on slideglass shows a mere 3.2% reduction from the transmittance of 91.2% for bare slideglass, whereas the transmittance is dramatically reduced by more than 90% for the case of the industry standard Au (47.5 nm)/Ti (2.5 nm)-coated coverglass.

3.3 Results

3.3.1 Naked and Cell Covered Gold and ITO Electrode Frequency Dependent Impedance

Figure 3.6 shows the frequency dependent resistance and reactance of a 250 μm diameter gold electrode (A), a 250 μm diameter ITO electrode (B), and a 500 μm diameter ITO electrode (C). Each of the figures compares the measured resistance and reactance between the naked electrode and cell-covered electrode. The measured resistance increases when the electrode is covered with cells, for both the gold and the ITO electrodes demonstrating the feasibility of using the ITO electrode as a bio-impedance sensor.

Figure 3.7 shows the normalized real and imaginary impedance of the same data shown in Figure 3.6. The 250 μm ITO electrode shows similar but somewhat reduced sensitivity to endothelial cell attachment compared to the 250 μm gold electrode. The measurement sensitivity of the cell-covered electrode resistance shows the highest in the range of 1 to 10 kHz with a peak around 5.62 kHz for the gold electrode and 3.62 kHz for the ITO electrode.

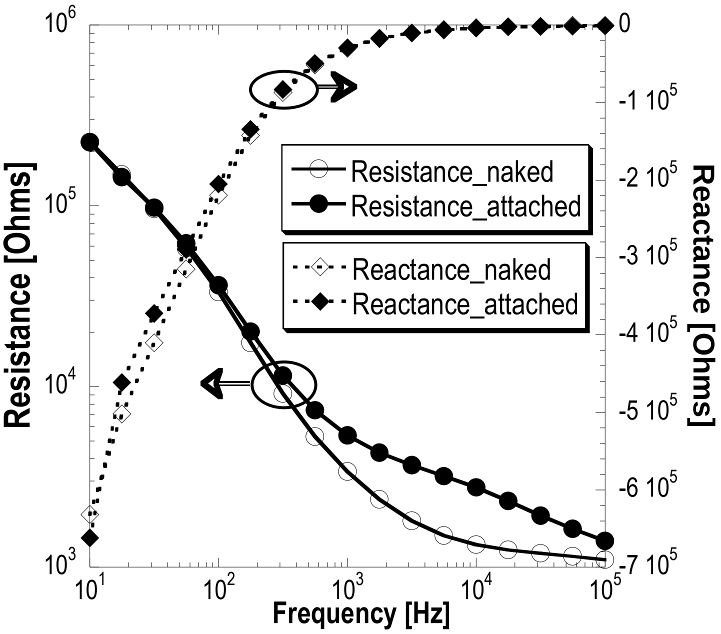

(a) 250 μm gold electrode

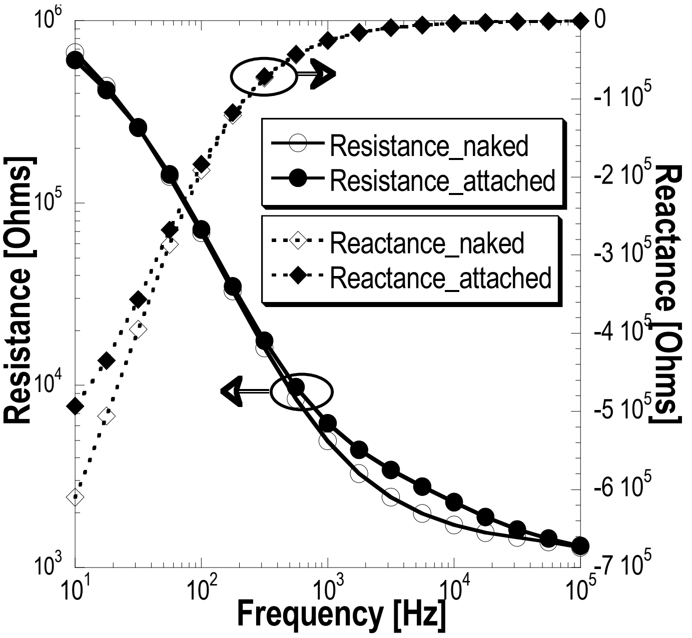

(b) 250 μm ITO electrode

Figure 3.6: Real and imaginary frequency dependent impedance response of naked and cell covered 250 μm gold (A) and 250 μm ITO (B) electrodes. Measurements were performed simultaneously using the same batch of ECs.

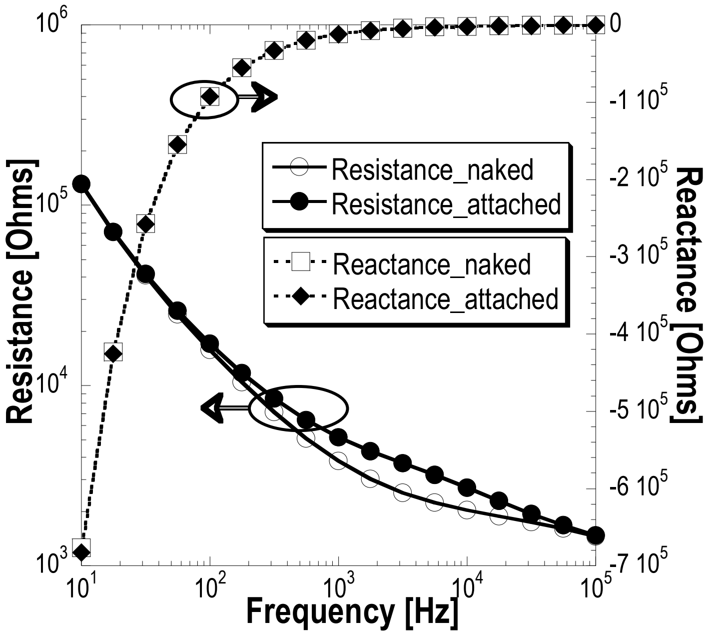

(c) 250 μm ITO electrode

Figure 3.6: Continued. Real and imaginary frequency dependent impedance response of naked and cell covered 500 μm ITO (C) electrodes. Measurements were performed simultaneously using the same batch of ECs.

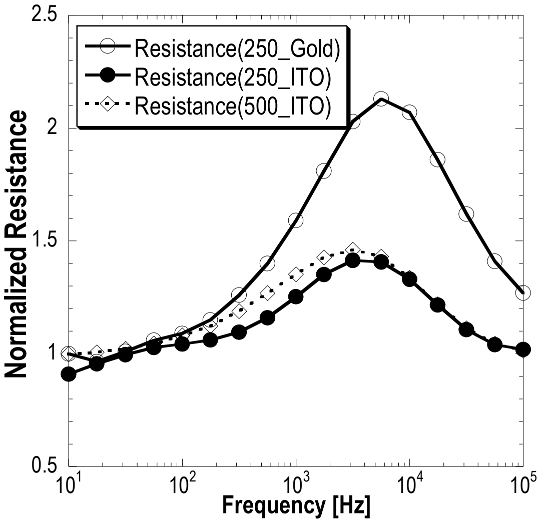

(a) Resistance

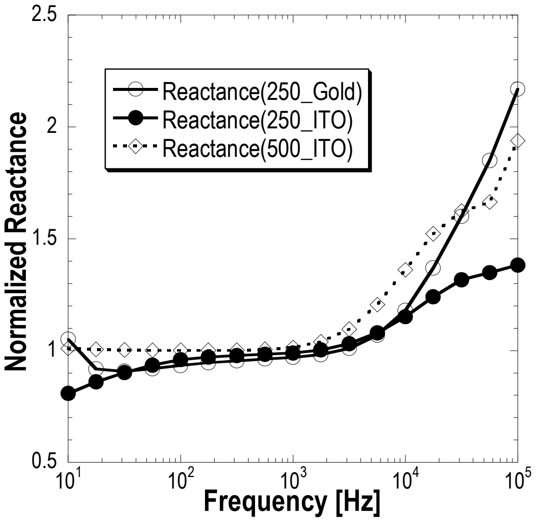

(a) Reactance

Figure 3.7: Frequency dependent normalized resistance (A) and reactance (B) of cell covered 250 μm gold, 250 μm ITO and 500 μm ITO electrodes.

3.3.2 Endothelial Cell Attachment to a 500 μm ITO Electrode

Figure 3.8 shows the frequency dependent changes in electrode impedance as a function of time during the cellular attachment of PPAECs to a 500 μm ITO electrode. An initial peak in the resistance occurred approximately one hour after cell inoculation on the ITO electrodes. The normalized resistance illustrates a peak sensitivity in the frequency range between 500 Hz and 10 kHz. Following the initial peak the normalized resistance stabilizes and slowly decreases over several hours.

Figure 3.9 shows a confluent cellular image on a 500 μm ITO electrode with a 10x objective lens. This confirms cellular attachment with ITO silicon nitride bioelectrodes even without fibronectin as well as demonstrates that the ITO electrode is a good tool for both electrical measurement and optical visualization.

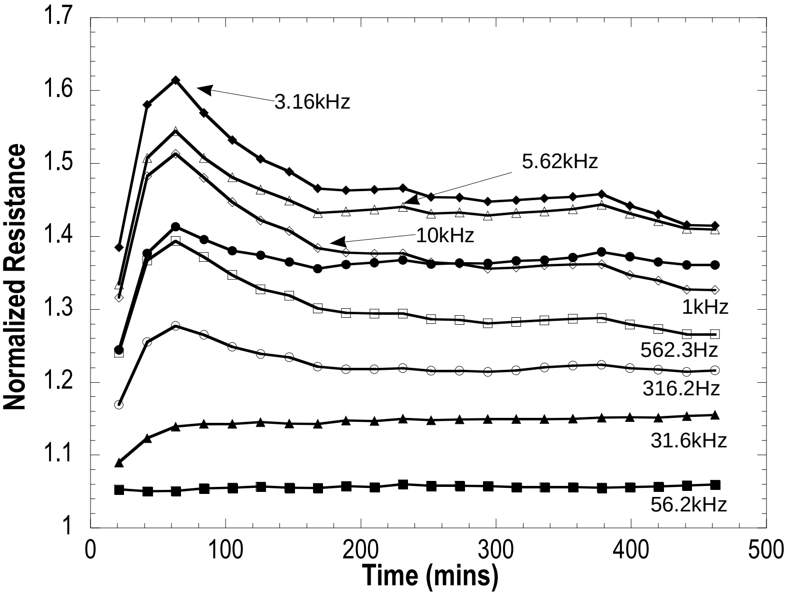

Figure 3.8: A stack of normalized resistance as a function of time during a cellular attachment for a 500 μm ITO electrode. 8 normalized resistances as a function of frequency and time are chosen for the sake of complexity.

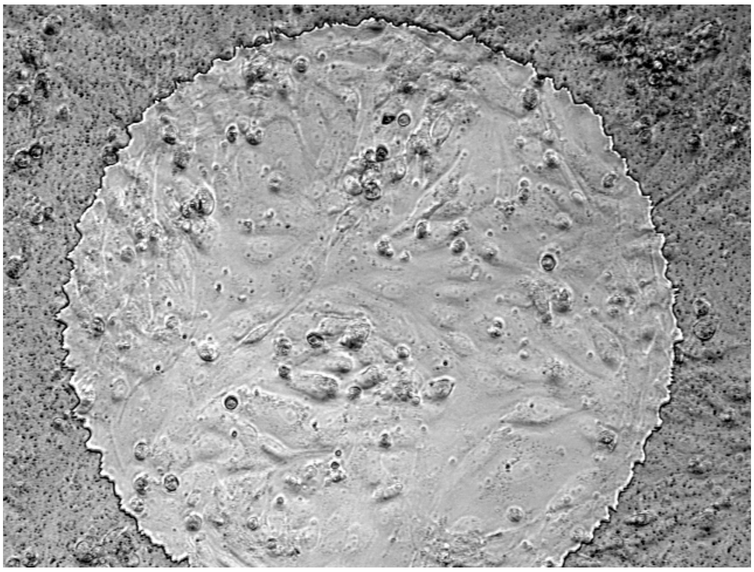

Figure 3.9: Phase contrast cell image on the 500 μm ITO- Si_3N_4 electrodes. All the attached scan wells in each electrode have similar cellular attachment patterns. The image size is 615.5 μm x 461.4 μm. The darker gray region outside the exposed circular electrode region represents the Si_3N_4 layer.

CHAPTER 4

SIMULTANEOUS OPTICAL AND ELECTRICAL PROPERTIES OF ENDOTHELIAL CELLS' ATTACHMENT ON ITO BIOSENSORS

4.1 Cytoskeleton and Morphology

The ability of eucaryotic cells to adopt a variety of shapes and to carry out coordinated and directed movements depends on a complex network of protein filaments that extend throughout the cytoplasm. This network, or the cytoskeleton, is a highly dynamic structure that reorganizes continuously as the cell changes its shape, divides, and responds to its environment. It is also responsible for the crawling of cells on a substratum, muscle contraction, shape changes of a developing vertebrate embryo, and the machinery for intracellular movements such as the transport of organelles from one place to another in the cytoplasm. It is, furthermore, responsible for the segregation of chromosomes during mitosis [121] .

The characteristics of cytoskeleton can be expressed simply: first, actin filaments are essential for many movements of the cell, especially those at its surface; second microtubules are thought to be the primary organizers of the cytoskeleton; finally, intermediate filaments, which have a rope like structure provide cells with mechanical strength [121, 130-133].

The cytoskeleton has been known to be mainly composed of actin filaments, microtubules and intermediate filaments. Each type of filament is formed from a different protein subunit: actin proteins for actin filaments, tubulin proteins for microtubules, and a family of related fibrous protein, such as vimentin or lamin for intermediate filaments. A wide variety of accessory proteins that bind to the actin or microtubulin enables distinct functions of the filaments in different regions of a cell. These also link filaments to one another or to other components, such as the plasma membrane. Furthermore the rate and extent of the filament polymerization are controlled in many ways. Among the filament related proteins, motor proteins hydrolyze ATP to produce force and directed movement along the filaments. The cytoskeleton enables the living cell, like a city, to have many specialized services concentrated in different areas but extensively interconnected by paths of communication.[122-129]

4.1.1 Actin filaments

Actin filaments also known as microfilaments (figure 4.1) are two-stranded helical polymers of the protein actin. They have a flexible and dynamic structure, with a diameter of 5-9 nm, and are organized into a variety of linear bundles throughout the cell. They are most highly concentrated in the cortex, just beneath the plasma membrane with a variety of actin-binding protein. This actin-rich layer controls the shape and surface movements of most animal cells.

Actin is a highly conserved cytoskeletal protein that is present at high concentrations in nearly all eucaryotic cells. Purified actin exists as a monomer in low ionic strength solutions and spontaneously assembles into actin filaments on addition of salt provided ATP is present. As with tubulin, the polymerization of actin is a dynamic process that is regulated by the hydrolysis of a tightly bound nucleotide. In cells, approximately half of the actin is kept in a monomeric form through its binding to small

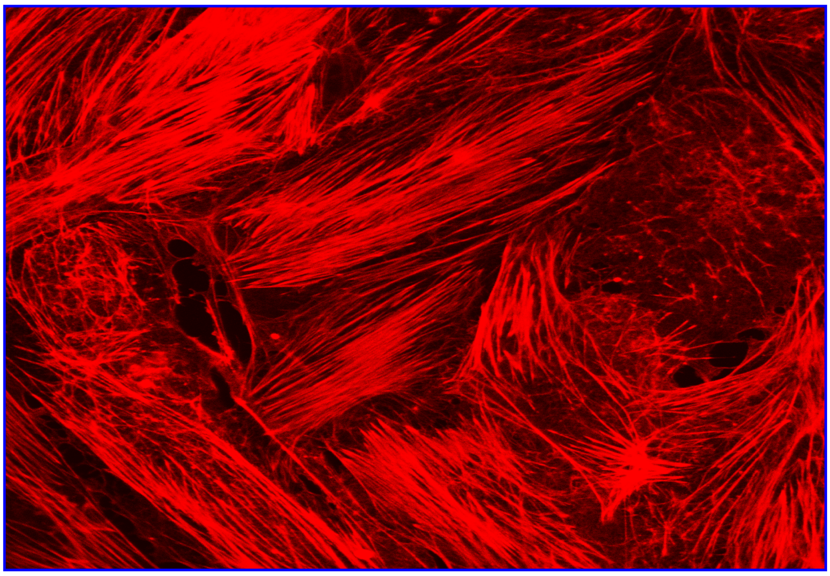

Figure 4.1: A stained confocal image of actin filament using Texas Red Dye.

proteins such as thymosin. In the cortex of animal cells, actin molecules continually polymerize and depolymerize to generate cell-surface protrusions such as lamellipodia and microspikes. Polymerization can be regulated by extracellular signals binding to cell-surface receptors that act through heterotrimeric G proteins and the small GTPase Rac and Rho. The varied forms and functions of actin in eucaryotic cells depends on a versatile repertoire of actin-binding proteins that cross-link actin filaments into loose gels, bind them into stiff bundles, attach them to the plasma membrane, or forcibly move them relative to each other. Tropomyosin, for example, binds along the length of actin filaments, making them more rigid and altering their affinity for other proteins. Filamin cross-links actin filaments into a loose gel. Fimbrin and α-actinin form bundles of parallel actin filaments. Gelsolin mediates Ca^{2+}-dependent fragmentation of actin filaments, thereby causing a rapid solation of actin gels. Various forms of myosin use the energy of ATP hydrolysis to move along actin filaments, either carrying membrane-bounded organelles from one location in the cell to another or moving adjacent actin filaments against each other. Sets of actin-binding proteins are thought to act cooperatively in generating the movements of the cell surface, including cytokinesis, phagocytosis, and cell locomotion.

4.1.2. Intermediate filaments

Intermediate filaments are tough and rope-like fibers with a diameter of approximately 10 nm. They are made of intermediate filament protein, which constitute a large and heterogeneous family. One type of intermediate filament forms a meshwork called the nuclear lamina just beneath the inner nuclear membrane. Other types extend across the cytoplasm, giving cells mechanical strength and carrying the mechanical stresses in an epithelial tissue by spanning the cytoplasm from one cell-cell junction to another.

Intermediate filaments are strong, rope-like polymers of fibrous polypeptides that resist elongation and play a structural or tension-bearing role in the cell. A variety of tissue-specific forms are known that differ in the type of polypeptide they contain: these include the keratin filaments of epithelial cells, the neurofilaments of nerve cells, the glial filaments of astrocytes and Schwann cells, the desmin filaments of muscle cells and the vimentin filaments of fibroblasts and many other cell types. Nuclear lamins, which form the fibrous lamina that underlies the nuclear envelope, are a separate family of intermediate filament proteins. The monomers of different types of intermediate filaments differ in amino acid sequence and have very different molecular weight. But they all contain a homologous central rod domain that forms an extended coiled-coil structure when the protein dimerizes. Two coiled-coil dimers associate with each other to form a symmetrical tetramer, which in turn assembles in large overlapping arrays to form the nonpolarized intermediate filaments. The rod domains of subunits form the structural core of the intermediate filament, whereas the domains at either end can project outward. One function of the variable terminal domains may be to allow each type of filament to associate with other components in the cell, so as to position the filaments appropriately for a particular cell type.

4.1.3 Microtubules

Microtubules are long, hollow cylinders made of the protein tubulin. With an outer diameter of 25 nm, they are much more rigid than actin filaments. Microtubules are long and straight and typically have one end attached to a single microtubule organizing center (MTOC) called the centrosome while the other remains unchanged in the cytoplasm. In many cells microtubules are highly dynamic structures that alternately grow and shrink by the addition or loss of the tubulin subunits. The motor proteins move in one direction or the other along a microtubule, carrying specific membrane-bounded organelles to desired locations in the cell.

Microtubules are stiff polymers of tubulin molecules. They assemble by addition of GTP-containing tubulin molecules to the free end of the microtubule, with one end (the plus end) growing faster than the other. Hydrolysis of the bound GTP takes place after assembly and weakens the bonds that hold the microtubule together. Microtubule-organizing centers such as centrosomes protect the minus ends of microtubules and continually nucleate the formation of new microtubules, which grow in random directions. Any microtubule that happens to encounter a structure that stabilizes its free plus end will be selectively retained, while other microtubules will depolymerize. The tubulin subunits in microtubules that have been selectively stabilized are modified by acetylation and detyrosination. These alterations are thought to label the microtubule as mature and provide site for the binding of specific microtubule-associated proteins (MAPs), which further stabilize the microtubule against disassembly. In general, dynein move cargo toward the minus ends of microtubules, while most kinesins move cargo toward the plus ends. Such motor proteins are largely responsible for the spatial organization and directed movements of organelles in the cytoplasm.

4.2 Background

Simultaneously acquired optical microscopic images and electrical micro-impedance measurements have a number of potential biomedical applications. Although the information obtained from micro-impedance measurements compliment many existing optical microscopy techniques, it is a complicated and sensitive function of the cellular state. In particular, the measured electrical impedance is a function of the cellular morphology, cell-matrix attachment, and the degree of cell-cell contacts. Combined optical and micro-impedance measurements, therefore, have the potential to elucidate a number of complex cellular processes that optical and electrical measurements are not capable of independently.

A particularly novel approach to cellular impedance measurements was pioneered by Giaever and Keese [92, 94] Since then, electrical impedance measurements have been applied to a number of biological problems that deal with cellular barrier function and adhesion [101, 109, 134]. Electrical impedance measurements have been used to evaluate the model parameters associated with cell-cell and cell-matrix junction formation [135, 136]. In addition, measurements at a single frequency have found applications in cellular motility studies. The vast majority of these studies, however, have been performed using gold microelectrode arrays. Although gold electrodes have attractive properties, they are relatively opaque, making simultaneous microscopy measurements difficult or infeasible in most cases.

Indium tin oxide (ITO) films have the unique property of being both electrically conductive and optically transparent [118-120]. As a result, ITO films have found a number of interesting applications in studying surface molecular biology [115, 117] and excitable cells [112, 113, 116]. There have, however, been surprisingly few ITO applications in the measurement of cellular barrier function. Hilldebrand et al. [137] examined the thrombin induced changes in human umbilical vein endothelial cell barrier function while acquiring phase contrast microscopy images. Choi et al. [138] examined the properties of an ITO silicon nitride electrode and its use to electrically measure the growth, attachment, and response of porcine endothelial cells to the drug Cytochalasin D. The results of these studies demonstrate the potential of ITO bioelectrodes for acquiring simultaneous optical and electrical measurements.

This study examines the time dependent attachment and spreading of porcine pulmonary artery endothelial cells (PPAECs) on optically thin ITO electrodes using concurrent optical and electrical micro-impedance measurements. Specifically, differential interference contrast microscopy (DICM) images are recorded simultaneously with frequency dependent resistance and reactance measurements as a function of time. By digitally processing the images, the time dependent changes in cellular morphology and electrode coverage are obtained and compared with the corresponding impedance measurements.

4.3 Methods and Materials

4.3.1 Cell Culture

Porcine pulmonary artery endothelial cells (PPAECs) were isolated from fresh porcine arteries obtained from a local abattoir. The endothelial cells were removed from the intimal artery walls by carefully scraping them off with a scalpel. The cell culture media consisted of M199 (GibcoBRL) and 10% fetal bovine serum (Hyclone) supplemented with BME vitamins (Sigma), L-glutamine (GibcoBRL), penicillin and streptomycin (GibcoBRL), and BME amino acids (Sigma). The culture was maintained until the cells reached confluence, and then they were passaged. Passaging generally occurred once a week, and passages four through eight were used for testing in this study. Trypsin-EDTA (1X, GibcoBRL) was used to detach cells for passaging and electrode inoculation. Cells were cultivated in an incubator that kept the temperature at 37°C and the CO_2 level at 5%. Cells suspended in M199 were inoculated directly onto a sterilized ITO-Si_3N_4 microelectrode that was not previously coated with any adhesion molecules such as fibronectin.

4.3.2 Microscopy and Image Processing

Figure 4.2 shows a schematic of the optical and electrical impedance measuring apparatus. An SR830 lock-in amplifier circuit generated a current through the ITO electrode and measured the resulting electrode voltage. A computer equipped with a PCMCIA card and a LabView based data acquisition program controlled the amplifier and performed frequency scans. Cells were kept viable using an incubator (WeatherStation, Olympus) that kept the temperature (37°C), humidity, and CO_2 (5%) levels constant. These controlled conditions were crucial to keep cells alive during long time lapse measurements. The imaging system consisted of a 20 long working distance objective lens with a numerical aperture (NA) equal to 0.4, an Olympus Model IX-71 inverted microscope with a polarizer (IX-LWPO), a DIC prism (IX2-DIC20) in the long working distance DIC condenser (IX2-LWUCD, NA=0.55), a transmitted Nomarski prism (U-DICTS), an analyzer (IX2-AN), a 100 W Halogen lamp house (U-LH100-3, Olympus), and a Hamamatsu 14-bit electron multiplier (EM) cooled and intensified-

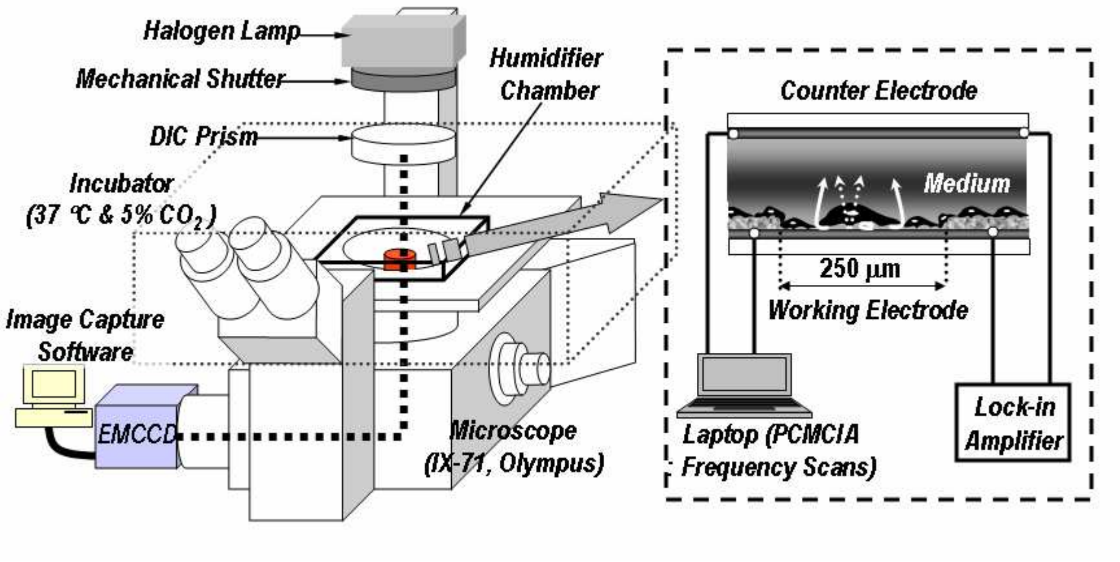

Figure 4.2: Integrated optical and electrical impedance measurement system schematic. Differential interference contrast microscopy images are acquired simultaneously with electrical impedance measurements. An environmental chamber maintains a humidified, 37°C, and 5% CO_2 atmosphere for dynamic long time-lapse measurements. The measured impedance is a function of the current flow under the cells, between the cells, and the capacitively coupled current through the cell membranes.

CCD digital camera. Additionally, a mechanical shutter was synchronized with the CCD camera to minimize any effects the halogen lamp may have had on cell growth [139]. The total magnification used in the current imaging system was 32X, resulting from a 20X objective lens and a 1.6X lens in the DIX71S1F, which approximately fit the entire ITO working electrode. Differential interference contrast image and impedance measurements were taken simultaneously at three minute time intervals.

Image processing was performed using a series of deconvolution and edge detection filters to identify the cell boundaries and to estimate the total cell covered electrode area. Each image was deconvolved using a Lucy-Richardson deconvolution algorithm with a Gaussian point spread function and the background was removed from the cell-covered areas using high and low threshold limits [140]. Binary images were obtained using Canny and Sobel filters. An overlay image was subsequently constructed to compare the digitally processed image with the original image. This permitted the cell-covered area to be quantified by determining the total number of pixels that had not been eliminated by the filters.

4.3.3 Electrical impedance measurements

Electrical impedance measurements were performed using a Stanford Research SR830 lock-in amplifier. A 1 $v_{p\text{-}p}$ ac signal was generated and connected to an electrode array via a 1 MΩ resistor. Although this provided an approximately 1 μA current source, corrections based on the circuit model were made to estimate the actual impedance from the electrode voltage measurement. The lock-in amplifier had an input impedance characterized by a parallel combination of a 10 MΩ resistor and a 25 pF capacitor. The ac voltage source resistance was 50Ω, and the capacitance of each coaxial lead, C_{pv}

and C_{ps}, was approximately 86 pF. Fabrication of the ITO electrodes is explained in detail in a previously published paper[138].

The voltage was sampled at a rate of 32 samples per second using a filter time constant of 32 ms and a 12 dB/decade roll off every 3 minutes. The averages and standard deviations of the 32 sampled voltages were calculated for each set of measurements. Frequency sweeps using 15 logarithmically spaced frequency samples between 10 Hz and 100 kHz were obtained for the naked electrode and the cell inoculated electrode during cellular attachment.

4.4 Results

4.4.1 Electrical scan summary

Figure 4.3 shows the time dependent changes in normalized resistance and reactance at 1.0 kHz, 1.77 kHz, 3.16 kHz, and 5.62 kHz during the attachment of PPAECs to a 250 μm diameter ITO electrode. The zero time point corresponds to the cell inoculation time. The normalized resistance, $(R_c-R_n)/R_n$, and the normalized reactance, $(X_c-X_n)/X_n$, were calculated from the cell covered and naked electrode resistances, R_c and R_n, and reactances, X_c and X_n, respectively. An initial peak in the normalized resistance and reactance occurred approximately four hours after cell inoculation on the ITO electrodes. Following the initial peak, the normalized resistance and reactance stabilized and slowly decreased over several hours. The normalized resistive component of the naked electrode was consistent with small amounts of drift. In addition, changes in both the resistive and reactive components were observed during the first several scans until the environmental chamber parameters, such as the CO_2 level, pH, and temperature stabilized.

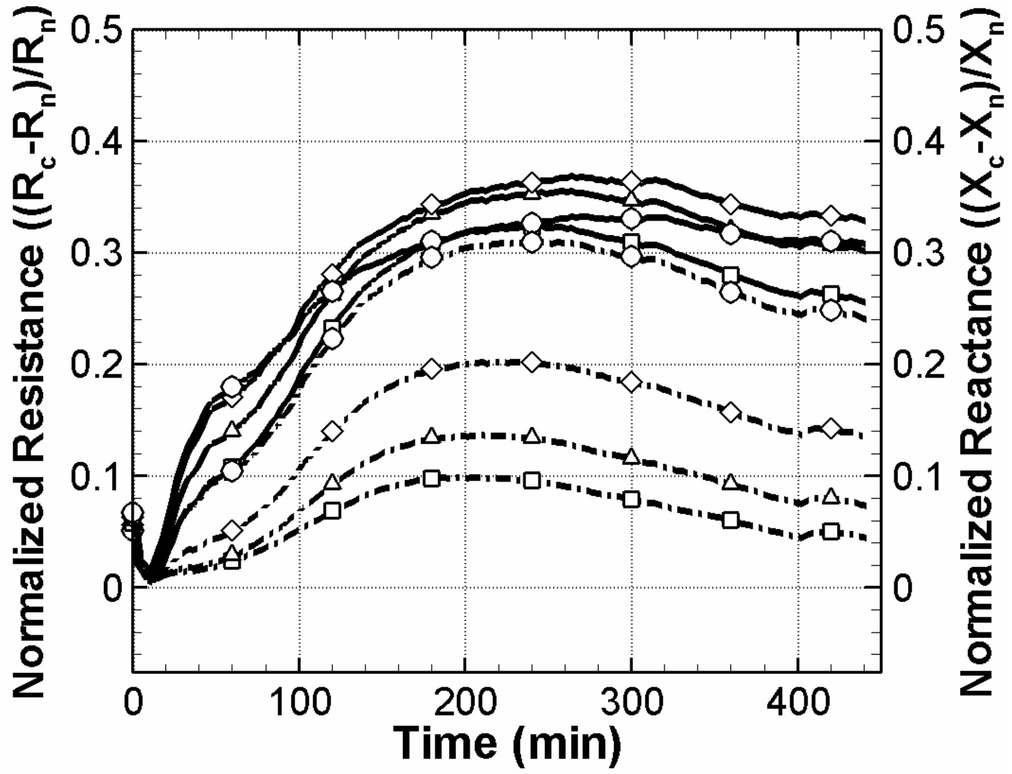

Figure 4.3: Normalized resistances (solid lines) and normalized reactances (dashdot lines) as a function of time. The terms *R* and *X* represent the resistance and reactance, respectively and the subscripts *c* and *n* indicate cell covered and naked scans, respectively. Among the 15 frequency scans acquired, four representative frequencies are selected to illustrate the cellular attachment of PPAECs to a 250 μm ITO electrode. For the sake of clarity, every 20th data point is marked with symbols; □ for 1.0 kHz, Δ for 1.77 kHz, ◊ for 3.16 kHz, and O for 5.62 kHz.

Figure 4.4 summarizes the time dependent evolution of the normalized resistance and reactance as a function of frequency. The normalized resistance peaked around 1 kHz while the normalized reactance appeared to increase with increasing frequency following an initial attachment phase. The resistance and reactance changes were a complex function of the endothelial cell attachment, spreading, and micromotion. Although the impedance measurements were a sensitive function of the cellular attachment parameters, these measurements alone could not sufficiently evaluate the dynamic cellular morphology changes coupled to the cell-cell and cell-substrate adhesion, and cell-covered area on the working electrode.

4.4.2 Image segmentation and cell covered area estimation

Figure 4.5 shows a time series of DICM images of endothelial cells on a 250 μm diameter ITO electrode following a sub-confluent and confluent endothelial cell inoculation. The first row shows the sub-confluent time series, and the second row shows the confluent series. During the endothelial cell attachment and spreading process, the cells start with a globular morphology and then gradually flatten. In the sub-confluent case, approximately 25 cells became attached to the working electrode. At 6 minutes after inoculation of cells onto an ITO electrode, two cells began to spread, while the rest retained their globular morphology for approximately 30 to 33 minutes. In the confluent case approximately 6 minutes after inoculation, a few cells began spreading, while most cells remained globular for approximately 30 to 33 minutes. The cell-covered areas remained almost constant after the PPEACs reached confluence. However, the cells became more tightly packed and much flatter over time. There were approximately 55 and 65 cells on the working electrode at t = 450 minutes and t = 900

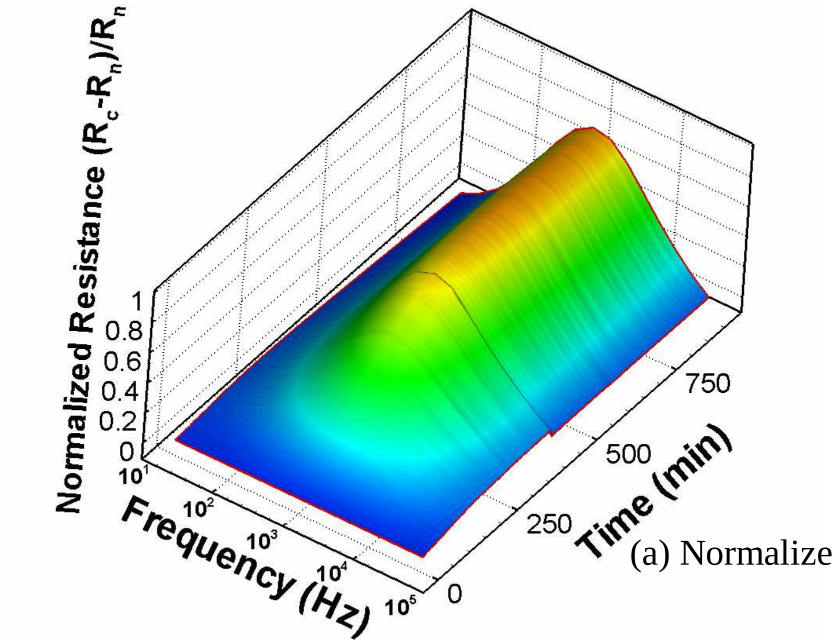

(a) Normalized resistance

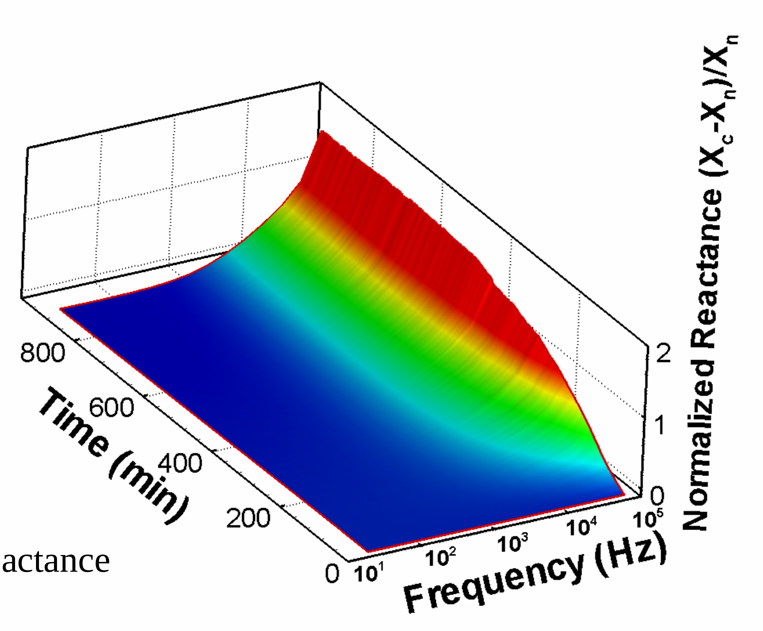

(b) Normalized reactance

Figure 4.4: Representative surface plots of normalized resistance (a) and reactance (b) attach scans of PPEACs on a 250 μm diameter ITO electrode as a function of frequency and time following a confluent inoculation density. The surfaces consist of approximately 300 frequency spectrum scans that were sampled at three minute time intervals.

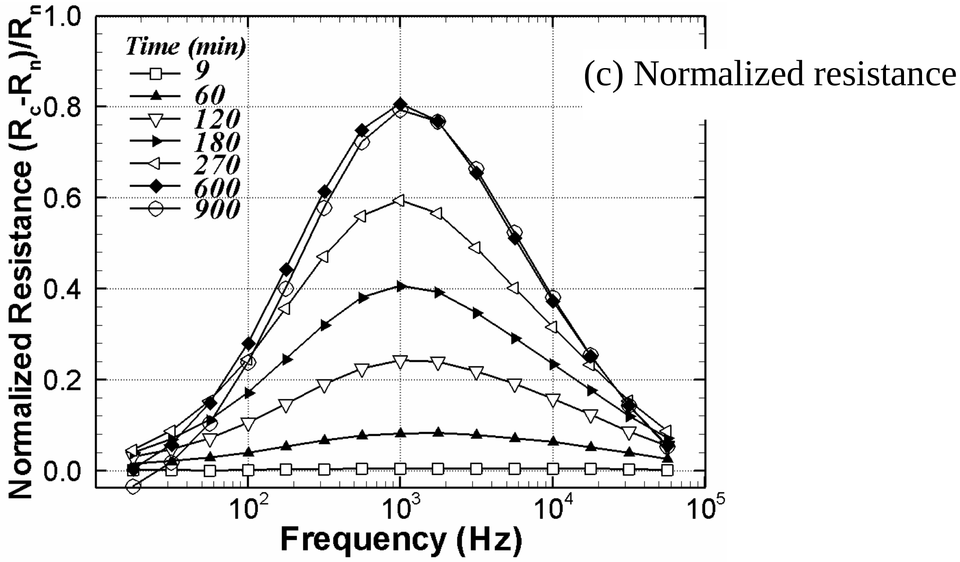

(c) Normalized resistance

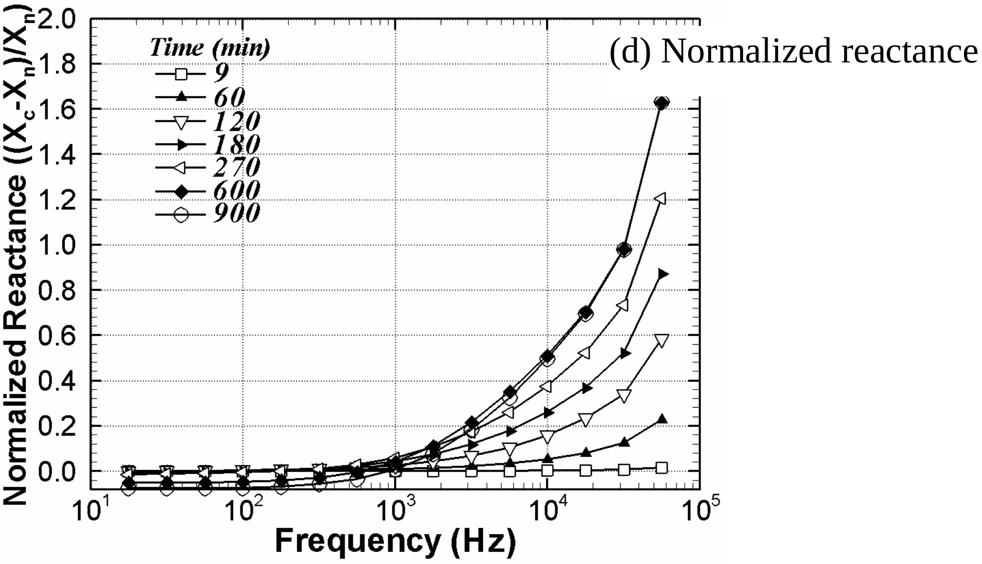

(d) Normalized reactance

Figure 4.4: Continued. Representative surface plots of normalized resistance (a) and reactance (b) attach scans of PPEACs on a 250 μm diameter ITO electrode as a function of frequency and time following a confluent inoculation density. The surfaces consist of approximately 300 frequency spectrum scans that were sampled at three minute time intervals. Plots (c) and (d) show normalized resistance and reactance, respectively for PPEACs' attachment at *t* = 9 min, 60 min, 120 min, 180 min, 270 min, 600 min, and 900 min. (c) The normalized resistance as a function of frequency shows a monotonic increase with time up to approximately 600 minutes at which point saturation occurs. (d) The corresponding normalized reactance also shows an increase with time during the cellular attachment phase.

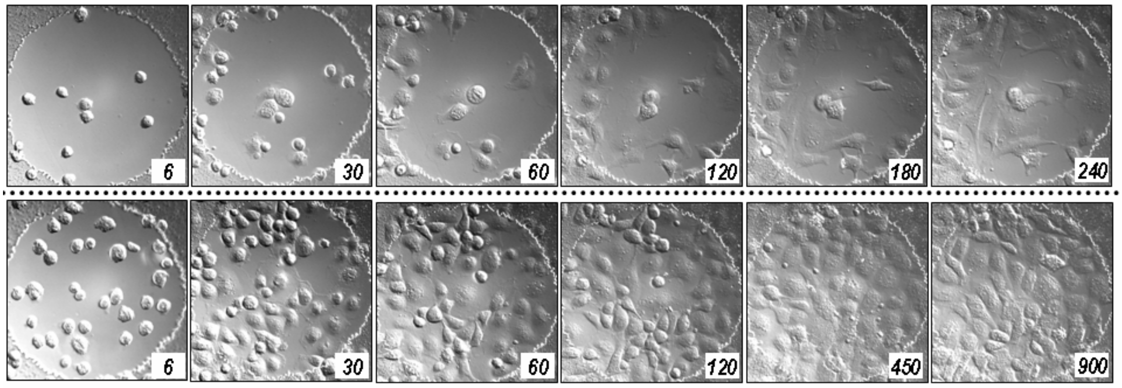

Figure 4.5: Differential interference contrast microscopy images of PPAECs on a 250 μm diameter ITO-Si_3N_4 electrode. The top row shows a set of images for a sub-confluent inoculation and the bottom row shows a set of images for a confluent inoculation. The magnification is 32x providing a 250 μm x 250 μm field of view. The initial inoculation density was carefully chosen to produce either a sub-confluent or confluent endothelial cell attachment pattern.

minutes, respectively. For both sub-confluent and confluent endothelial cell inoculations, the time required for the initial cell spreading stayed relatively constant. Another comparison made for these two cases was the settling time, defined as the initial time when the number of cells remained constant for a period of 4 consecutive images. The settling time for the confluent case was approximately 15 to 18 minutes, while the settling time for the sub-confluent case was approximately 21 to 27 minutes.

Figure 4.6 summarizes the image processing results used to evaluate the cell covered electrode area in this study. A deconvolved image, (a), was first obtained using a Gaussian point spread function. The following image, (b), removed a portion of the background from the cell-covered areas using high and low threshold limits, while a complete binary image, (c), was separately obtained using a Canny or Sobel filter. The local gradients were compared to high and low threshold values, either provided by the user or internally calculated, to roughly detect the cell boundary. A pixel by pixel comparison of images (b) and (c) was then made to more accurately define the cell membrane boundaries. Generally, a portion of each cell was removed using the threshold filter since some of these pixels had similar intensities compared to those of the surrounding medium. This is a general characteristic of differential interference contrast microscopy (DICM). The intensities in a cell varied from darker to brighter or brighter to darker along the shear axis. The diagonal filter compensated for this eliminated area and specified single cells. Another filter, called a stitch filter, was employed to completely fill holes in cells to produce image (f). Finally, a removal filter deleted the defects that appeared as cells but were possibly small air bubbles or optical artifacts. The final overlay image, (h), was constructed from images (a) and (g), to compare the

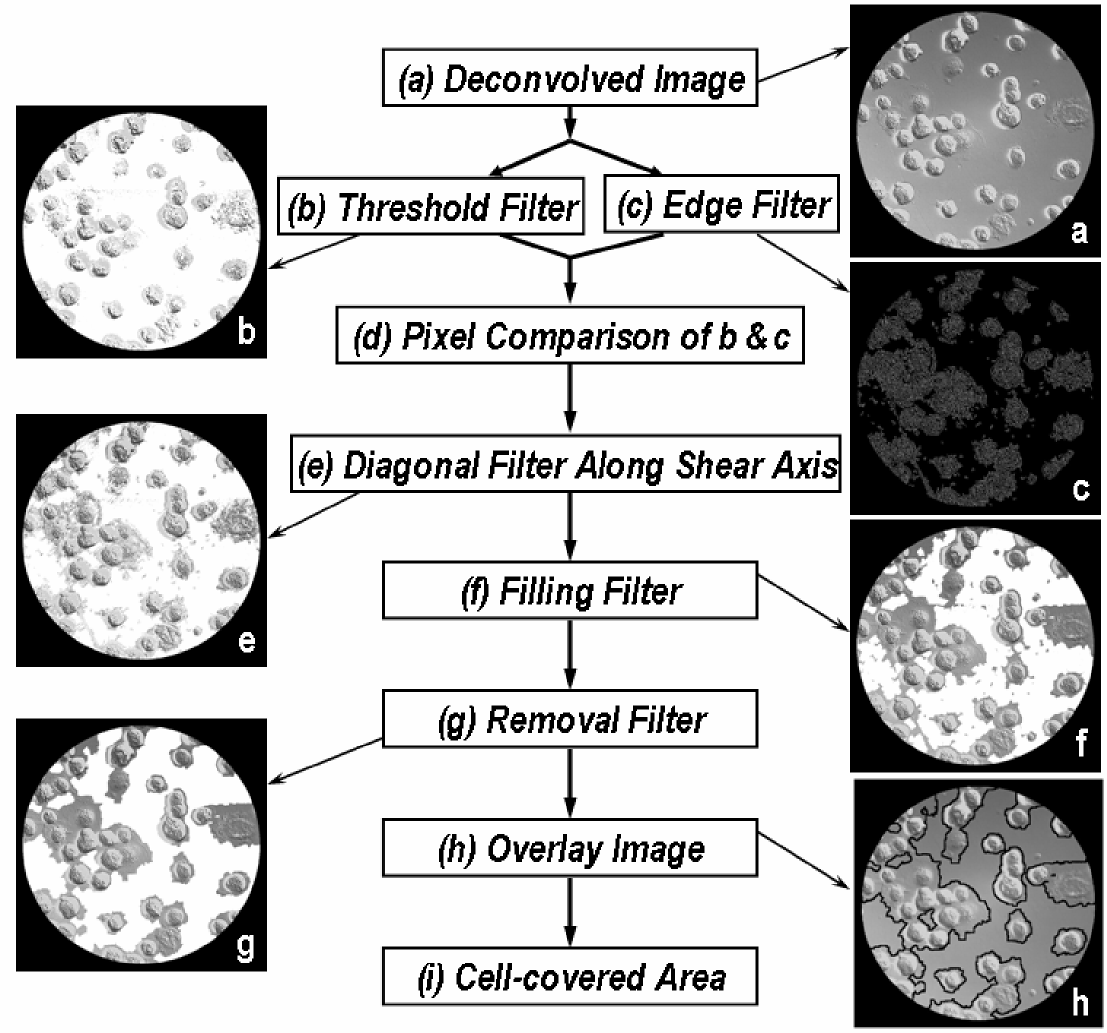

Figure 4.6 Image processing flow chart and digitally processed images following each filter step. To automate the cell covered area estimation, a sequence of image processing steps is carried out. (a) Deconvolved image with examined area outside electrode set to zero. (b) After applying threshold filtering with high and low threshold limits. (c) Binary image created using a Canny filter. (d) Image after combining (b) and (c). (e) After applying diagonal filter along the shear axis. (f) After the filling filter. (g) After removal filter. (h) Overlaying image with (a) and (g) for the comparison of actual and calculated areas.

digitally processed image with the original image. The last image (h) gives the area covered by cells using the image processing algorithm and quantifies any eliminated or overestimated areas produced by the algorithm.

Figure 4.7 shows 4 digitally processed representative overlay images of PPAECs and normalized cell-covered area as a function of time. The imaging processing software identified single cells and their boundaries until they reach confluence. Overlay images were used to visually check cell-occupied areas overestimated or discarded from digital image processing. The graph validates the results obtained by digital image processing by comparing them with those acquired by manual area estimation. The average difference between digital image processing and manual area estimation for each experiment was observed to be less than 5%.

4.4.3 Combined Opto-electric Analysis

Figure 4.8 compares the time dependent changes in the normalized resistance and normalized cell-covered area for a sub-confluent and confluent cell inoculation. In both cases, the normalized resistance did not completely reflect the amount of the electrode covered with cells. Changes in cell-matrix and cell-cell attachment, which altered the resistance, complicated the correlation between cell covered area and resistance. In both cases, however, their time dependent patterns are similar.

Figure 4.9 illustrates the changes in normalized resistance with normalized cell-covered area for both the sub-confluent and confluent cases. Three distinct intervals are considered and will be referred to as the settling zone, the linearly correlated zone, and the saturated zone. For the settling zone, the normalized cell-covered area first increases abruptly due to the increasing number of cells. A total of 25 cells in the sub-

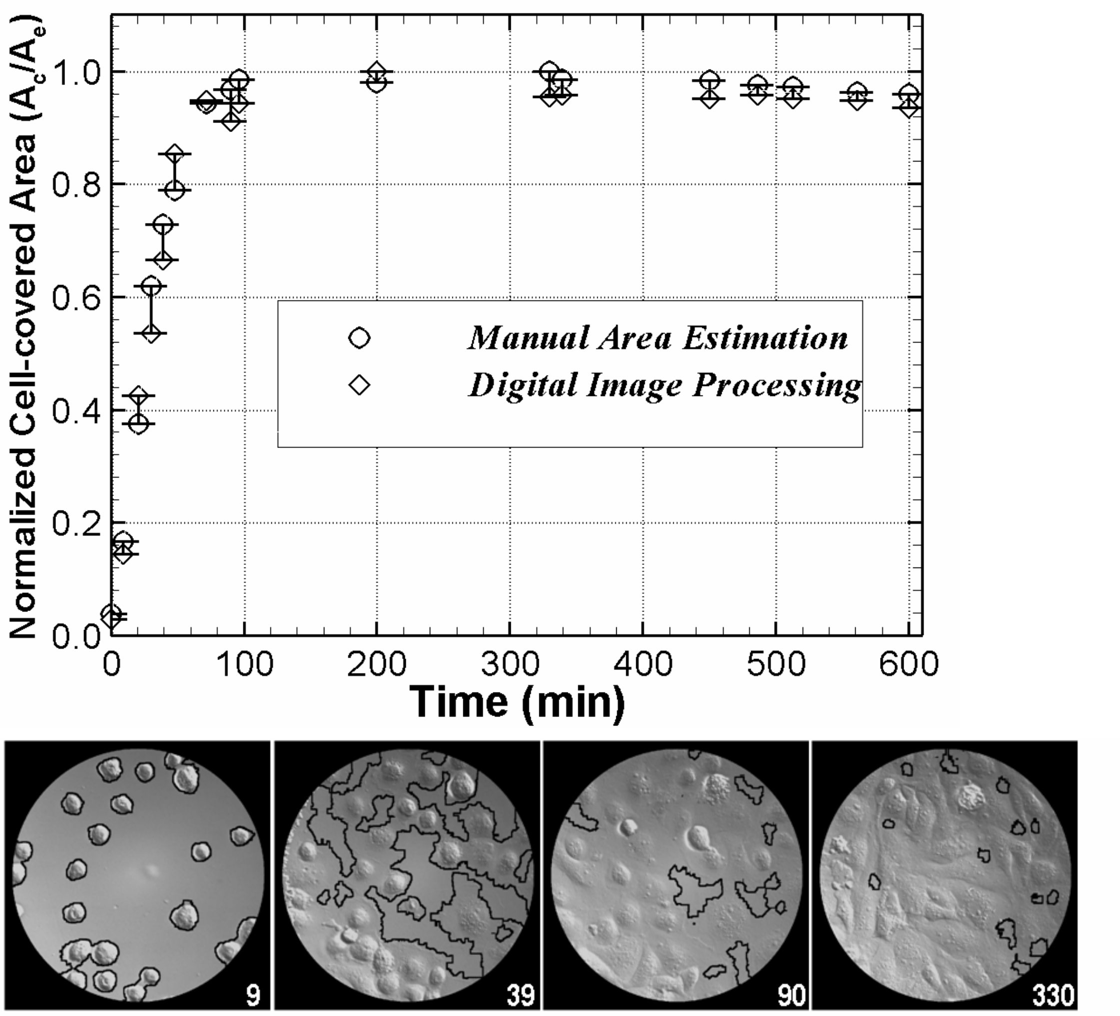

Figure 4.7: Overlay images comparing the cell covered areas estimated using the image processing algorithm and manual cell covered area estimates. The overlay images are used to visually check the areas that are discarded or overestimated after image processing. The graph validates the cell-covered area estimates obtained from digital image processing by comparing those obtained by manually tracing the cell boundaries. The maximum difference between the two methods is approximately 8% for this sample where cells reached confluence at approximately 100 minutes. The term A_c denotes the cell-covered area and A_e denotes 0.043 mm^2 electrode area.

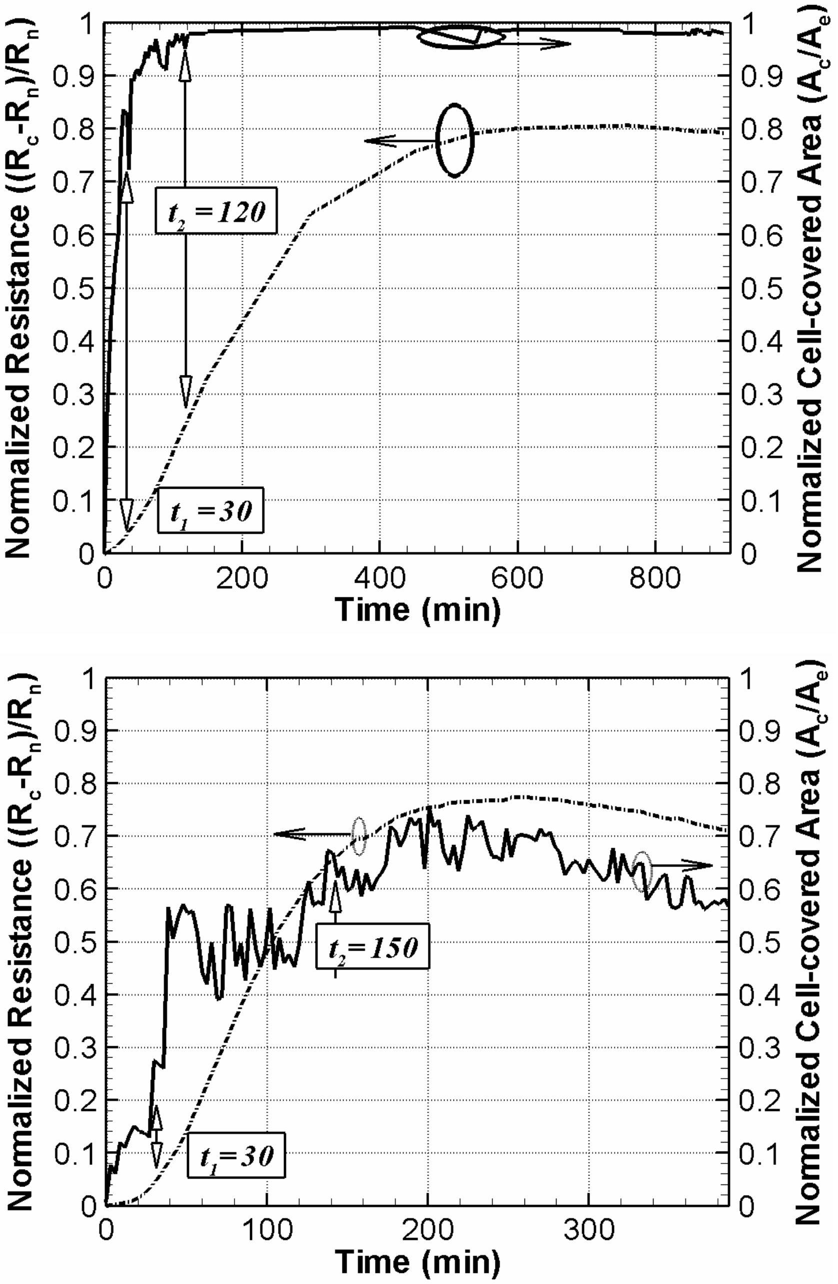

Figure 4.8: Normalized resistance (dash lines) and normalized cell covered area (solid lines) versus time for the (a) sub-confluent (b) confluent cases shown in Fig. 5. The normalized resistance and the normalized cell-covered area have similar time dependent-patterns. Both electrical impedance and DICM image data were simultaneously acquired at 3 minute time intervals.

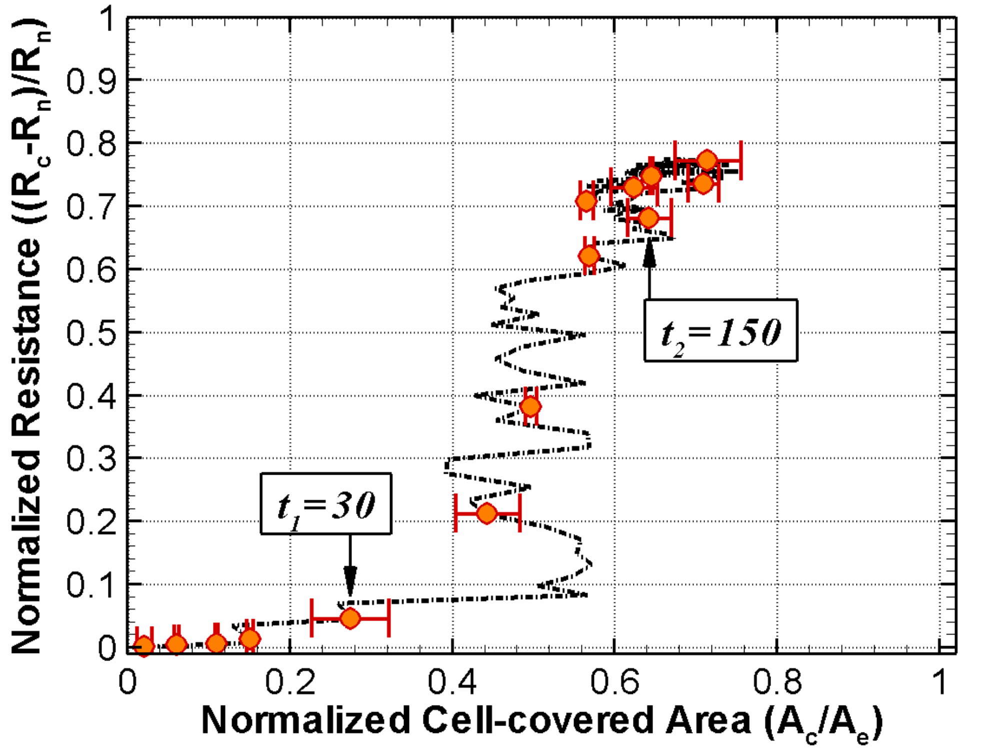

(a) Sub-confluence cell inoculation

Figure 4.9: Normalized resistance versus normalized cell-covered area for the (a) sub-confluent shown in Figure.4.5.

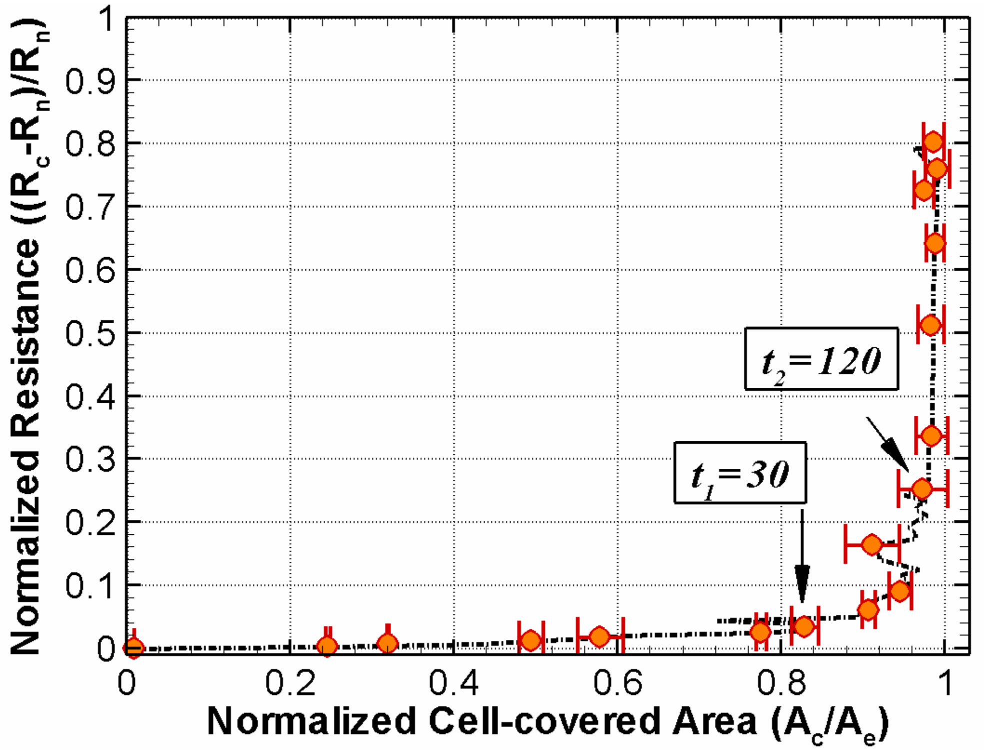

(b) Confluence cell inoculation

Figure 4.9: Continued. Normalized resistance versus normalized cell-covered area for the (b) confluent shown in Figure.4.5. The error bars shown for selected data points indicate the difference between manual area estimates and those calculated using the digital image processing algorithm. Estimated errors for the normalized resistance are smaller than the symbol size. The times t_1 and t_2 represent the times necessary for most cells to spread and the time to reach approximately 5% of their maximum electrode covered area, respectively. For the confluent case, the maximum covered area is approximately 99% of the total electrode surface area and for the sub-confluent case the maximum covered area is approximately 70% of the total electrode area.

confluence case and 65 cells in the confluence case do not appreciably change the normalized resistance. In the linearly correlated zone the normalized cell-covered area proportionally increases with the normalized resistance showing both sub-confluence and confluence cases have an analogous starting time, which is around t_1. Also, a linear relationship between the normalized cell-covered area and normalized resistance is shown. For the saturated zone, in the sub-confluence case the normalized cell-covered area slightly decreases while the normalized resistance remains relatively constant as the cell-substrate adhesion is much tighter and flatter. In the confluent case, however, the normalized cell-covered area remains constant while the normalized resistance continuously increases as a possible result of increasing cell-substrate and cell-cell adhesion. The cells look much flatter and more tightly packed in these cases. Changes in normalized resistance and reactance are a complicated function of the normalized cell-covered area, cell-cell adhesion, and cell-substrate adhesion. All of these factors can be considered both optically and electrically with a transparent conductive ITO electrode. Increasing cell-cell and cell-matrix adhesion states, however, are consistent with the more tightly packed and flatter cell morphologies. This confirms cellular attachment with ITO silicon nitride bioelectrodes as well as demonstrates that the ITO electrode is a good tool for both electrical measurement and optical visualization.

Each sub-confluent and confluent cellular inoculation needs to be considered on a case by case basis. For the confluent case, which lasted up to 19 hours, the cell covered electrode morphology is relatively constant after reaching confluence. However the population of cells was observed to fluctuate. In another confluent case considered in this study, after 13 hours some of the cells appeared to migrate from the working electrode surface to the insulating layer area thus leaving bare areas. In all the sub-confluent cases, the cells migrate more freely than the confluent case, and as a result, there are greater fluctuations in the total cell covered area.

4.4 Discussion

Although electrical signals are extremely sensitive to the different stages of cellular attachment, they are a complicated function of the degree of cell-cell and cell-matrix interaction as well as the fraction of the covered electrode surface area. Several degenerate states, giving similar electrical impedances, can potentially arise under very different degrees of electrode coverage and states of cellular attachment. In some cases, for example, it is possible to have a small fraction of the electrode covered by tightly adhering cells that gives rise to a similar impedance measurement produced by a confluent covering of loosely attached cells. Simultaneous optical images can provide a direct measure of the fraction of the electrode covered by cells and, therefore, remove this ambiguity

The results of this study show that even when the electrode is inoculated with a large density of cells, a finite attachment time is required for cells to completely cover the electrode surface. During this time, it is easy to misinterpret the increasing electrical impedance signal as arising from the increasing degrees of cell-substrate or cell-cell attachment. A direct visual measurement will differentiate these states.

Different normalized resistance values were found for different tests due to several variables. First, the medium for each test may have a slightly different ion concentration. Second, the number of cells on the working electrode, as mentioned previously, varies with each test. Finally, the electrical characteristics of individual electrodes may change slightly over time. Therefore, the impedance values measured with different electrodes and at different times are not appropriate to directly compare with each other. As a result, a more accurate way to examine the effect of cell growth on the change in resistance over time is to supplement the resistance measurements with microscopic images.

The ability to simultaneously perform electrical impedance and optical imaging of cellular cultures has a number of potential applications. Microscopic images permit a more direct picture of cell-cell and cell-matrix states to be interpreted from electrical impedance measurements. The potential application of fluorescent molecules, particularly green fluorescent proteins, or GFPs, offer a number of opportunities for a more quantitative interpretation of electrical impedance measurements. The combination of interference reflection microscopy and electrical impedance measurements may further elucidate the role of cell-matrix adhesion on the electrical signal. In particular, interference reflection microscopy (IRM) may help to quantify the role that cell-matrix separation distance fluctuations play in the measured impedance signal.

Excellent resolution and improved cell boundary visibility can be obtained using DICM, particularly in the adjoining cellular regions that have larger optical gradients. In general, the use of a high numerical aperture objective lens provides optical slicing in a thick specimen without confusing images. The shear axis, which is a chief characteristic in DICM and along which the maximum contrast exists, can be exploited in the application of image processing algorithms, particularly those that implement a diagonal filter. Annoying halos, encountered in phase contrast microscopy (PCM), are absent in DICM images. Plastic materials, such as tissue culture dishes, commercial gold electrode, and other birefringent specimens, however, are not suitable for DICM measurements because of their affect upon polarized light. Thus, in order to properly use the DICM technique, all the materials along the light path must consist of glass since plastics or acrylics change the characteristics of both the ordinary and extraordinary rays. The transparent conductive ITO-Si_3N_4 electrodes used in this experiment are sufficiently compatible with DICM imaging.

Phase contrast microscopy (PCM) yields image intensity values as a function of specimen optical path length magnitude while DICM creates the contrast by optical path length gradients, or the rate of change in the direction of wavefront shear. This is the most important characteristic that is exploited in the digital image processing. Unlike PCM, DICM produces an improved contrast image by introducing bias retardation by the objective Nomarski prism whose net result is to render the image in a pseudo 3-dimensional relief, where regions of increasing optical path difference appear much brighter or darker.

The ITO electrodes used in this study were recyclable and in fact have been used more than 100 times so far without any apparent decrease in performance. Similar gold electrodes can typically be used only once. In addition, the ITO-Si_3N_4 electrodes were resistant to ethanol sterilization. Some forms of photoresist that are used for the insulating layer are solubilized in ethanol and are harder to sterilize and clean for repeated applications. Compared to silicon nitride, initial attempts to use SU-8 as a photoresist were unsuccessful because it was not resistant to ethanol sterilization. When the electrode arrays with an SU-8 photoresist were rinsed with ethanol the SU-8 contracted or shrunk.

In order to effectively determine the settling time and the spreading time higher frame rates are strongly recommended. Additionally higher frames per second are also needed to optically detect micromotion, motility, and cell-cell and cell-substrate interaction in detail. A single frequency scan for the impedance measurement of endothelial cells is desirable to electrically measure their sensitive activities.

4.5 Conclusion

The simultaneous dynamic opto-electric observation of endothelial cells using DICM imaging and impedance measurements provided a clearer interpretation of the time dependent changes associated with cellular attachment and spreading. The combination of optical and electrical methods, therefore, provided a more quantitative and qualitative assessment of dynamic cellular morphology changes, cell-cell and cell-substrate adhesion changes, and cell-covered area changes. The fraction of the cell covered area was in qualitative agreement with the electrical impedance during the attachment phase following cell settling to the electrode surface. Digital image processing automated the cell covered area estimation and was validated using manual area estimation.

CHAPTER 5

CYTOTOXICITY MEASUREMENT

5.1 Introduction

Endothelial cell toxicity [141-145] may be caused by pharmacological agent interaction with membrane molecules that initiate a series of interactive cascades of signaling leading to eventual lesions. Any external stimuli, such as a toxic agent, can perturb cellular membrane functions which are responsible for normal physiological behavior. In particular, drug-induced vascular injury is characterized by inflammation, intimal proliferation, neutrophil infiltration, internal elastic lamina breaks, apoptosis, and aneurysms. Thus, new drug development must consider inevitable toxicological concerns induced by drugs. Therefore, *in vivo* or *in vitro* cytotoxicity experiments are important to examine morphological changes and cellular adhesion changes following the change of membrane molecules caused by toxic agents.

In vivo cytotoxicity experiments use whole animals in testing a new compound and combination of compounds. These experiments, however, are difficult and undesirable are raise concerns regarding animal welfare. As a result, new developments in cost effective cell culture methods are desirable to experimentally manipulate and directly observe the response of living and developing tissue/cells to toxic agents in a controlled setting [141-143, 145].

A major advantage of *in vitro* tissue/cell culture systems is that aspects of metabolic, chemical and morphological changes induced in the cultures by experimental variables can be assessed in a relatively straightforward fashion. Morphological changes can be examined easily and photographed in living cultures using only a light microscope in the following two ways: (1) Cultures can be fixed and stained for more in-depth morphological examination at any time throughout the culture period and (2) cells grown culture dishes are directly visualized without any staining methods.

The primary goal if this study is to examine the bottom morphology changes related to cell-substrate adhesion, i.e., gap between cell and substrate, caused by cytochalasin D[20] onto endothelial cells using dynamic multi-spectrum interference reflection microscopy (MS-IRM). Three complementary method are also included: (1) Biochemical analysis to measure the number of viable cells using spectrophotometry, (2) confocal imaging for cellular imaging after staining fixed cells in cytotoxicity research, and (3) micro-impedance measurement referred to as electrical cell-substrate impedance sensing (ECIS) [92-94, 146].

It should be noted that multi-spectrum interference reflection microscopy (MS-IRM) is one of microscope techniques available in the advance dynamic live-cell opto-electric detection system previously explained as a label-free and dynamic method. To our knowledge, the MS-IRM imaging technique with supplemental bio-chemical and bio-electrical methods is a potential package to examine cytotoxic-induced endothelial cell damage, morphology changes, adhesion changes, and vascular toxicity, which is strongly related to angiogenesis [147-162].

---

[20] Cytochalasin D is a cell permeable mycotoxin, which causes both the association and dissociation of actin subunits, disrupts actin filaments and inhibits actin polymerization. Its molecular weight is 507.6 and formula is $C_{30}H_{37}NO_6$.

5.2 Method and Materials

5.2.1 Cell Culture

Endothelial cells were isolated from porcine pulmonary arteries obtained from a local abattoir. The endothelial cells were cultivated in an incubator at 37 ^{o}C and 5 % CO_2. The cell culture media consisted of M199 (GibcoBRL) and 10 % fetal bovine serum (Hyclone) supplemented with BME vitamins (Sigma), L-glutamine (GibcoBRL), penicillin and streptomycin (GibcoBRL), and BME amino acids (Sigma). The culture was maintained for approximately one week at which point the cells reached confluence. They were then regularly passaged once a week. For this study, passages between four and nine were used for measurements. Trypsin-EDTA (1X, GibcoBRL) was used to detach cells for passaging and electrode inoculation.

5.2.2 Automated Live Cell Imaging System

Figure 5.1 shows a schematic of the dynamic live cell imaging system having phase contrast microscopy (PCM), differential interference contrast reflection microscopy (DICM), and multi-spectrum interference reflection microscopy (MS-IRM). Cells were kept viable using an incubator (WeatherStation, Olympus) that kept the temperature (37°C), humidity, and CO_2 (5%) levels constant. These controlled conditions were crucial to keep cells alive during long time lapse measurements. The imaging system consisted of a 100X objective lens with a changeable numerical aperture (NA) from 0.7 to 1.35, an Olympus Model IX-71 inverted microscope with a polarizer (IX-LWPO), a DIC prism (IX2-DIC100) in the long working distance DIC condenser (IX2-LWUCD, NA=0.55), a transmitted Nomarski prism (U-DICTS), an analyzer (IX2-AN), a phase annulus, a 100X phase objective lens, a 100 W Halogen lamp house (U-LH100-3, Olympus), a Xenon

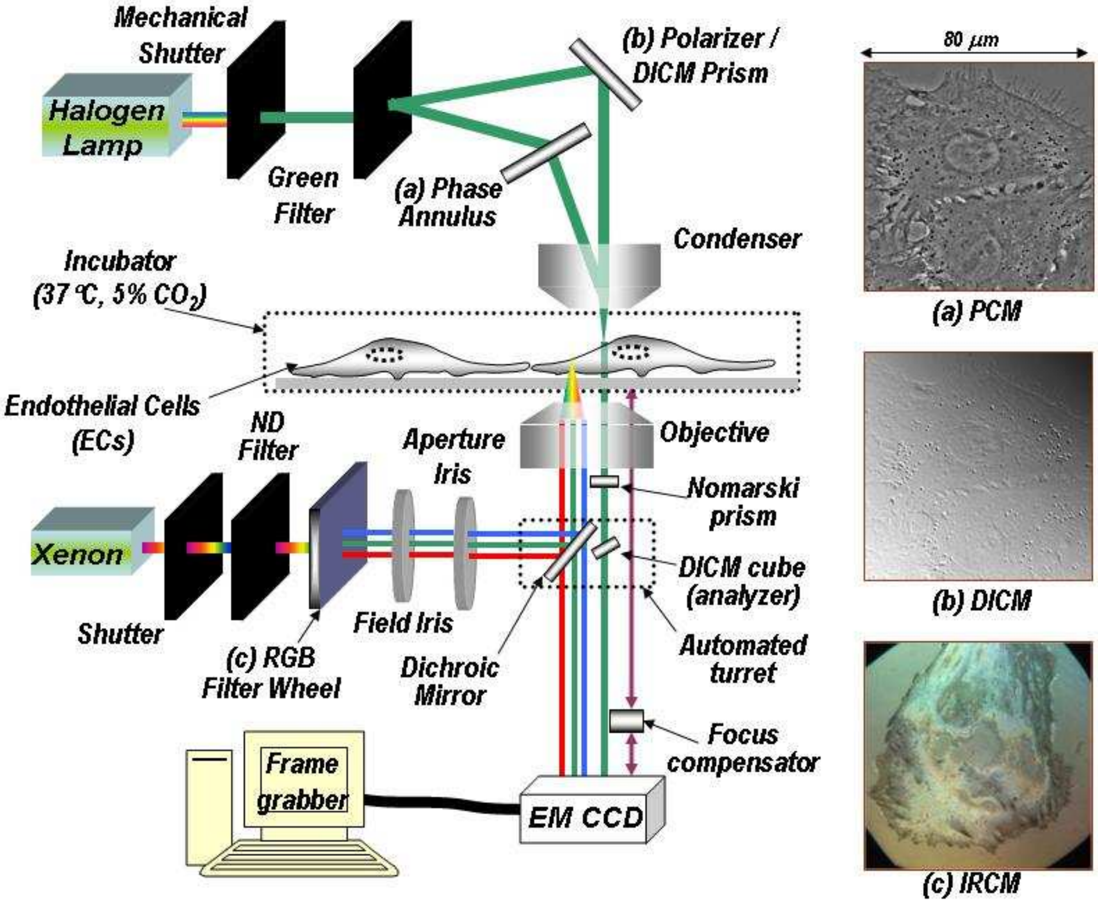

Figure 5.1: Schematic illustration of phase contrast microscopy (PCM), differential interference contrast microscopy (DICM), and interference reflection contrast microscopy (IRCM) used in the dynamic live cell environmental incubation chamber and imaging system.

light, and a Hamamatsu 14-bit electron multiplier (EM) cooled and intensified-CCD digital camera. A filter wheel system[21] was added to allow multi-color blue, green, and red channels. A z-directional control unit (ZDC) acts as a focus drift compensator and uses a 785 nm laser beam on the glass surface to detect the position of the cover glass with respect to the objective. An offset value can be used to assure images are taken at a desired target position.

5.2.3 Micro-impedance

A data acquisition and analysis system was implemented using LabVIEW. The impedance measuring circuit configuration is shown in the schematic illustration in figure 2.1. A reference voltage source provided an ac $1v_{p-p}$ reference signal via a series 1 MΩ resistor, R_{cc}, to the electrode array. A National Instruments SCXI-1331 switch made successive connections between the different working electrodes and the counter electrode of each array. The source voltage generator resistance, R_s, was 50 Ω. Since the series resistance was significantly larger than the electrode impedance over the range of frequencies used in this study, an approximately 1μA constant current was provided.

An SR830 lock-in amplifier, shown in figure 5.2, measured the electrode voltage. The input impedance of the lock-in amplifier was equivalent to a parallel resistor, R_v, and capacitor C_v combination of 10 MΩand 10 pF, respectively. The source and lock-in amplifier cable have parasitic capacitance, C_{ps} and C_{pv}, respectively. Direct measurements of the cable parasitic capacitances were made using a LCR meter and incorporated into the circuit model to estimate the impedance based on the lock-in voltage measurement.

---

[21] In the filter wheel system, mechanical shutters for excitation for transmitted light and excitation and emission for reflected lights were synchronized with the CCD camera to minimize any effects either the halogen lamp or Xenon light may have had on cell growth [139]

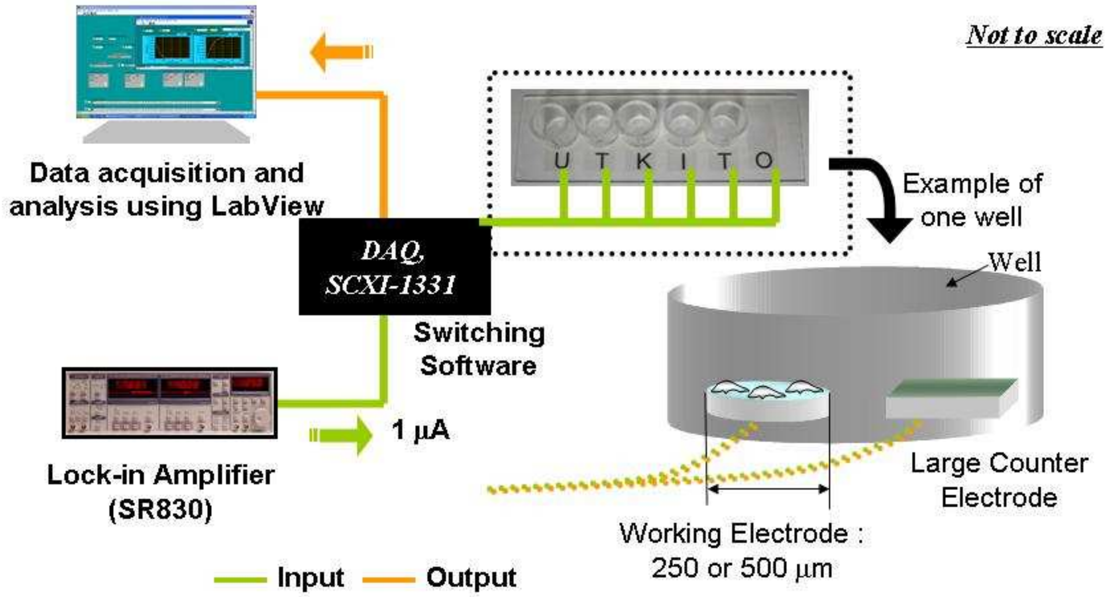

Figure 5.2: Experimental setup for the electrical cell-substrate impedance sensing system. This system consists of a lock-in amplifier, Data acquisition board, computer, and ITO electrodes. The voltage drop across the working and counter electrode is measured. The corresponding impedance is calculated from this measured voltage based on the circuit model (figure 2.1) of this impedance measurement including all the resistance and capacitance from cables and source.

Among a total of 17 even logarithmically space frequencies between 10 Hz and 100 kHz, 5.16 kHz was chosen because this frequency showed the highest sensitivity for cellular attachment and spreading. The preliminary naked scan checked for any debris on the ITO-Si_3N_4 electrodes as well as electrode defects. An one (1) second naked scan sampled at a rate of 32 Hz was then performed for the naked electrodes. The electrodes were then inoculated with 400 μL porcine pulmonary artery endothelial cells (PPAECs) and M199. One well of 500 μm electrode arrays was filled with only medium to provide a control. During the cellular attach scans data was acquired at a rate of 32 Hz for 1 second, using a 30 ms filter time constant and 12 dB/decade roll off.

5.2.4 Proliferation Assay

Endothelial cells were plated into 4 sets of 96 wells with 100 μl, shown in figure 5.3. The number of cells in each well was approximately 4000. The next day, the cells were treated with 0, 0.03, 0.3, and 3 μM of cytochalasin D while the first culture dish was measured spectrophotometry to provide a reference control before being treated. At each time point after cell treatment, 20 μl of Celltiter 96 AQuous one solution was added into each well. The culture dish was left for 1 hour in the incubator and then spectrophotometry measurements were performed.

The Celltiter 96 AQuous one solution cell proliferation assay is a colorimetric method for determining the number of viable cells in culture in a multi-well plate format. It can be used in many applications such as cell proliferation, chemo-sensitivity, cell attachment, and cytotoxicity. This assay can be performed by adding a small amount of Celltiter 96 AQuous one solution reagent directly to culture wells, incubating one to four hours and then recording absorbance at 490 nm with a spectrophotometric plate reader.

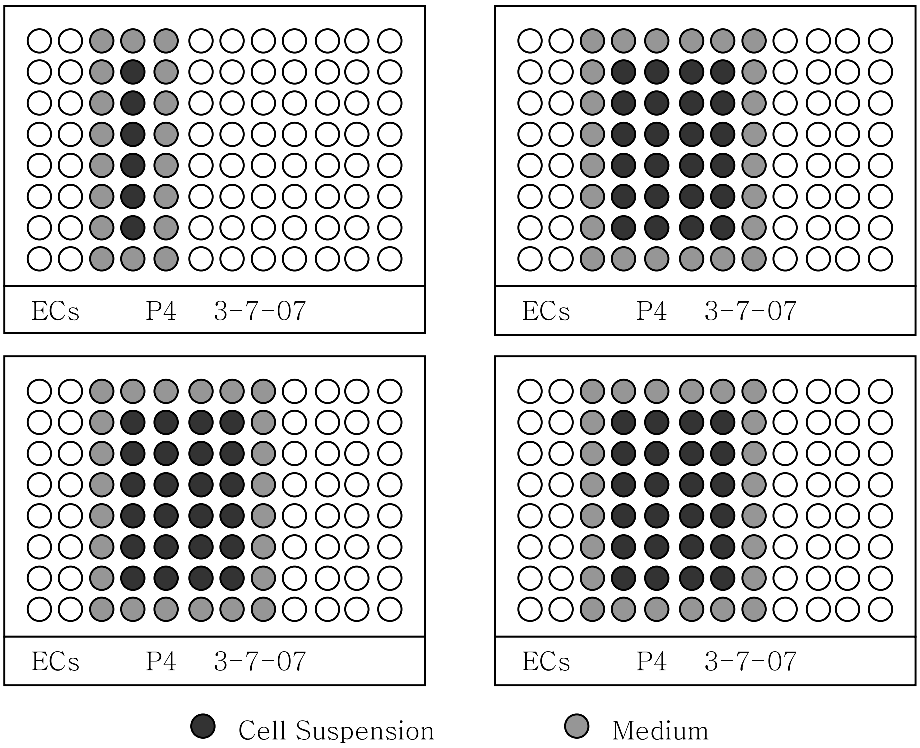

Figure 5.3: Example of plating cells onto 96 wells for cell proliferation assay. After cells are plated, medium only was put into the surrounding wells in order to minimize the evaporation of medium during the experiment.

The quantity of formazan product as measured by the amount of 490 nm absorbance is directly proportional to the number of living cells in culture.

5.2.5 Immunofluorescence

The Immunofluorescence technique consisted of four important procedures namely fixation, permeabilization, blocking and staining. Fixation is the first and foremost procedure which preserves the cellular ultrastructure and antigenic protein sites. The main intent of the fixation procedure is to maintain the original morphology of the cell. There are a plethora of commercially available fixative agents and the choice of the agent depends upon the protein of interest. Formaldehyde is known to preserve actin well, and hence was used as the fixation agent in this case. After proper cell fixation, it was necessary to permeabilize the cells. The goal of this procedure is to permeabilize the plasma membrane so as to make it accessible to the stains and anti-bodies used in the procedure. It is important to block other potential protein-binding sites which would result in non-specific binding. A blocking agent, that does not react with the anti-bodies used but does react with the other potential binding proteins, is selected to perform this task. In this study, Triton-X and BSA were used in appropriate concentrations as the permeabilization agent and blocking agent, respectively. After the above mentioned procedures, the cells were stained for the actin filaments using Phalloidin, commercially available as Texas red dye. On completion of the staining procedure, the sample was taken to the confocal microscopy facility and the imaging session was carried out.

5.2.6 Time-scales in the cytotoxicity measurement

Figure 5.4 shows the time scales of experimental methods used to examine the cytotoxicity effect of cytochalasin D on endothelial cells. First endothelial cells were plated with the appropriate concentration determined by the measurement of interest. The “0” hour time point refers the replacement time for the untreated medium with treated medium containing 3 μM cytochalasin D. At four hours, the treated medium was replaced with complete medium, and at eight hours the experiment was terminated. Thus, all the measurements were done for 4 hours under the toxic agent of cytochalasin D and for another 4 hours after replacing the treated medium with new complete medium. While micro-impedance measurements begin as soon as cells are inoculated onto the electrodes, the biochemical analysis, stained confocal images, and multi-spectrum interference reflection microscopic images typically begin 1~2 days after inoculation in order for the cells to have time to tightly adhere to the substrate.

In the biochemical analysis, spectrophotometry was measured every hour, in the IRM images and micro-impedance analysis were dynamically taken, and only two images were taken for the confocal case one before treatment and one after treatment.

5.3 Results and Discussion

The dynamic response of the cells to different toxins is a valuable tool for many drug delivery systems and tissue engineering applications. This cytotoxicity test can predict the mechanism and structure of cells, such as division, proliferation, and migration as well as cellular morphology changes by analyzing the number of viable cells under the toxic agent of cytochalasin D. Using spectrophotometry, the effect of actin filament exposed to the Cytochalasin D can be examined using stained confocal images.

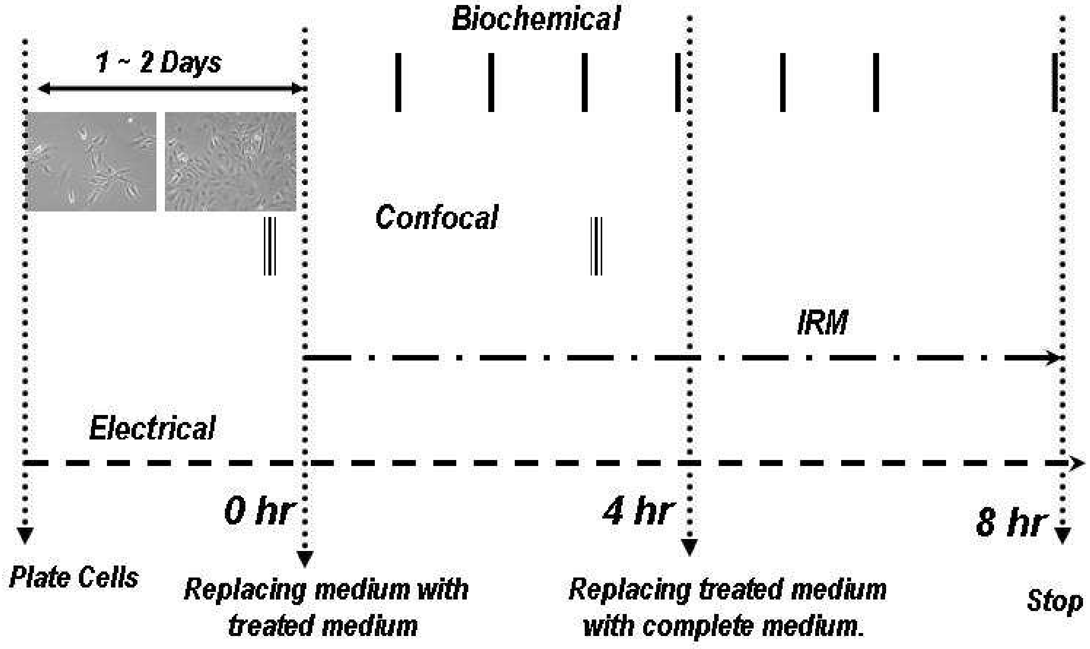

Figure 5.4: Time scales of the biochemical analysis, stained confocal images, multi-spectrum interference reflection microscopic images and the electrical impedance measurements used to examine the cytotoxicity effect of cytochalasin D onto endothelial cells.

In addition, electrical resistance of cells grown a ITO electrode, and the bottom morphology change caused by cytochalasin treatment

5.3.1 Micro-impedance

Figure 5.5 shows the time-dependent normalized resistance with and without the effect of the actin disrupting drug, cytochalasin D on Porcine Pulmonary Artery Endothelial Cells (PPAECs) cultivated on a 500 μm ITO electrode. The normalized resistance for the naked scans shows that there is an acceptably small amount of drift. The cellular attachment, such as the formation of cell-cell and cell-substrate contacts, gives rise to measured changes in the normalized resistance. There is a distinctive peak due to the cellular attachment followed by decease of the normalized resistance observed with some fluctuation in both blue and red lines over the first several hours. Adding cytochalasin D produced a systematic decrease in the normalized resistance and removal of the drug as well as changing of the medium produced an abrupt increase. No significant change in resistance was observed for the normal condition. Another peak of the impedance is shown during the recovery of cellular attachment and the normalized resistance is decreased again as time goes by.

5.3.2 Confocal Images

Figure 5.6 consists of two stained confocal images that illustrate how actin filaments are disrupted under 3 uM cytochalasin D treatment on the Porcine Pulmonary Artery Endothelial Cells (PPAECs). The Immunofluorescence technique has proved to be one of the most efficient ways to look at the cell and its components. It is possible to visualize specific parts of the cell using this method. The actin-filament stained images are used as supporting information of the cellular response to the drug obtained from

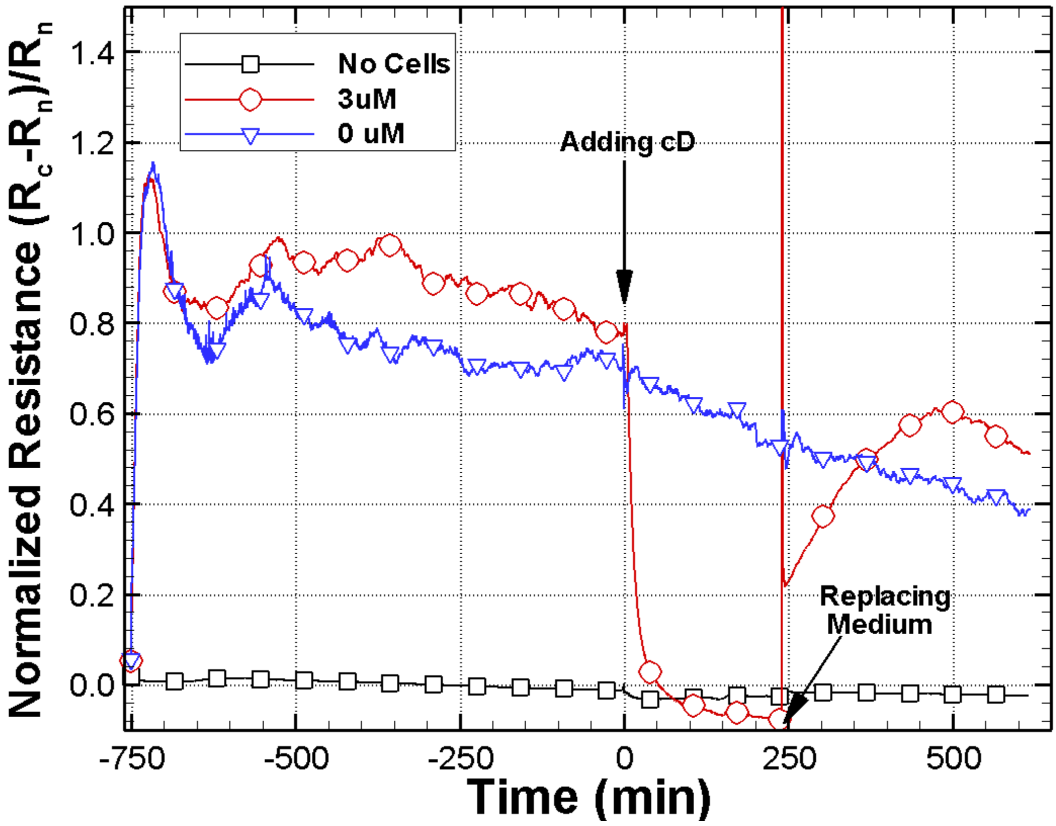

Figure 5.5: Time-dependent normalized resistance with and without the effect of the actin disrupting drug, cytochalasin D on the Porcine Pulmonary Artery Endothelial Cells (PPAECs) on a 500 μm ITO electrode.

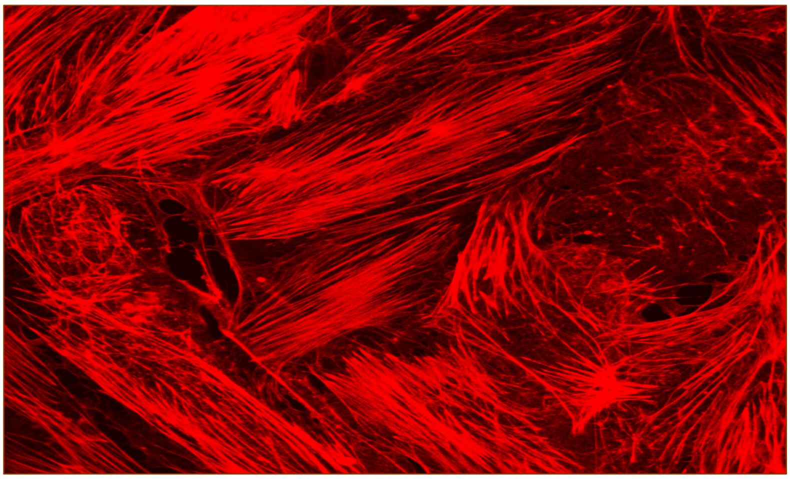

(a) Without cytochalasin D

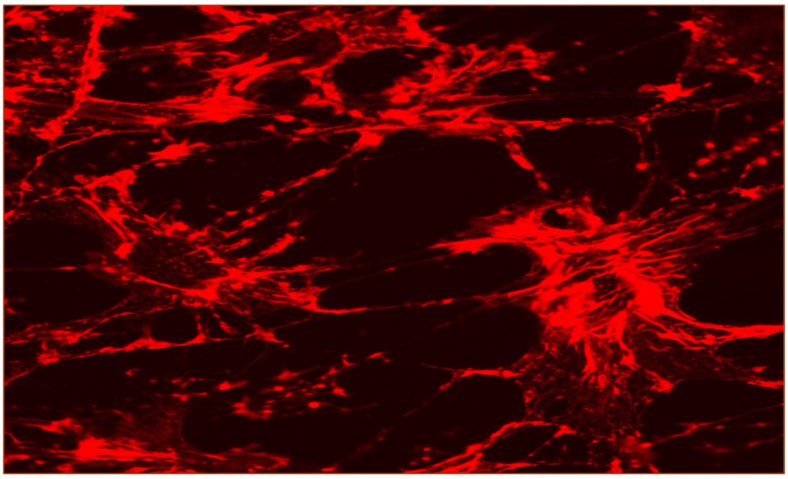

(b) 3 μM cytochalasin D Treatment

Figure 5.6: Two stained confocal images without (a) and with (b) cytochalasin D treatment show how actin filaments are disrupted under a 3 uM cytochalasin D treatment on the Porcine Pulmonary Artery Endothelial Cells (PPAECs).

other methods. The Immunofluorescence technique consisted of four important procedures namely fixation, permeabilization, blocking and staining.

5.3.3 Biochemical Result

Figure 5.7 summarizes the biochemical results cytochalasin D cytotoxicity on endothelial cells. The biochemical analysis results was obtained by recording spectrophotometry the quantity of formazan product produced by living cells in culture. In the figure 5.7 (a) it is observed that for all concentrations of cytochalasin D less than 3 μM, cells proliferate while a 3 μM concentration of cD, cells appear to die. Because the first few hours under 3 μM concentration were interesting, a second experiment using different time scales was conducted. As expected, a decrease in the number of viable cells is observed under toxic conditions while after replacing the treated medium with new complete medium they appear to recover.

5.3.4 MS-IRM

Color fringe patterns are ubiquitously seen as long as there is a thin film present. For example, an oil film on water, an air or water film between coverslips, and soup bubbles in the air can produce color fringe patterns that can be captured using our advanced multi-spectrum interference reflection microscopy. This concept is applied to examine the gap morphology between a cell and substrate as this gap is made of a very thin medium film. Interference reflection microscopy thus allows the visualization of cell-substrate adhesions, such as focal contacts which appear as darker streaks and are located closest to the surface, close contacts shown to be dark areas which are a little further away than focal contacts, and

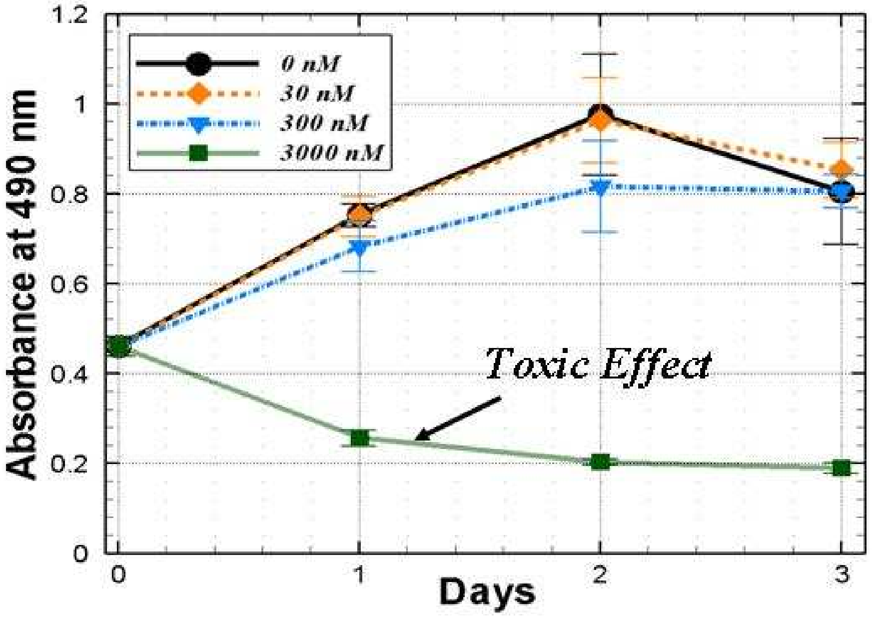

(a) As a function of days and dose

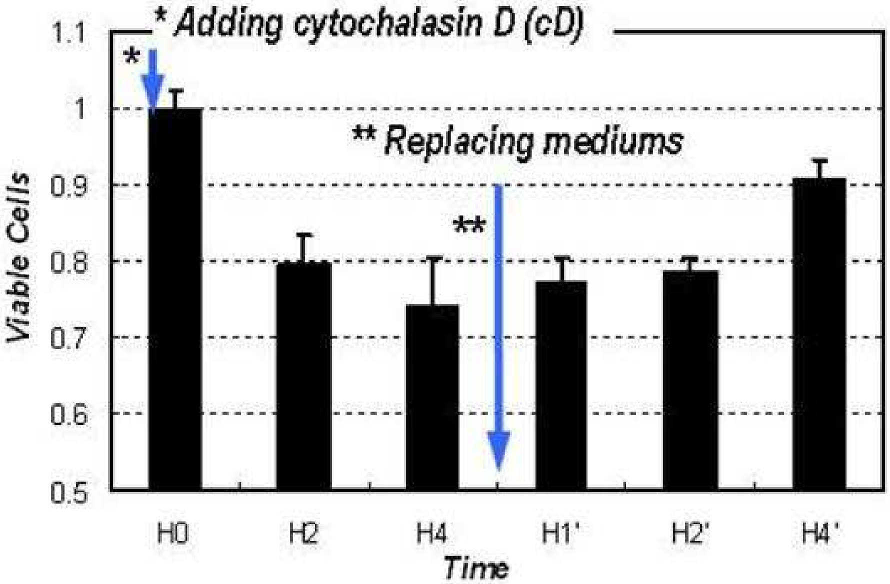

(b) As a function of hours at a fixed 3 μM cytochalasin D

Figure 5.7: Biochemical results of Endothelial cells (ECs): (a) as a function of days and dose and (b) as a function of hours at a fixed 3 μM cytochalasin D concentration.

large cell-to-substrate gaps that appear as bright spots. Interference reflection microscopy images are obtained by interference of reflected lights from the interface at the glass-medium and medium-bottom membrane. Reflected lights from the top membrane produce a signal that is too weak to capture, which should therefore not disturb calculations made for the bottom surface.

While the actin filament-stained confocal fluorescence images use fixed cells, which are dead cells, the MS-IRM images use live cells. Most importantly and interestingly, these IRM images clearly show bottom morphology changes caused by the toxic agent. In figure 5.8, there is a dramatic morphology change caused by cytochalasin D on endothelial cells caused by 3 μM cytochalasin D treatment using differential interference reflection microscopy (DICM) and multi-spectrum interference reflection microscopy (MS-IRM). Endothelial cells shrink under the toxic agent, similar to apoptotic morphology changes, but their substrate adherence substantially recovers after replacing the treated medium with new complete medium.

5.5 Conclusion

This dynamic response of the cells to different environments and sensitivity to toxicants is a valuable tool for many drug discovery methods and tissue engineering applications. Table 5.1 shows a summary of the pros and cons of four different methods used to examine the cytotoxicity effect of cytochalasin D on endothelial cells. The optical techniques of the actin filament stained confocal images and multi-spectrum interference reflection microscopy combined with spectrophotometry measurement and micro-impedance measurement promises to be efficient tools in studying the various behavioral characteristics of cells under toxic conditions.

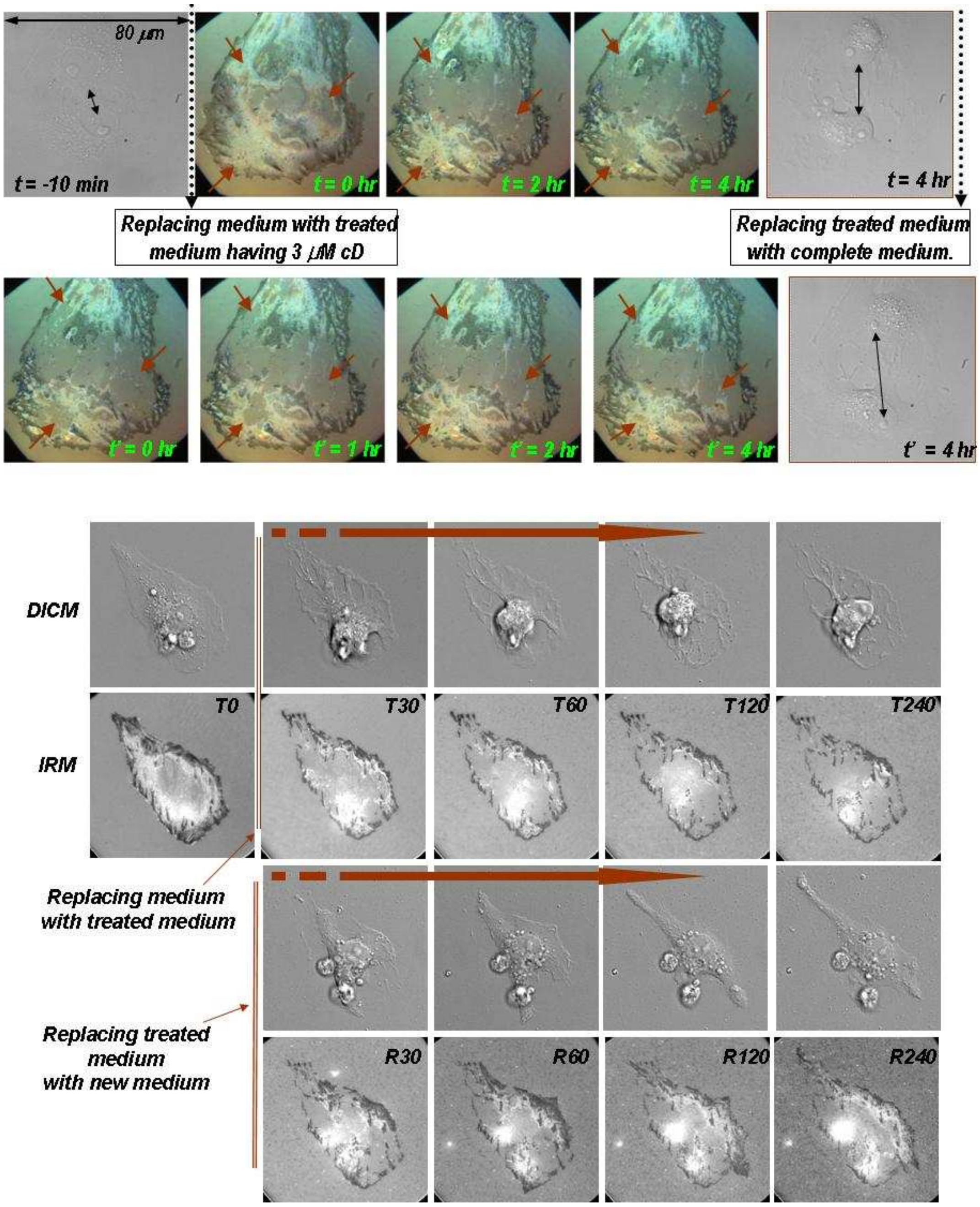

Figure 5.8: Observation of a dramatic morphology change of endothelial cells caused by 3 μM cytochalasin D treatment using differential interference reflection microscopy (DICM) and multi-spectrum interference reflection microscopy (MS-IRM).

Table 5.1 A summary of the pros and cons of all the methods used to examine the cytotoxicity effect of 3 μM cytochalasin D onto endothelial cells.

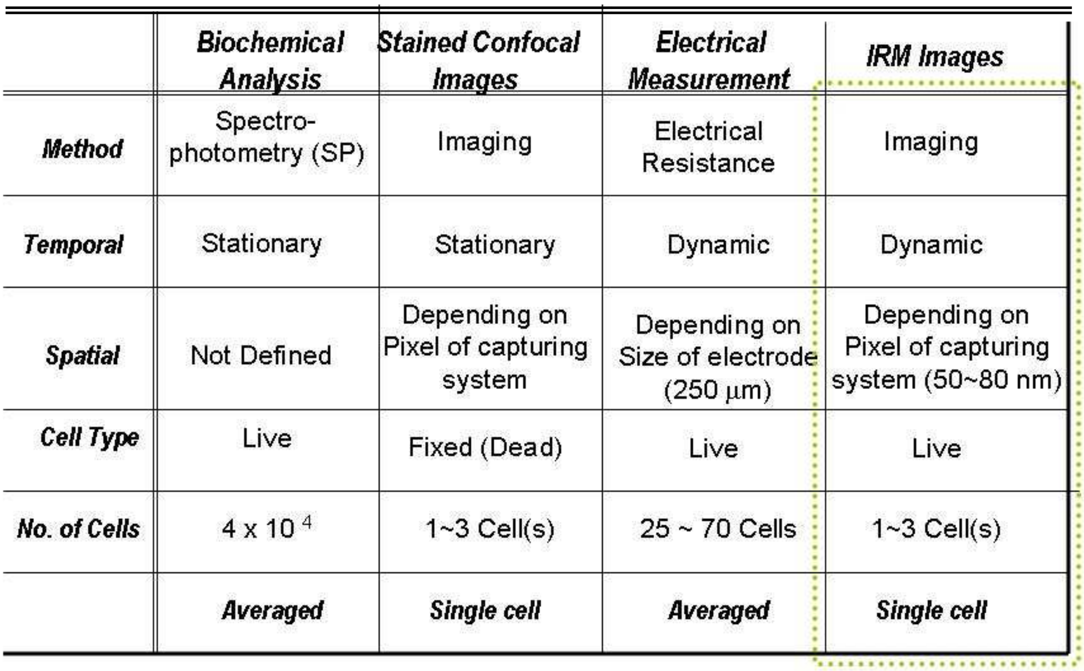

	Biochemical Analysis	***Stained Confocal Images***	***Electrical Measurement***	***IRM Images***
Method	Spectro-photometry (SP)	Imaging	Electrical Resistance	Imaging
Temporal	Stationary	Stationary	Dynamic	Dynamic
Spatial	Not Defined	Depending on Pixel of capturing system	Depending on Size of electrode (250 μm)	Depending on Pixel of capturing system (50~80 nm)
Cell Type	Live	Fixed (Dead)	Live	Live
No. of Cells	4×10^4	1~3 Cell(s)	25 ~ 70 Cells	1~3 Cell(s)
	Averaged	***Single cell***	***Averaged***	***Single cell***

Biochemical analysis using spectrophotometry is a valuable and reliable method, which is stationary and provides averaged values for many cells. Even though stained confocal images employ a stationary digital imaging method using fixed cells, it produces evident fluorescent actin filament disruption. The impedance measurements are a dynamic definitive indicator for cellular morphology changes caused by toxic agents. Nevertheless, the MS-IRM imaging technique with our developed advanced opto-electric system has the most attractive advantages such as a dynamic and label-free measurement, with a 10-nm order spatial resolution, and better time resolution (up to 57.7fps using the current EM-CCD), and single live cell detection.

These Cytotoxicity tests give a deep insight in to the mechanism of these cells and how the various structures of the cell contribute in its division, proliferation and migration. Thus, this combined analysis with the relevant optical techniques and signal processing algorithms can make a very good package for *in vitro* toxicology monitoring and other cell based assays.

CHAPTER 6

CONCLUSION

In order to build a dynamic live cell opto-electric biosensor an optical sensing system was needed consisting of several microscopic methods including regular bright-field microscopy (BFM), phase contrast microscopy (PCM), differential interference contrast microscopy (DICM), multi-spectrum interference reflection microscopy (MS-IRM), total internal reflection fluorescence microscopy (TIRFM), and epi-fluorescence microscopy (EFM). Next an electrical system was chosen to measure the electrical impedance. In order to conduct both optical and electrical measurements simultaneously, an optically transparent and electrically conductive electrode was needed. The material best suited for this was ITO-Si_3N_4. Finally the optical and electrical ITO electrodes were combined with a lock-in amplifier, a cellular environmental incubation chamber, and a microscopy system in order to establish the integrated dynamic live-cell opto-electric detection system.

With an advanced integrated dynamic live-cell detection system built, two major experiments were completed as follows: (1) cellular proliferation and (2) in vitro cytotoxicity. First, with respect to cellular proliferation, cellular attachment and spreading were successfully examined by simultaneously and dynamically measuring optical and electrical characteristics of endothelial cells. Second, *in vitro* cytotoxicity effects of cytochalasin D on endothelial cells was comprehensively examined by using biochemical analysis, micro-impedance measurement, staining confocal microscopic imaging, and MS-IRM imaging.

The developed integrated dynamic live-cell opto-electric detection system can now provide multi-microscopic methods, including TIRFM for protein tracking, PCM for cells grown on plastic culture dishes, EPM for stained cells, DICM for realistic 3D cell imaging, IRM for cell-substrate interaction, and electrical impedance measurement with live cells.

REFERENCES

[1] M. Minsky, "Memoir on Inventing the Confocal Scanning Microscope," *Scanning,* vol. 10, pp. 128-138, 1998.

[2] R. H. Webb, "Confocal optical microscopy," *Rep. Prog. Phys.* , vol. 59, pp. 427-471, 1996.

[3] S. Kimura and C. Munakata, "Depth resolution of the fluorescent confocal scanning optical microscope," *Applied Optics*, vol. 59, pp. 489-494, 1990.

[4] H. Qian and E. L. Elson, "Analysis of confocal laser-microscope optics for 3-D fluorescence correlation spectroscopy," *Applied Optics,* vol. 30, pp. 1185-1195, 1991.

[5] C. J. R. Sheppard and M. Gu, "Aberration compensation in confocal microscopy," *Applied Optics,* vol. 30, pp. 3563-3568, 1991.

[6] S. Hell, G. Reiner, C. Cremer, and E. H. K. Stelzer, "Aberrations in confocal fluorescence microscopy induced by mismatches in refractive index," *Journal of Microscopy,* vol. 169, pp. 391-405, 1993.

[7] D. R. Sandison and W. W. Webb, "Background rejection and signal-to-noise optimization in confocal and alternative fluorescence microscopes," *Applied optics,* vol. 33, pp. 603-615, 1994.

[8] J.-A. Conchello and J. W. Lichtman, "Theoretical analysis of a rotating-disk partially confocal scanning microscope," *Applied Optics,* vol. 33, pp. 585-596, 1994.

[9] H. J. Tiziani and H.-M. Uhde, "Three-dimensional analysis by a microlens-array confocal arrangement " *Applied optics,* vol. 33, pp. 567-572, 1994.

[10] A. Ichihara, T. Tanaami, K. Isozaki, Y. Sugiyama, Y. Kosugi, K. Mikuriya, M. Abe,

and I. Uemura, "High-speed confocal fluorescence microscopy using a Nipkow scanner with microlenses for 3-D imaging of single fluorescent molecule in real time," *Bioimages,* vol. 4, pp. 57-62, 1996.

[11] A. Egner, V. Andersen, and S. W. Hell, "Comparison of the axial resolution of practical Nipkow-disk confocal fluorescence microscopy with that of multifocal multiphoton microscopy: theory and experiment," *Journal of Microscopy,* vol. 206, pp. 24-32, 2002.

[12] M. Raffel, C. E. Willert, and J. Kompenhans, "Particle Image Velocimetry: A Practical Guide," *Springer, Berlin,* 1998.

[13] J. G. Santiago, S. T. Wereley, C. D. Meinhart, D. J. Beebe, and R. J. Adrian, "A particle image velocimetry system for microfluidics," *Experiments in Fluids,* vol. 25, pp. 316-319, 1998.

[14] Y. Sugii, S. Nishio, and K. Okamoto, "In Vivo PIV Measurement of Red Blood Cell Velocity Field in Microvessels Considering Mesentery Motion," *Physiol. Meas.*, vol. 23, pp. 403-416, 2002.

[15] E. Hecht, "Optics (4th ed.)," *Addison Wesley, Reading,* 2002.

[16] S. Wilhelm, B. Grobler, M. Gluch, and H. Heinz, "Confocal Laser Scanning Microscopy: Principles," *Zeiss,* pp. 7-16, 2002.

[17] M. G. Olsen and R. J. Adrian, "Out-of-focus effects on particle image visibility and correlation in microscopic particle image velocimetry," *Experiments in Fluids,* vol. Suppl., pp. S166-S174, 2000.

[18] C. D. Meinhart, S. T. Wereley, and H. B. Gray, "Volume illumination for two-dimensional particle image velocimetry," *Measurement Science and Technology,*

vol. 11, pp. 809-814, 2000.

[19] M. Born and E. Wolf, "Principles of Optics, 7th edition," *Cambridge: Cambridge University Press,* p. 491, 1999.

[20] A. Diaspro, "Confocal and Two-photon Microscopy: Foundations, Application, and Advances," *Wiley-Liss, Inc., New York,* pp. 101~125, 245~247, 2002.

[21] M. G. Olsen and R. J. Adrian, "motion and correlation in particle image velocimetry," *Opt. & Laser Technol.,* vol. 32, pp. 621-627, 2000.

[22] V. Hohreiter, S. T. Wereley, M. G. Olsen, and J. N. Chung, "Cross-correlation analysis for temperature measurement," *Meas. Sci. Technol.* , vol. 13, pp. 1072-1078, 2002.

[23] Y. Sato, S. Inaba, K. Hishida, and M. Maeda, "Spatially averaged time-resolved particle-tracking velocimetry in microspace considering Brownian motion of submicron fluorescent particles," *Experiments in Fluids* vol. 35, pp. 167-177, 2003.

[24] J. B. Perrin, "Atoms," *Ox Bow Press, New York,* pp. 109-133, 1990.

[25] P. Nakroshis, M. Amoroso, J. Legere, and C. Smith, "Measuring Boltzmann's constant using video microscopy of Brownian motion," *Am. J. Phys.* , vol. 71, pp. 568-573, 2002.

[26] R. Salmon, C. Robbins, and K. Forinash, "Brownian motion using video capture," *Eur. J. Phys.,* vol. 23, pp. 1-5, 2002.

[27] K. D. Kihm, A. Banerjee, C. K. Choi, and T. Takagi, "Near-wall hindered Brownian diffusion of nanoparticles examined by three-dimensional Ratiometric Total Internal Reflection Fluorescence Microscopy (3D R-TIRFM)," *Experiments*

in Fluids vol. 37, pp. 105-119, 2004.

[28] D. A. Agard, "Optical sectioning microscopy: cellular architecture in three dimensions," *Ann. Rev. Biophys. Bioeng.,* vol. 13, pp. 191-219, 1984.

[29] M. Cagnet, M. Francon, and J. C. Thrierr, "Atlas of optical phenomena " *Berlin: Springer –Verlag,* 1962.

[30] B. Richards and E. Wolf, "Electromagnetic diffraction in optical systems II. Structure of the image field in an aplanatic system," *Proc. R. Soc. A* vol. 253, pp. 358-379, 1959.

[31] F. S. Gibson and F. Lanni, "Experimental test of an analytical model of aberration in an oil-immersion objective lens used in three-dimensional light microscopy " *J. Opt. Soc. Am. A* vol. 8, pp. 1601-1613, 1991.

[32] S. Inoué and K. R. Spring, "Video Microscopy: The Fundamentals," *New York: Plenum,* pp. 26-65, 1997.

[33] J. G. McNally, C. Preza, J. A. Conchello, and L. J. Thomas, "Artifacts in computational optical-sectioning microscopy," *J. Opt. Soc. Am. A* vol. 11, pp. 1056-1067, 1994.

[34] M. Speidel, A. Jonas, and E. L. Florin, "Three-dimensional tracking of fluorescent nanoparticles with subnanometer precision by use of off-focus imaging " *Optics Letters* vol. 28, pp. 69-71, 2003.

[35] F. Pereira and M. Gharib, "Defocusing digital particle image velocimetry and the three-dimensional characterization of two-phase flows " *Meas. Sci. Technol.,* vol. 13, pp. 683-694, 2002.

[36] R. Brown, "The World of the Atoms, edited by H. Boorse and L. Motz," *New*

York: Basic Books, vol. 1, pp. 206-212, 1966.

[37] W. B. Russel, D. A. Saville, and W. R. Schowalter, "Colloidal dispersions " *Cambridge University Press,* pp. 21-63, 1989.

[38] S. Gray, "Several microscopical observations and experiments, made by Mr. Stehpen Gray," *Phil Trans,* vol. 19, pp. 280-287 1695.

[39] R. Brown, "A brief account of Microscopical Observations made in the months of June, July and August, 1827, on the particles contained in the pollen of plants; and on the General Existence of Active Molecules in Organic and Inorganic bodies," *Phil Mag,* vol. 4, pp. 161-173, 1828.

[40] J. Renn, "Einstein’s invention of Brownian motion," *Ann Phys* vol. 14, pp. supplement 23-37 2005.

[41] A. Einstein, "On the motion, required by the molecular-kinetic theory of heat, of particles suspended in a fluid at rest," *Ann Phys (Leipzig)* vol. 17, pp. 549-560 1905.

[42] K. Schatzel, W. G. Neumann, J. Muller, and B. Materzok, "Optical Tracking of Brownian Particles," *Applied Optics,* vol. 31, pp. 770-778 1992.

[43] A. J. Goldman, R. G. Cox, and H. Brenner, "Slow viscous motion of a sphere parallel to a plane-I: Motion through a quiescent fluid," *Chem Engg Sci* vol. 22, pp. 637-651 1967.

[44] H. Brenner, "The slow motion of a sphere through a viscous fluid towards a plane surface," ***Chem Engg Sci*** vol. 16, pp. 242-251, 1961.

[45] M. A. Bevan and D. C. Prieve, "Hindered diffusion of colloidal particles very near to a wall: Revisited," *J Chem Phys,* vol. 113, pp. 1228-1236 2000.

[46] E. S. Pagac, R. D. Tilton, and D. C. Prieve, "Hindered mobility of a rigid sphere near a wall," *Chem Eng Comm,* vol. 148, pp. 105-122, 1996.

[47] A. Banerjee and K. D. Kihm, "Experimental verification of near-wall hindered diffusion for the Brownian motion of nanoparticles using evanescent wave microscopy," *Phys Rev E* vol. 72, p. 042101, 2005.

[48] D. Axelrod, "Total internal reflection fluorescence microscopy in cell biology," *Traffic,* vol. 2, pp. 764-774, 2001.

[49] A. Rohrbach, "Observing Secretory Granules with a Multiangle Evanescent Wave Microscope," *Biophy J* vol. 78, pp. 2641-2654, 2000.

[50] T. P. Burghart and N. L. Thompson, "Effects of planar dielectric interfaces on fluorescence emission and detection," *Biophys J,* vol. 46, pp. 729-737 1984.

[51] E. H. Hellen and D. Axelrod, "Fluorescence emission at dielectric and metal film interfaces," *J Opt Soc Am B* vol. 4, pp. 337-350 1986.

[52] H. J. Wu and M. A. Bevan, "Direct Measurement of Single and Ensemble Average Particle-Surface Potential Energy Profiles,," *Langmuir,* vol. 21, pp. 1244-1254, 2005.

[53] G. A. Schumacher and v. d. V. TGM, "Evanescent Wave Scattering Studies on Latex-Glass Interactions," *Langmuir,* vol. 7, pp. 2028-2033 1991.

[54] R. Newburgh, J. Peidle, and W. Rueckner, "Einstein, Perrin, and the reality of atoms: 1905 revisited," *Am J Phys,* vol. 74, pp. 478-481 2006.

[55] A. D. Katsen, B. Vollmar, P. Mestres-Ventura, and M. D. Menger, "Cell surface and nuclear changes during TNF-alpha-induced apoptosis in WEHI 164 murine fibrosarcoma cells. A correlative light, scanning, and transmission electron

microscopical study," *Virchows Arch,* vol. 433, pp. 75-83, Jul 1998.

[56] T. M. Kolb, S. H. Chang, and M. A. Davis, "Biochemical and morphological events during okadaic acid-induced apoptosis of Tsc2-null ERC-18 cell line," *Toxicol Pathol,* vol. 30, pp. 235-46, Mar-Apr 2002.

[57] S. Ohta, J. Yoshida, S. Yamamoto, K. Uemura, T. Wakabayashi, M. Mizuno, T. Sakurai, and S. Terakawa, "Video-enhanced microscopic visualization of apoptotic cell death caused by anti-Fas antibody in living human glioma cells," *Brain Tumor Pathol,* vol. 15, pp. 19-21, 1998.

[58] I. Palyi, B. Vincze, S. Lovas, I. Mezo, J. Pato, A. Kalnay, G. Turi, D. Gaal, R. Mihalik, I. Peter, I. Teplan, and R. F. Murphy, "Gonadotropin-releasing hormone analogue conjugates with strong selective antitumor activity," *Proc Natl Acad Sci U S A,* vol. 96, pp. 2361-6, Mar 2 1999.

[59] J. C. Papadimitriou, C. B. Drachenberg, M. L. Shin, and B. F. Trump, "Ultrastructural studies of complement mediated cell death: a biological reaction model to plasma membrane injury," *Virchows Arch,* vol. 424, pp. 677-85, 1994.

[60] P. Prolo, F. Chiappelli, E. Cajulis, J. Bauer, S. Spackman, H. Romeo, M. Carrozzo, S. Gandolfo, and R. Christensen, "Psychoneuroimmunology in oral biology and medicine: the model of oral lichen planus," *Ann N Y Acad Sci,* vol. 966, pp. 429-40, Jun 2002.

[61] R. Rauh, S. Kahl, H. Boechzelt, R. Bauer, B. Kaina, and T. Efferth, "Molecular biology of cantharidin in cancer cells," *Chin Med,* vol. 2, p. 8, Jul 4 2007.

[62] Y. Ryuke, M. Mizuno, A. Natsume, O. Suzuki, M. Nobayashi, T. Kageshita, K. Matsumoto, T. Saida, and J. Yoshida, "Growth inhibition of subcutaneous mouse

melanoma and induction of natural killer cells by liposome-mediated interferon-beta gene therapy," *Melanoma Res,* vol. 13, pp. 349-56, Aug 2003.

[63] K. Sharma, R. X. Wang, L. Y. Zhang, D. L. Yin, X. Y. Luo, J. C. Solomon, R. F. Jiang, K. Markos, W. Davidson, D. W. Scott, and Y. F. Shi, "Death the Fas way: regulation and pathophysiology of CD95 and its ligand," *Pharmacol Ther,* vol. 88, pp. 333-47, Dec 2000.

[64] E. Straface, M. T. Santini, G. Donelli, P. U. Giacomoni, and W. Malorni, "Vitamin E prevents UVB-induced cell blebbing and cell death in A431 epidermoid cells," *Int J Radiat Biol,* vol. 68, pp. 579-87, Nov 1995.

[65] S. L. Wang, B. Cai, C. B. Cui, H. W. Liu, C. F. Wu, and X. S. Yao, "[Apoptosis of human chronic myeloid leukemia k562 cell induced by prosapogenin B of dioscin (P.B) in vitro]," *Ai Zheng,* vol. 22, pp. 795-800, Aug 2003.

[66] M. Wu, K. A. Harvey, N. Ruzmetov, Z. R. Welch, L. Sech, K. Jackson, W. Stillwell, G. P. Zaloga, and R. A. Siddiqui, "Omega-3 polyunsaturated fatty acids attenuate breast cancer growth through activation of a neutral sphingomyelinase-mediated pathway," *Int J Cancer,* vol. 117, pp. 340-8, Nov 10 2005.

[67] D. Yoshida, M. Noha, K. Watanabe, T. Bergenheim, R. Henriksson, and A. Teramoto, "The bleb formation of the extracellular pseudopodia; early evidence of microtubule depolymerization by estramustine phosphate in glioma cell; in vitro study," *J Neurooncol,* vol. 52, pp. 37-47, Mar 2001.

[68] B. Zhang, Z. Arany, D. Mann, J. G. Rhee, and R. G. Fenton, "Partitioning apoptosis: a novel form of the execution phase of apoptosis," *Apoptosis,* vol. 10, pp. 219-31, Jan 2005.

[69] C. Zhou, S. Chi, J. Deng, J. Liang, and R. Biolo, "[Apoptosis of mouse MS-2 fibrosarcoma cells induced by photodynamic therapy with LDL-administered zinc-phthalocyanine]," *Zhongguo Yi Xue Ke Xue Yuan Xue Bao,* vol. 17, pp. 25-9, Feb 1995.

[70] D. Axelrod, "Total internal reflection fluorescence microscopy in cell biology," *Traffic,* vol. 2, pp. 764-74, Nov 2001.

[71] L. Bliokh Zh, A. E. Platonov, and V. V. Smolianinov, "[Investigation of initial stage of fibroblast attachment by means of interference reflection microscopy]," *Biofizika,* vol. 27, pp. 120-5, Jan-Feb 1982.

[72] R. J. Bloch and B. Geiger, "The localization of acetylcholine receptor clusters in areas of cell-substrate contact in cultures of rat myotubes," *Cell,* vol. 21, pp. 25-35, Aug 1980.

[73] J. S. Burmeister, L. A. Olivier, W. M. Reichert, and G. A. Truskey, "Application of total internal reflection fluorescence microscopy to study cell adhesion to biomaterials," *Biomaterials,* vol. 19, pp. 307-25, Mar 1998.

[74] L. V. Domnina, V. I. Gelfand, O. Y. Ivanova, E. V. Leonova, O. Y. Pletjushkina, J. M. Vasiliev, and I. M. Gelfand, "Effects of small doses of cytochalasins on fibroblasts: preferential changes of active edges and focal contacts," *Proc Natl Acad Sci U S A,* vol. 79, pp. 7754-7, Dec 1982.

[75] B. Geiger, Z. Avnur, and J. Schlessinger, "Restricted mobility of membrane constituents in cell-substrate focal contacts of chicken fibroblasts," *J Cell Biol,* vol. 93, pp. 495-500, May 1982.

[76] J. M. Heiple, S. D. Wright, N. S. Allen, and S. C. Silverstein, "Macrophages form

circular zones of very close apposition to IgG-coated surfaces," *Cell Motil Cytoskeleton,* vol. 15, pp. 260-70, 1990.

[77] G. W. Ireland and C. D. Stern, "Cell-substrate contacts in cultured chick embryonic cells: an interference reflection study," *J Cell Sci,* vol. 58, pp. 165-83, Dec 1982.

[78] F. Lanni, A. S. Waggoner, and D. L. Taylor, "Structural organization of interphase 3T3 fibroblasts studied by total internal reflection fluorescence microscopy," *J Cell Biol,* vol. 100, pp. 1091-102, Apr 1985.

[79] M. M. Lee, F. H. Green, W. M. Schoel, and S. Schurch, "Cell-substrate adhesion and metastatic potential of cultured mesothelioma cells induced by asbestos," *Biochim Biophys Acta,* vol. 1226, pp. 151-62, May 25 1994.

[80] K. K. Liu, V. Chan, and Z. Zhang, "Capsule-substrate contact deformation: determination of adhesion energy," *Med Biol Eng Comput,* vol. 40, pp. 491-5, Jul 2002.

[81] E. M. Narcisi, J. J. Paulin, and M. Fechheimer, "Presence and localization of vinculin in Giardia," *J Parasitol,* vol. 80, pp. 468-73, Jun 1994.

[82] R. G. Richards, M. Stiffanic, G. R. Owen, M. Riehle, I. Ap Gwynn, and A. S. Curtis, "Immunogold labelling of fibroblast focal adhesion sites visualised in fixed material using scanning electron microscopy, and living, using internal reflection microscopy," *Cell Biol Int,* vol. 25, pp. 1237-49, 2001.

[83] G. Rinnerthaler, B. Geiger, and J. V. Small, "Contact formation during fibroblast locomotion: involvement of membrane ruffles and microtubules," *J Cell Biol,* vol. 106, pp. 747-60, Mar 1988.

[84] P. Sanchez-Aparicio, A. M. Martinez de Velasco, C. M. Niessen, L. Borradori, I. Kuikman, E. H. Hulsman, R. Fassler, K. Owaribe, and A. Sonnenberg, "The subcellular distribution of the high molecular mass protein, HD1, is determined by the cytoplasmic domain of the integrin beta 4 subunit," *J Cell Sci,* vol. 110 (Pt 2), pp. 169-78, Jan 1997.

[85] M. Schindl, E. Wallraff, B. Deubzer, W. Witke, G. Gerisch, and E. Sackmann, "Cell-substrate interactions and locomotion of Dictyostelium wild-type and mutants defective in three cytoskeletal proteins: a study using quantitative reflection interference contrast microscopy," *Biophys J,* vol. 68, pp. 1177-90, Mar 1995.

[86] J. A. Sullivan and G. L. Mandell, "Motility of human polymorphonuclear neutrophils: microscopic analysis of substrate adhesion and distribution of F-actin," *Cell Motil,* vol. 3, pp. 31-46, 1983.

[87] H. Tatsumi, Y. Katayama, and M. Sokabe, "Attachment of growth cones on substrate observed by multi-mode light microscopy," *Neurosci Res,* vol. 35, pp. 197-206, Dec 1 1999.

[88] M. Terai, M. Komiyama, and Y. Shimada, "Myofibril assembly is linked with vinculin, alpha-actinin, and cell-substrate contacts in embryonic cardiac myocytes in vitro," *Cell Motil Cytoskeleton,* vol. 12, pp. 185-94, 1989.

[89] C. Urquhart, "Morphological and adhesive changes to cultured chick kidney cells following parasitization with Eimeria tenella (Protozoa: Coccidia)," *Parasitology,* vol. 82, pp. 175-87, Apr 1981.

[90] H. Verschueren, "Interference reflection microscopy in cell biology: methodology

and applications," *J Cell Sci,* vol. 75, pp. 279-301, Apr 1985.

[91] D. A. Borkholder, "Cell Based Biosensors using microelectrodes, in Electrical Engineering," *Stanford University,* 1998.

[92] I. Giaever and C. R. Keese, "Monitoring fibroblast behavior in tissue culture with and applied electric field," *Proc. Natl. Acad. Sci. USA,* vol. 81, pp. 3761-3764, 1984.

[93] I. Giaever and C. R. Keese, "Use of Electric Fields to Monitor the Dynamical Aspect of Cell Behavior in Tissue Culture," *IEEE Trans. Biomed. Eng.,* vol. BME-33, pp. 242-247, 1986.

[94] I. Giaever and C. R. Keese, "Micromotion of Mammalian Cells Measured Electrically," *Proc. Natl. Acad. Sci. USA,* vol. 88, pp. 7896-7900, 1991.

[95] C. M. Lo, C. R. Keese, and I. Giaever, "Impedance Analysis of MDCK Cells Measured by Electric Cell-Substrate Impedance Sensing," *Biophys. J.,* vol. 69, pp. 2800-2807, 1995.

[96] C. Xiao, B. Lachance, G. Sunahara, and J. H. T. Luong, "Assessment of cytotoxicity using electric cell-substrate impedance sensing: concentration and time response function approach," *Anal. Chem.,* vol. 74, pp. 5748-5753, 2002.

[97] C. Xiao, B. Lachance, G. Sunahara, and J. H. T. Luong, "An in-depth analysis of electric cell-substrate impedance sensing to study the attachment and spreading of mammalian cells," *Anal. Chem.,* vol. 74, pp. 1333-1339, 2002.

[98] C. A. J. Thomas, G. E. Loeb, N. Y. Berwald, and C. M. Okun, "A miniature microelectrode array to monitor the bioelectric activity of cultured cells," *Experimental Cell Research,,* vol. 74, pp. 61-66, 1972.

[99] P. O'Shea, B. Goodwin, and I. Ridge, "A vibrating electrode anslysis of extracellular ion currents in Acetabularia acetabulum," *Journal of Cell Science,* vol. 97, pp. 503-508, 1990.

[100] Y. Jimbo and A. Kawana, "Electrical stimulation of cultured neural cells by planar electrode array," *Annual International Conference of the IEEE Engineering in Medicine and Biology Society,* pp. Tokyo, Japan, 1990.

[101] A. R. Burns, R. A. Bowden, S. D. MacDonell, D. C. Walker, T. O. Odebunmi, E. M. Donnachie, S. I. Simon, M. L. Entman, and C. W. Smith, "Analysis of Tight Junctions During Neutrophil Transendothelial Migration," *Journal of Cell Science,* vol. 113, pp. 45-57, 2000.

[102] C. A. Ellis, C. Tiruppathi, R. sandoval, W. D. Niles, and A. B. Malik, "Time Course of Recovery of Endothelial Cell Surface Thrombin Receptor (PAR-1) Expression," *Am. J. Physiol. (Cell Physiol.),* vol. 276, pp. C38-C45, 1999.

[103] J. P. Gainor, C. A. Morton, J. T. Roberts, P. A. Vincent, and F. L. Minnear, "Platelet-Conditioned Medium Increases Endothelial Electrical Resistance Independently of cAMP/PKA and cGMP/PKG," *Am. J. Physiol. Heart Circ. Physiol.,* vol. 281, pp. H1992-H2001, 2001.

[104] N. Kataoka, K. Iwaki, K. Hashimoto, S. Mochizuki, Y. Ogasawara, M. Sato, K. Tsujioka, and F. Kajiya, "Measurements of Endothelial Cell-to-Cell and Cell-to-Substrate Gaps and Micromechanical Properties of Endothelial Cells During Monocyte Adhesion," *Proc. Natl. Acad. Sci.,* vol. 99, pp. 15638-15643, November 26, 2002 2002.

[105] J. E. Phelps and N. DePaola, "Spatial Variations in Endothelial Barrier Function in

Disturbed Flows In Vitro," *Am. J. Physiol. Heart Circ. Physiol.*, vol. 278, pp. H469-H476, 2000.

[106] R. Sandoval, A. B. Malik, R. D. Minshall, P. Kouklis, C. A. Ellis, and A. Tiruppathi, "Ca2+ Signalling and PKCa Activate Increased Endothelial Permeability by Disassembly of VE-Cadherin Junctions," *J. Physiology*, vol. 533, pp. 433-445, 2001.

[107] C. Tiruppathi, A. B. Malik, P. J. D. Vecchio, C. R. Keese, and I. Giaever, "Electrical Method For Detection of Endothelial Cell Shape Change in Real Time: Assessment of Endothelial Barrier Function," *Proc. Natl. Acad. Sci. USA*, vol. 89, pp. 7919-7923, 1992.

[108] W. Tschugguel, Z. Zhegu, L. Gajkzik, M. Maier, B. R. Binder, and J. Graf, "High Precision Measurement of Electrical Resistance Across Endothelial Cell Monolayers," *Pflugers Arch - Eur J Physiol*, vol. 430, pp. 145-147, 1995.

[109] J. Wegener, C. R. Keese, and I. Giaever, "Electric Cell-Substrate Impedance Sensing (ECIS) as a Noninvasive Means to Monitor the Kinetics of Cell Spreading to Artificial Surfaces," *Experimental Cell Research*, vol. 259, pp. 158-166, 2000.

[110] J. Wegener, S. Zink, P. Rosen, and H.-J. Galla, "Use of Electrochemical Impedance Measurements to Monitor Beta-Adrenergic Stimulation of Bovine Aortic Endothelial Cells," *Pflugers. Arch. - Eur. J. Physiol.*, vol. 437, pp. 925-934, 1999.

[111] A. R. Burns, D. C. Walker, E. S. Brown, L. T. Thurmon, R. A. Bowden, C. R. Keese, S. I. Simon, M. L. Entman, and C. W. Smith, "Neutrophil Transendothelial

Migration is Independent of Tight Junctions and Occurs Preferentially at Tricellular Corners," *J. Immunol.*, vol. 159, pp. 2893-2903, 1997.

[112] V. Bucher, B. Brunner, C. Leibrock, M. Schubert, and W. Nisch, "Electrical properties of a light-addressable microelectrode chip with high electrode density for extracellular stimulation and recroding of excitable cells," *Biosensors and Bioelectronics*, vol. 16, pp. 205-210, 2001.

[113] V. Bucher, M. Schubert, D. Kern, and W. Nisch, "Light-addressed sub-micron electrodes for extracellular recording and stimulation of excitable cells," *Microelectronic engineering*, vol. 57-58, pp. 705-712, 2001.

[114] F. Fabregat-Santiago, N. S. Ferriols, and G. Garcia-Belmonte, "Determiniation of the humidity of soil by monitoring the conductivity with indium tin oxide glass electrodes," *80*, vol. 15, pp. 2785-2787, 2002.

[115] S. Gritsch, P. Nollert, F. Jahnig, and E. Sackmann, "Impedance Spectroscopy of Porin and Gramicidin Pores Reconstituted into Supported Lipid Bilayers on Indium-Tin Oxide Electrodes," *Langmuir*, vol. 14, pp. 3118-3125, 1998.

[116] G. W. Gross, W. Y. Wen, and J. W. Lin, "Transparent indium-tin oxide electrode patterns for extracellular, multisite recording in neuronal cultures," *Journal of Neuroscience Methods*, vol. 15, pp. 243-252, 1985.

[117] H. Hillebrandt, G. Wiegand, M. Tanaka, and E. Sackmann, "High Electric resistance Polymer/Lipid Composite Films on Indium-Tin-Oxide Electrodes," *Lanmguir*, vol. 15, pp. 8451-8459, 1999.

[118] S.-I. Jun, T. E. McKnight, M. L. Simpson, and P. D. Rack, "A statistical parameter study of indium tin oxide thin films deposited by radio-frequency sputtering,"

Thin Solid Films, vol. 476, pp. 59-64, 2005.

[119] M. Penza, S. Cozzi, M. A. Tagliente, L. Mirenghi, C. Martucci, and A. Quirini, "Characterization of transparent and conductive electrodes of indium tin oxide thin films by sequential reactive evaporation," *Thin Solid Films* vol. 349, pp. 71-77, 1999.

[120] S. Ray, R. Banerjee, N. Basu, A. K. Batabyal, and A. K. Barua, "Properties of tin doped indium oxide thin films prepared by magnetron sputtering," *J. Appl. Phys.*, vol. 54, p. 3497, June 1983.

[121] B. Albert, D. Bray, J. Lewis, M. Raff, K. Robert, and J. D. Watson, "Molecular Biology of THE CELL 3rd ed," *Garland Publishing, Inc.,* 1993.

[122] H. Stebbings, J. D. Lane, and N. J. Talbot, "mRNA translocation and microtubules in sect ovary models," *Trends in cell Biol.,* vol. 5, pp. 361-365, 1995.

[123] P. M. Novikoff, M. Cammer, L. Tao, H. Oda, R. J. Stockert, A. W. Wolkoff, and P. Satir, "Three-dimensional organization of rat hepatocyte cytoskeleton: relation to the asialoglycoprotein endocytosis pathway," *J. Cell Science* vol. 109, pp. 21-32 1996.

[124] J. F. Challacombe, D. M. Snow, and P. C. Letourneau, "Actin filament bundles are required for microtubule reorientation during growth cone turning to avoid an inhibitory guidance cue," *J. Cell Science* vol. 109, pp. 2031-2040 1996.

[125] C. S. Spittle and L. Cassimeris, "Mechanism blocking microtubule minus end assembly: Evidence for a tubulin dimer-binding protein," *Cell Motil. Cytoskeleton* vol. 34, pp. 324-335 1996.

[126] S. X. H. Lin, K. K. Pfister, and C. A. Collins, "Comparison of the intracellular

distribution of cytoplasmic dynein and kinesin in cultured cells: Motor protein location does not reliably predict fuction," *Cell Motil. Cytoskeleton* vol. 34, pp. 299-312 1996.

[127] O. Valiron, V. Chevrier, Y. Usson, F. Breviario, and D. Job, "Desmoplakin expression and organiztion at human umbilical vein endothelial cell-to-cell junctions," *J. Cell Science,* vol. 109, pp. 2141-2149 1996.

[128] D. J. Fishkind, J. D. Silverman, and Y. L. Wang, "Function of spindle microtubules in directing cortical movement and actin filament organization in dividing cultured cells,," *J. Cell Science,* vol. 109, pp. 2041-2051 1996.

[129] A. Durrbach, D. Louvard, and E. Coudrier, "Actin filaments facilitate two steps of endocytosis," *J. Cell Science,* vol. 109, pp. 457-465 109.

[130] N. Wang, J. P. Butler, and D. E. Ingber, "Mechanotransduction across the cell surface and through the cytoskelton," *Science,* vol. 260, pp. 1124-1127 1993.

[131] G. Plopper and D. E. Ingber, "Rapid induction and isolation of focal adhesion complexes, Biochem," *Biophy. Res. Comm.* , vol. 193, pp. 571-578 1993.

[132] N. Wang and D. E. Ingber, "Control of cytoskeletal mechanics by extracellular matrix, cell shape, and mechanical tension," *Biophysical J.* , vol. 66, pp. 2181-2189 1994.

[133] D. J. Mooney, R. Langer, and D. E. Ingber, "Cytoskeletal filament assembly and the control of cell spreading and function by extracellular matrix," *J. Cell Science* vol. 108, pp. 2311-2320 1995.

[134] A. R. Burns, D. C. Walker, E. S. Brown, L. T. Thurmon, R. A. Bowden, C. R. Keese, S. I. Simon, M. L. Entman, and C. W. Smith, "Neutrophil transendothelial

migration is independent of tight junctions and occurs preferentially at tricellular corners," *The Journal of Immunology,* vol. 159, pp. 2893-2903, 1997.

[135] A. E. English, C. P. Plaut, and M. A. B., "A Riemannian manifold analysis of endothelial cell monolayer impedance parameter precision,

," *J. Math. Bio.,* vol. In press, 2007.

[136] A. E. English, J. C. Squire, J. E. Bodmer, and M. A. B., "ndothelial cell electrical impedance parameter artifacts produced by a gold electrode and phase sensitive detection," *IEEE Trans. Biomed. Eng.* , vol. 54, pp. 863-873, 2007.

[137] H. Hillebrandt, A. Abdelghani, C. Abdelghani-Jaquin, M. Aepfelbacher, and E. Sackmann, "Electrical and optical characterization of thrombin-induced permeability of cultured endothelial cell monolayers on semiconductor electrode arrays," *Appl. Phys. A,* vol. 73, pp. 539-546, 2001.

[138] C. K. Choi, A. E. English, S.-I. Jun, K. D. Kihm, and R. P. D., "An endothelial cell compatible biosensor fabricated using optically thin indium tin oxide silicon nitride electrodes," *Biosensors and Bioelectronics,* vol. 22, pp. 2585-2590, 2007.

[139] C. K. Dorey, F. C. Delori, and K. Akeo, "Growth of cultured retinal pigment epithelial (RPE) and endothelial cell is inhibited by blue light but not green or red light," *Current Eye Research,* vol. 9, pp. 549-559, Jun 1990.

[140] S. Venkataraman, J. L. Morrell-Falvey, M. J. Doktycz, and H. Qi, "Automated image analysis of fluorescence microscopic images to identify protein-protein interactions," in *Proceedings of the 2005 IEEE Engineering in Medicine and Biology 27th Annual Conference,* Shanghai, China, 2005, pp. 797-800.

[141] D. G. Babbitt, M. B. Forman, R. Jones, A. K. Bajaj, and R. L. Hoover, "Prevention

of neutrophil-mediated injury to endothelial cells by perfluorochemical," *Am J Pathol*, vol. 136, pp. 451-9, Feb 1990.

[142] A. F. Lopez, D. J. Williamson, J. R. Gamble, C. G. Begley, J. M. Harlan, S. J. Klebanoff, A. Waltersdorph, G. Wong, S. C. Clark, and M. A. Vadas, "Recombinant human granulocyte-macrophage colony-stimulating factor stimulates in vitro mature human neutrophil and eosinophil function, surface receptor expression, and survival," *J Clin Invest*, vol. 78, pp. 1220-8, Nov 1986.

[143] T. Sacks, C. F. Moldow, P. R. Craddock, T. K. Bowers, and H. S. Jacob, "Oxygen radicals mediate endothelial cell damage by complement-stimulated granulocytes. An in vitro model of immune vascular damage," *J Clin Invest*, vol. 61, pp. 1161-7, May 1978.

[144] M. W. Stinson, S. Alder, and S. Kumar, "Invasion and killing of human endothelial cells by viridans group streptococci," *Infect Immun*, vol. 71, pp. 2365-72, May 2003.

[145] Z. Tabi, M. Moutaftsi, and L. K. Borysiewicz, "Human cytomegalovirus pp65- and immediate early 1 antigen-specific HLA class I-restricted cytotoxic T cell responses induced by cross-presentation of viral antigens," *J Immunol*, vol. 166, pp. 5695-703, May 1 2001.

[146] I. Giaever and C. R. Keese, "Fractal Motion of Mammalian Cells," *Physica D*, vol. 38, pp. 128-133, 1989.

[147] N. Ancellin, C. Colmont, J. Su, Q. Li, N. Mittereder, S. S. Chae, S. Stefansson, G. Liau, and T. Hla, "Extracellular export of sphingosine kinase-1 enzyme. Sphingosine 1-phosphate generation and the induction of angiogenic vascular

maturation," *J Biol Chem,* vol. 277, pp. 6667-75, Feb 22 2002.

[148] C. R. Carratelli, R. Paolillo, and A. Rizzo, "Chlamydia pneumoniae stimulates the proliferation of HUVEC through the induction of VEGF by THP-1," *Int Immunopharmacol,* vol. 7, pp. 287-94, Mar 2007.

[149] G. E. Davis and C. W. Camarillo, "Regulation of endothelial cell morphogenesis by integrins, mechanical forces, and matrix guidance pathways," *Exp Cell Res,* vol. 216, pp. 113-23, Jan 1995.

[150] G. Fibbi, R. Caldini, M. Chevanne, M. Pucci, N. Schiavone, L. Morbidelli, A. Parenti, H. J. Granger, M. Del Rosso, and M. Ziche, "Urokinase-dependent angiogenesis in vitro and diacylglycerol production are blocked by antisense oligonucleotides against the urokinase receptor," *Lab Invest,* vol. 78, pp. 1109-19, Sep 1998.

[151] D. A. Flusberg, Y. Numaguchi, and D. E. Ingber, "Cooperative control of Akt phosphorylation, bcl-2 expression, and apoptosis by cytoskeletal microfilaments and microtubules in capillary endothelial cells," *Mol Biol Cell,* vol. 12, pp. 3087-94, Oct 2001.

[152] S. M. Frisch, E. J. Clark, and Z. Werb, "Coordinate regulation of stromelysin and collagenase genes determined with cDNA probes," *Proc Natl Acad Sci U S A,* vol. 84, pp. 2600-4, May 1987.

[153] M. Gaudry, O. Bregerie, V. Andrieu, J. El Benna, M. A. Pocidalo, and J. Hakim, "Intracellular pool of vascular endothelial growth factor in human neutrophils," *Blood,* vol. 90, pp. 4153-61, Nov 15 1997.

[154] D. S. Grant, P. I. Lelkes, K. Fukuda, and H. K. Kleinman, "Intracellular

mechanisms involved in basement membrane induced blood vessel differentiation in vitro," *In Vitro Cell Dev Biol,* vol. 27A, pp. 327-36, Apr 1991.

[155] S. Huang, C. S. Chen, and D. E. Ingber, "Control of cyclin D1, p27(Kip1), and cell cycle progression in human capillary endothelial cells by cell shape and cytoskeletal tension," *Mol Biol Cell,* vol. 9, pp. 3179-93, Nov 1998.

[156] D. E. Ingber, D. Prusty, Z. Sun, H. Betensky, and N. Wang, "Cell shape, cytoskeletal mechanics, and cell cycle control in angiogenesis," *J Biomech,* vol. 28, pp. 1471-84, Dec 1995.

[157] E. Ispanovic and T. L. Haas, "JNK and PI3K differentially regulate MMP-2 and MT1-MMP mRNA and protein in response to actin cytoskeleton reorganization in endothelial cells," *Am J Physiol Cell Physiol,* vol. 291, pp. C579-88, Oct 2006.

[158] S. I. Resto-Ruiz, M. Schmiederer, D. Sweger, C. Newton, T. W. Klein, H. Friedman, and B. E. Anderson, "Induction of a potential paracrine angiogenic loop between human THP-1 macrophages and human microvascular endothelial cells during Bartonella henselae infection," *Infect Immun,* vol. 70, pp. 4564-70, Aug 2002.

[159] E. Y. Shin, J. Y. Lee, M. K. Park, Y. H. Chin, G. B. Jeong, S. Y. Kim, S. R. Kim, and E. G. Kim, "Overexpressed alpha3beta1 and constitutively activated extracellular signal-regulated kinase modulate the angiogenic properties of ECV304 cells," *Mol Cells,* vol. 9, pp. 138-45, Apr 30 1999.

[160] T. Udagawa, J. Yuan, D. Panigrahy, Y. H. Chang, J. Shah, and R. J. D'Amato, "Cytochalasin E, an epoxide containing Aspergillus-derived fungal metabolite, inhibits angiogenesis and tumor growth," *J Pharmacol Exp Ther,* vol. 294, pp.

421-7, Aug 2000.

[161] R. B. Vernon, S. L. Lara, C. J. Drake, M. L. Iruela-Arispe, J. C. Angello, C. D. Little, T. N. Wight, and E. H. Sage, "Organized type I collagen influences endothelial patterns during "spontaneous angiogenesis in vitro": planar cultures as models of vascular development," *In Vitro Cell Dev Biol Anim,* vol. 31, pp. 120-31, Feb 1995.

[162] L. Yan, M. A. Moses, S. Huang, and D. E. Ingber, "Adhesion-dependent control of matrix metalloproteinase-2 activation in human capillary endothelial cells," *J Cell Sci,* vol. 113 (Pt 22), pp. 3979-87, Nov 2000.

VITA

Chang Kyoung Choi was born in Sacheon-si, Kyoungnam Province in Korea on January 18, 1971 in the lunar calendar. After graduating from Dongmyoung High School in 1990, he entered Chung-Ang University in Seoul, Korea. He earned second place in the entrance examination to the Department of Mechanical Engineering and graduated in 1999 with the highest Honorary Certificate, equivalent to Magna Cum Laude, which was awarded to him by the president of Chung-Ang University. This certificate was given each year to the student with the highest GPA in the College of Engineering (1/445, GPA: 3.89/4.0).

After receiving his Bachelor's degree in Mechanical Engineering, he continued working for his Master's degree at Chung-Ang University. He was awarded a full scholarship for his entire period of his graduate work, and graduated in February 2001 (GPA: 4.0/4.0).

His doctorate in Mechanical Engineering began at Texas A&M University in August 2002, where he stayed until July 2004 (GPA: 3.87/4.0). At this point his advisor moved to the University of Tennessee and Chang Kyoung decided to follow him in order to make "a new history" at the University of Tennessee. He has successfully completed all requirements toward his doctoral degree at the Micro/Nano-Scale Fluidics and Energy Transport Laboratory. He has published 15 papers in highly regarded refereed journals in the area of mechanical, physical and biomedical areas. He has also published 4 conference proceeding publications, and a review article on the area of his research and the laboratory in KSME Magazine.

He received his doctoral degree in Mechanical and Biomedical Engineering on

August 2007 at the University of Tennessee under the supervision of his primary advisor, Dr. Kenneth D. Kihm, Magnavox Chair Professor, and his co-advisor, Dr. Anthony E. English, Assistant Professor, both of the Mech ABE Department.